Detector simulation, exclusive search and mass measurements for Supersymmetry at ATLAS

by

Marianne Johansen

Thesis
submitted for the degree of
Candidata Scientiarum

Division of Experimental Particle Physics
Department of Physics
University of Oslo

May 2005

Abstract

If supersymmetry is a symmetry of nature and is realized at the TeV-scale, a substantial production will take place at the Large Hadron Collider. Measurements of sparticle masses will be an important task. In an R-parity conserving scenario such measurements are complicated, due to the fact that the lightest supersymmetric particle escapes detection. Kinematical constraints on the detectable particles in the cascade decay chain $\tilde{q}_L \rightarrow \tilde{\chi}_2^0 q \rightarrow \tilde{l}_R^{\pm} l^{\mp} q \rightarrow \tilde{\chi}_1^0 l^+ l^- q$, make it possible to extract information on the sparticle masses. This is done by measuring endpoints of various invariant mass distribution related to the particles produced in the cascade. Proper detection and identification of the decay chain are therefore necessary. This thesis attempts to cover the various aspects needed for mass measurements. Detector performance related to leptons and jets is investigated, as well as the requirements used for extracting the decay chain from competing processes. Finally, mass measurements of fast and full simulation data are performed. Low statistics data samples corresponding to six months of running at the LHC are used for this purpose.

Acknowledgments

First I would like to thank my supervisors Prof. Lars Bugge and Ass. prof. Farid Ould-Saada for their experienced guidance, comments and support of my work. They have always kept their doors open, and given priority to my inquiries.

A special thank to Dr. Børge. K. Gjelsten for unveiling the secrets of SUSY mass measurements, and for generously sharing his time and knowledge. His contribution has been highly appreciated. Also thanks to Dr. Samir Ferrag for introducing me to full simulation data, and for bringing motivation when there was non left.

I am grateful to the group of Experimental Particle Physics at the University of Oslo for giving me the opportunity to attend international conferences and visit CERN. Prof. Alex Read has been particularly helpful; giving me computer assistance and a quiet office of my own. All group members; professors, staff, doctoral and master students, Olav Mundal and Mustafa Hussain, have, however, in one way or the other contributed to my thesis, thank you!

A very special thank to Robindra Prabhu who has been my friend and closest ally the last two years. His playfulness and cheerful spirit have made survival possible.

Finally, I would like to thank my friends, especially; Helene, Thomas, Daniel, Tone-Lill, Maria, Chris, Mathea and Helene, who have constantly reminded me of the world outside the physics department. I would prefer supersymmetry to not be found, rather than losing one of them.

Introduction

The aspiring goal of particle physics is to understand matter on a fundamental level. The search for the fundamental constituents of the universe has been an ongoing quest throughout history. The idea that matter is composed of elementary particles dates to at least the 6th century BC. At this point mainly two Greek philosophers, Leucippus and Democritus[1], developed Atomism. Atomism suggested that matter was composed of indivisible and imperishable elements called atoms, and that their properties in turn determined those of matter [41].

Present day particle physics are based on the same ideas put forward in ancient Greece. Quarks and leptons are the modern atoms, believed to be indivisible and imperishable in the sense that their numbers remain constant in the universe. Evidence is also found for macroscopic objects to obtain their properties through the characteristics of their fundamental constituents, as suggested by Democritus.

There is however a huge difference between the brave and creative ideas of Atomism and modern physics, that is testability. On the sunny shores of Miletus, Leucippus and Democritus could develop the idea of Atomism but were never able confirm it by experiment. Technological development and theoretical knowledge of the 20th century have for the first time in history made experiments in particle physics possible.

The first elementary particle to be discovered was the electron. It was first seen and identified as a negatively charged particle by J.J. Thompson in 1897 while he was studying cathode rays. A few years later Planck suggested that radiation comes in discrete amounts. His ideas were used by Einstein in 1905, who applied them on light, and proposed a quantum of light called the photon. Five years later the nucleus was discovered in alpha-scattering experiments performed by H. Geiger and E. Marsden under the supervision of E. Rutherford, while evidence of the proton was not found until ten years later. At this point only three fundamental particles were known, the electron, proton, and photon.

The 1930s lead to additional particles, many of them found in cosmic ray studies. Among the discoveries in this period were the neutron, muon and positron. The 1940s and 50s saw the first accelerator experiments and at the same time a cascade of particles were discovered. Sheldon Glashow suggested that particles interact through exchange of bosons[2], and indicated that all weak interactions were mediated by charged W-bosons. In 1964 Gell-Mann and Zweig introduced three quarks in order to classify the new particles. And in 1967 S. Weinberg and A. Salam published the electroweak unification theory. In the years after, all models, theories and discoveries were collected and presented as the Standard Model (SM). Predictions of this theory were searched for and found in experiments all over the world, the most important being the discovery of the W and Z-bosons and the bottom and top quarks. Unveiling the secrets of matter has been a major task for modern physics, and still is.

One of the most important contributors to modern particle physics experiments is the European Organization for Nuclear Research, CERN. Situated on the border

[1] Democritus was the student of Leucippus and became more famous than his teacher. Aristotle however credits Leucippus with the invention of Atomism

[2] Julian Schwinger and Sidney Bludman present similar ideas in separate papers

between Switzerland and France it has become a center for particle physics research worldwide. A new particle accelerator called the Large Hadron Collider (LHC) is under construction at CERN, and is expected to be operative by 2007. The main goal of this facility is to search for the Higgs-boson, who's existence is necessary in order for other particles to acquire mass. Present day theories are not regarded as the complete description of elementary particles. The LHC will also be used to search for evidence of new theories and symmetries of particle physics, among them extra dimensions and supersymmetry.

Supersymmetry, or SUSY for short, was developed thirty years ago by three independent research groups[3]. Because of its elegancy and ability to solve problems in particle physics it is considered the most promising extension of the Standard Model. SUSY predicts additional particles to the ones already discovered, but these are not yet found. If SUSY is the correct description of nature, supersymmetric particles are expected to be discovered at the LHC.

This thesis will span three aspects related to searches for supersymmetry at the LHC; detector response, identification of a decay chain and mass measurements.

Chapter 1 will give a short introduction to the present theory of particle physics, the Standard Model, and to supersymmetry. Chapter 2 concerns the experimental apparatus, the particle accelerator, LHC, and the particle detector, ATLAS. Since the experiment is still under construction, the investigations in this thesis are based on computer simulation programs. Some knowledge of these programs is necessary in order to understand the data they produce. Chapter 3 gives a short introduction to Monte Carlo event generators and detector simulation programs. The chapter will also investigate how the detector simulation preforms in measuring evidence for supersymmetry. The final goal of this thesis is to attempt to measure masses of SUSY particles. Special features of supersymmetric events require the identification of a distinct decay mode for mass measurements to be possible. In chapter 4 different properties of such a decay chain is studied. Particular characteristics are used to distinguish the decay chain from competing processes. Studies are also made of how well the decay chain we study (signal) can be separated from those processes (background). When the decay chain is properly identified and isolated from the background, mass measurements can start. Chapter 5 illustrates how to measure the unknown masses of SUSY particles, and gives an estimate on how well these masses can be measured only after six months of data taking at the LHC.

[3] 1.Golfand and Likhtman (1971) 2.Volkov, Akulov and Sorokov (1973) 3.Zumino and Wess (1973)

Contents

Chapter 1

Particle physics today

Particle physics seek to explore the fundamental constituents of matter and the forces acting between them. Two approaches to scientific investigations in physics are common. One is to rely on a mathematical descriptive theory to predict phenomena that can be confirmed experimentally. The other is to start with observations, inexplicable by existing theories, and try to find a description that fits. The development of particle physics is an alternation between these two approaches. It was motivated by the need of a theory that could describe the observed phenomena, and has been confirmed and further developed by experimental data.

An experimentalist has to be well acquainted with her theory in order to fully utilize and understand experimental data. This chapter provides a brief introduction to the Standard Model, by presenting its particle content and interactions, the Higgs mechanism and some problems of the theory. A similar introduction to supersymmetry follows, with special weight on the minimal supersymmetric extension of the standard model.

1.1 The Standard Model of Particle Physics

In the first half of the 20th century a myriad of different short-lived particles were discovered. The prevailing hypothesis of that time proclaimed that the basic building blocks of matter were the constituents of the atom; the proton, neutron and electron. Unable to explain the existence of other kind of particles from this hypothesis physicists started searching for new explanations. Among the new developments were the association of forces with boson exchange and the quark model. These ideas were the starting point of the Standard Model of Particle Physics (SM), which is the present theory of forces and particles.

1.1.1 Particles and Interactions

Elementary particles[1] can be divided into two kinds, fermions that have spin one half, and bosons of integer spin. Fermions build up matter and are therefore referred to as matter particles. Elementary bosons do not form matter but mediate forces between the fermions.

Four forces describe all possible interactions between matter. They are the electromagnetic force, the weak force, the strong force and gravity. Each force is mediated by bosons called force carriers. Every force has its own force carriers. One photon for the electromagnetic force, Z^0 and $W^{\pm}$ for the weak force and eight gluons for the strong force, see table (1.1). The Standard Model describes the electroweak and strong force.

[1] "Elementary particle" - particle without internal structure

Interaction	Particle	Mass (GeV)
Electromagnetic	γ (photon)	0
Weak	$W^{\pm}$, Z_0	80.22, 91.19
Strong	g (gluon)	0

Table 1.1: Force mediaters in the Standard Model

1^{st} generation	$\begin{pmatrix} \nu_e \\ e^- \end{pmatrix}$	$\begin{pmatrix} u \\ d \end{pmatrix}$
2^{nd} generation	$\begin{pmatrix} \nu_\mu \\ \mu^- \end{pmatrix}$	$\begin{pmatrix} c \\ s \end{pmatrix}$
3^{rd} generation	$\begin{pmatrix} \nu_\tau \\ \tau^- \end{pmatrix}$	$\begin{pmatrix} t \\ b \end{pmatrix}$

Table 1.2: The three generation of fermions in the standard model.

Gravity is not yet included and is also negligible in strength compared to the other forces.

There are two types of fundamental fermions; leptons and quarks. Both leptons and quarks come in three generations as table (1.2) shows. The classification of fermions in doublets are due to SU(2)[2] weak isospin symmetry. Each member in a doublet has the same value of isospin. Charged currents of the weak interaction also couple equally to quarks and leptons within the same generation[3].

Quarks are divided into two kinds; the up-type quarks, u (up), c (charm) and t(top), with electrical charge $2/3e$, and the down-type quarks, d(down), s (strange) and b(bottom), with charge $-1/3e$. The quark masses range from approximately $m_u =$ 0.005 GeV - $m_t = 174$ GeV. They have three colour degrees of freedom, and can be either red, green or blue. Quarks undergo all three interactions in the Standard Model, and are the only particles that interact through the strong force.

Because of a feature of the strong force called confinement we do not see free quarks. They always come in colour-less bound states of baryons or mesons. Baryons consist of three quarks (qqq), and examples of such particles are the constituents of the atomic nucleus. The proton consists of three quarks, two u-quarks and one d-quark, p(uud), and the neutron consist of two d-quarks and one u-quark, n(ddu). There are also a myriad of unstable baryons for instance Δ^{++}(uuu). Mesons are combinations of quark anti-quark pairs ($q\bar{q}$) the lightest mesons are the pions $\pi^{\pm}(u\bar{d}, d\bar{u})$ and $\pi^0(\frac{1}{\sqrt{2}}(u\bar{u}-d\bar{d}))$.

All leptons have integer electrical charge. The electron, muon and tauon have negative charge $-e$, while the neutrinos are neutral with charge $0e$. Leptons exist in free states, and the electrons are stable enough to be part of atoms. Lepton masses range from $m_e = 0.00051$ GeV to $m_\tau = 1.7771$ GeV. The neutrinos are considered massless even though the Super Kamiokande experiment in Japan [34] has found evidence for neutrino oscillations, for which mass is a prerequisite. The difference between the charged leptons and the neutrinos also reveals itself when it comes to their interactions; neutrinos only interact weakly, while the remaining leptons interact both weakly and electromagnetically.

Particle interactions are described by powerful symmetry demands on Lagrangians. The Lagrangian formalism from classical mechanics is transferred to relativistic quan-

[2]SU(n)-groups are special unitary Lie-groups, special in the sense that the determinants in the fundamental matrix representation are one

[3]When quark mixing is considered!

tum mechanics by replacing the generalized discrete coordinates q_i by continuous fields $\phi(x_\mu)$, as equation (1.1) shows.

$$L(q_i, \dot{q}_i, t) \rightarrow \mathscr{L}(\phi(x_\mu), \frac{\partial \phi}{\partial x_\mu}, x_\mu) \tag{1.1}$$

Lagrangian formalism is well suited for describing the dynamics of a system of particles. Free Lagrangians for leptons and quarks are invariant under global symmetry transformations described by the groups U(1)[4] and SU(3) respectively. By requiring these Lagrangians to be invariant under local symmetry transformations as well, the introduction of vector fields is needed. The vector fields are physically interpreted as force carriers. Local U(1) symmetry requires the introduction of one vector field, the photon, while local SU(3) symmetry requires eight vector fields, the gluons. After the vector fields are introduced they are added to the free Lagrangian. The final Lagrangian describes all possible interactions between the constituent fields (See appendix A for details).

Electromagnetic and weak interactions are unified in the product group $SU(2)_L \times U(1)_Y$, and is referred to as the electroweak interaction. As a consequence of the electroweak unification, exchange of Z^0 and γ occur at the same rate in neutral current processes.

1.1.2 Description of Mass

Photons and gluons are massless gauge bosons, while the bosons of the weak interaction are experimentally found to be massive. This relates to the interaction range of the forces[5]. The electromagnetic and strong force have infinite range, while the weak force is usually approximated to be a point interaction. Mass terms of the gauge fields would destroy the symmetry, and at first sight it seems difficult to give the weak force a gauge description.

A solution to this problem is the Higgs mechanism, which gives mass to vector bosons and fermions while retaining gauge invariance. According to the Higgs mechanism particles acquire masses by interacting with a scalar field present everywhere in the universe, called the Higgs field. The scalar field itself is generated by a massive particle called the Higgs boson. For each massive particle, the strength of the coupling to the Higgs field is proportional to its mass [7].

Mathematically the Higgs field is described as a SU(2) isospin doublet with two complex scalar fields

$$\Phi = \begin{pmatrix} \phi_\alpha \\ \phi_\beta \end{pmatrix} = \sqrt{\frac{1}{2}} \begin{pmatrix} \phi_1 + i\phi_2 \\ \phi_3 + i\phi_4 \end{pmatrix} \tag{1.2}$$

In addition a potential

$$V(\phi) = \mu^2 \phi^\dagger \phi + \lambda (\phi^\dagger \phi)^2 \tag{1.3}$$

is considered. $V(\phi)$ has its minimum at a finite value of $|\phi|$ where

$$|\phi|^2 = \phi^\dagger \phi = \frac{1}{2}(\phi_1^2 + \phi_2^2 + \phi_3^2 + \phi_4^2) = -\frac{\mu^2}{2\lambda} \tag{1.4}$$

There will be many solutions that satisfy equation (1.4) it is also invariant under SU(2) transformations. We now choose a minimum by letting $\phi_1 = \phi_2 = \phi_4 = 0$ so that

$$\phi_3^2 = -\frac{\mu^2}{2\lambda} = v^2 \tag{1.5}$$

[4] U(n)-groups are unitary Lie groups

[5] The range of a force, R, is related to the mass of the gauge bosons, M_X by $R \sim \frac{1}{M_X}$.

The SU(2) symmetry of equation (1.4) is now broken. This way of breaking a symmetry by preferring one solution is called spontaneous symmetry breaking (SSB).

We now expand $\phi(x)$ around this particular vacuum

$$\phi_0 = \sqrt{\frac{1}{2}} \begin{pmatrix} 0 \\ v \end{pmatrix}, \tag{1.6}$$

and finally get an expression for $\phi(x)$ itself

$$\phi(x) = \sqrt{\frac{1}{2}} \begin{pmatrix} 0 \\ v + h(x) \end{pmatrix}. \tag{1.7}$$

Of the four original scalar fields only the Higgs field $h(x)$ remains. In order to determine masses for the gauge bosons, it is sufficient to substitute the vacuum state in equation (1.6) into the Lagrangian describing the interactions between the gauge bosons and the original scalar field, equation (1.2). The Higgs boson is the physical manifestation of $h(x)$, but no experimental evidence for the existence of this particle is found yet.

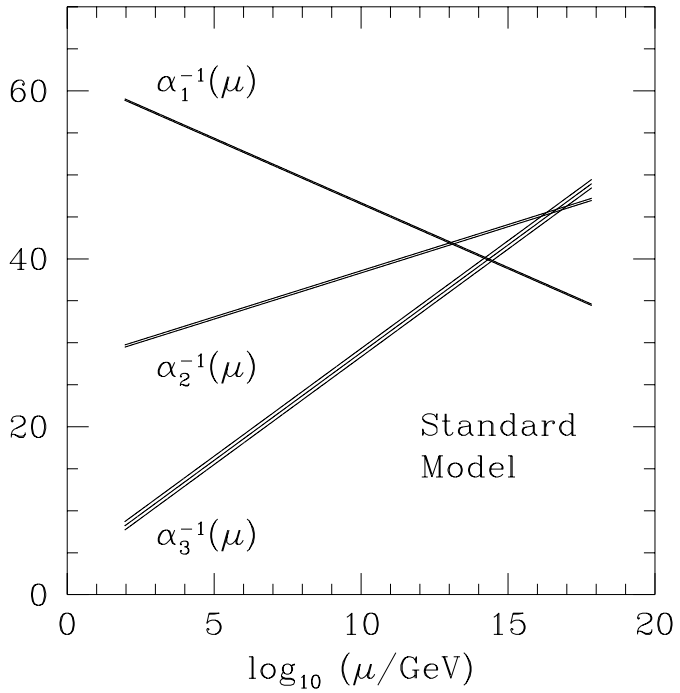

Figure 1.1: The running of the strong, weak and electromagnetic coupling constants in the Standard Model. From [37]

1.1.3 Problems in the Standard Model

Even though the Standard Model is a remarkably successful description of all presently known phenomena, it is clear that it does not provide a complete description of matter [36]. It contains at least 19 arbitrary parameters which is regarded theoretically unsatisfactory. It does not explain why quarks and leptons come with so many different flavours or why there are three generations only. Finally it does not provide any

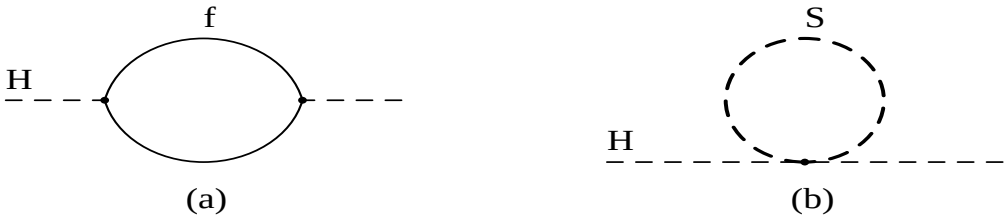

Figure 1.2: Quantum corrections to the Higgs (mass)^2 [36]. (a) a fermion loop and (b) a scalar loop.

description of gravity or unification of the coupling constants of the Standard Model forces. Figure (1.1) illustrates this last point, where the coupling constants of the three SM forces are shown as a function of the log of the momentum transfer. From the figure it becomes clear that the running coupling constants never meet, which means that the Standard Model is not a candidate for a Grand Unified Theory (GUT). The width of the lines are due to experimental uncertainties [37].

An additional problem arises in relation to the Higgs mechanism described in the previous section. Quantum corrections to the Higgs mass are enormous, several orders of magnitude larger than the predicted mass range at $(100\,GeV)^2$ [36]. Figure (1.2a) shows the correction to the Higgs mass squared from a loop containing a fermion of mass m_f. This loop gives a correction:

$$\Delta m_H^2 = \frac{|\lambda_f|^2}{16\pi^2}[-2\Lambda_{UV}^2 + 6m_f^2 \ln \Lambda_{UV}/m_f + \dots], \tag{1.8}$$

where λ_f is the fermion coupling to the Higgs field and Λ_{UV} is an ultraviolet momentum cutoff, interpreted as the energy scale at which new physics appear. If Λ_{UV} is at the Planck scale[6], the corrections to m_H^2 is 35 orders of magnitude larger than the rough estimate $m_H^2 \sim (100 \quad GeV)^2$. Quantum corrections to fermion and gauge boson masses are not quadratic in Λ_{UV}, and large corrections are therefore avoided for these particles. However, every particle in the Standard Model acquire mass from the Higgs field, and is therefore indirectly sensitive to the cutoff Λ_{UV}. This problem is referred to as the technical hierarchy problem, for which the Standard Model does not provide any satisfactory solution.

1.2 Supersymmetry

Supersymmetry is a symmetry that relates bosons and fermions. Mathematically this means that there exists an operator Q transforming bosonic states to fermionic states and vice versa.

$$Q|Boson>=|Fermion>, \qquad Q|Fermion>=|Boson>. \tag{1.9}$$

In order for an operator Q to generate such transformations, it must be a spinor. In addition, Q and its hermitian conjugate $Q^\dagger$ must satisfy an algebra of anti commutation and commutation relations on the form;

$$\begin{array}{rcccl} \{Q, Q^\dagger\} & = & P^\mu & & \\ \{Q, Q\} & = & \{Q^\dagger, Q^\dagger\} & = & 0 \\ [P^\mu, Q] & = & [P^\mu, Q^\dagger] & = & 0 \end{array}$$

[6]The Planck scale is the microscopic scale at which gravity becomes important and a description of quantum gravity is needed. This scale is usually represented by the Planck mass defined as $M_{Pl} \sim \sqrt{\frac{\hbar c}{G_N}} \sim 10^{19} GeV$ [40].

where P^μ is the momentum generator of space-time translations, and spinor indices on Q and $Q^\dagger$ are suppressed.

The particle states of a supersymmetric theory are organized in supermultiplets. A supermultiplet contains both fermions and bosons, where the number of fermionic degrees of freedom equals the bosonic degrees of freedom [36]. Particles belonging to the same supermultiplet are *superpartners* of each other. They have equal masses and the same electric charges, weak isospin, and colour degrees of freedom [36].

1.2.1 Motivations for supersymmetry

The development of supersymmetry was purely theoretically motivated. It was discovered in an attempt to find non-trivial extensions of the Poincare group[7] by using fermionic operators [7]. At the present supersymmetry is considered the best candidate theory for physics beyond the Standard Model. One of its most attractive features is that it provides a solution to the hierarchy problem mentioned in section 1.1.3.

In section 1.1.3 the corrections to m_H through fermion loops were considered. Out of curiosity we also investigate the corrections coming from scalar loops. The existence of a heavy complex scalar particle S with mass m_S would give a correction to the Higgs mass through the loop diagram shown in figure (1.2b). The analytical expression for this correction is

$$\Delta m_H^2 = \frac{\lambda_S}{16\pi^2}[\Lambda_{UV}^2 - 2m_S^2 \ln \Lambda_{UV}/m_S + \dots], \tag{1.10}$$

where λ_S is the scalar coupling to the Higgs field.

By comparing equation (1.8) and (1.10) it is evident that that if every Standard Model fermion was accompanied by two complex scalars with $\lambda_S = |\lambda_f|^2$ the quadratic terms would neatly cancel out [36]. Supersymmetry has this feature since it requires the bosonic and fermionic degrees of freedom to be equal. In a supersymmetric theory all quadratic terms in the corrections to the Higgs mass will be canceled, and there will be no technical hierarchy problem.

Another motivation for SUSY is that it actually causes the Standard Model coupling constants to meet. The running of the SU(3), SU(2) and U(1) gauge coupling constants depends on the particle content in a theory [40]. Figure (1.3) shows that the inclusion of SUSY causes the coupling constants to meet. This is an improvement of the situation in figure (1.1), which contained the Standard Model particles only. A common value of the coupling constants from some energy scale is requisite for a Grand Unified Theory (GUT), since the aim of a GUT is to unify the three SM forces.

1.2.2 The minimal supersymmetric standard model

The minimal supersymmetric standard model (MSSM) is a possible extension of the Standard Model to a supersymmetric theory of minimum particle content. In the MSSM every Standard Model particle has one superpartner, these are often referred to as sparticles. According to this theory none of the known particles are superpartners of each other, because their internal quantum numbers do not match. Quarks, for instance, come in colour triplets, while the known bosons are either colour singlets or octets [35]. As a result the MSSM will at least double the number of fundamental particles in nature.

As already mentioned, the SM and SUSY particles will be organized in supermultiplets. Supermultiplets come in two kinds; chiral or matter supermultiplets containing leptons, quarks and their superpartners, and gauge supermultiplets containing the gauge bosons and their superpartners. The members of a supermultiplet have spins

[7]The Poincare group is a 10-dimensional Lie group having both the Lorentz group and the group of translations as subgroups [41]

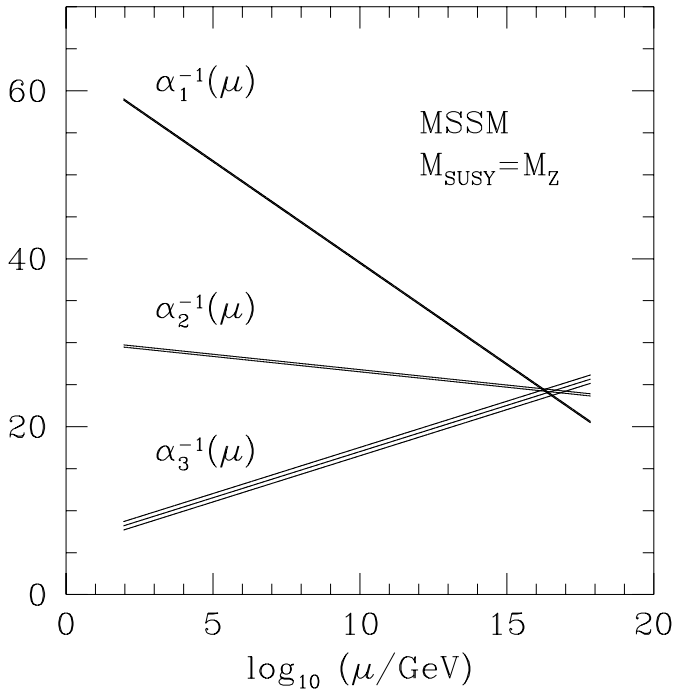

Figure 1.3: Running of the Standard Model coupling constants with supersymmetry [37]

Particles		spin 0	spin $\frac{1}{2}$
squarks, quarks ($\times$ 3 families)	Q $\bar{u}$ $\bar{d}$	$(\tilde{u}_L \quad \tilde{d}_L)$ $\tilde{u}^*$ $\tilde{d}^*$	$(u_L \quad d_L)$ $u_R^\dagger$ $d_R^\dagger$
sleptons, leptons ($\times$ 3 families)	L $\bar{e}$	$(\tilde{\nu} \quad \tilde{e}_L)$ $\tilde{e}_R^*$	$(\nu \quad e_L)$ $e_R^\dagger$
Higgs, Higgsinos	H_u H_d	$(H_u^+ \quad H_u^0)$ $(H_d^+ \quad H_d^0)$	$(\tilde{H}_u^+ \quad \tilde{H}_u^0)$ $(\tilde{H}_d^+ \quad \tilde{H}_d^0)$

Table 1.3: MSSM chiral supermultiplets

that differs by a half, so that chiral supermultiplets consists of spin-zero and spin-half particles, while gauge supermultiplets consist of spin one bosons and their spin-half partners.

Any supersymmetric particle is symbolically distinguished from its Standard Model partner by placing a tilde over the particle symbol. The supersymmetric partner of the electron; e^-, is for instance written $\tilde{e}^-$. The partners of the SM fermions are all scalars and this is reflected in their names, scalar leptons are called sleptons and scalar quarks are called squarks. Also individual particle names follow this scheme, so the partner of the electron is called selectron and the partner of the top-quark is called stop etc.

Fermions have two spin (or chirality) states. Since the fermionic and bosonic degrees of freedom, in a supersymmetric theory, are equal each SM fermion has two scalar partners. Right- and left-handed fermions, f_L and f_R have 'right' and 'left'-handed sfermions, $\tilde{f}_L$ and $\tilde{f}_R$, as partners. Even though the sfermions are denoted in this way they do not have any 'handedness' themselves since they are scalar particles. The label refers to the chirality of their fermionic partners.

The partners of the third generation quarks and leptons are denoted according to their handedness, due to their large left-right mixing[8]. Stops, sbottoms and staus are usually denoted with subscripts 1 and 2 to separate the lighter and heavier state respectively [40]. The lightest stop is for instance denoted $\tilde{t}_1$. Table (1.3) summarizes the chiral supermultiplets in the MSSM.

Particles	spin $\frac{1}{2}$	spin 1
gluino, gluon	$\tilde{g}$	g
wino, W bosons	$\tilde{W}^{\pm}$, $\tilde{W}^0$	$W^{\pm}$, W^0
bino, B boson	$\tilde{B}^0$	B^0

Table 1.4: Gauge supermultiplets in the MSSM

The vector bosons in the Standard Model are integer-spin particles. They belong to gauge supermultiplets and have half-spin partners. Table (1.4) shows the SM gauge bosons their corresponding fermionic partners called gauginos. The particles in table (1.4) corresponds to unbroken $SU(3) \times SU(2) \times U(1)$ and the SUSY partners are called gluinos, winos and bino respectively.

In the Standard Model the existence of a single Higgs doublet is postulated. The SM Higgs boson is a scalar particle and would therefore be placed in a chiral supermultiplet. Supersymmetry however, requires two Higgs doublets in order to give mass to both up-type and down-type quarks [40]. Five physical Higgs bosons remains after electroweak symmetry breaking, a charged and neutral pair of scalars; $H^{\pm}$ and H, h, respectively, and a neutral pseudoscalar A. Each of these particles have spin-half partners, the Higgsinos. Higgsinos mix with the winos and bino to form mass eigenstates. The charged Higgsinos and winos mix to two particles called *charginos*, $\tilde{\chi}_1^{\pm}$ and $\tilde{\chi}_2^{\pm}$. The two neutral Higgsinos mix with the neutral wino and bino and form four neutral particles called *neutralinos*, $\tilde{\chi}_1^0$, $\tilde{\chi}_2^0$, $\tilde{\chi}_3^0$ and $\tilde{\chi}_4^0$.

[8] After the electroweak symmetry breaking the Lagrangian contains terms $(\tilde{f}_L^* \quad \tilde{f}_R^*)\mathbf{m_{\tilde{f}}^2} \begin{pmatrix} \tilde{f}_L \\ \tilde{f}_R \end{pmatrix}$, where $\tilde{f}_{L,R}$ are gauge eigenstates. The (mass)^2-matrix, $\mathbf{m_{\tilde{f}}^2}$, has off-diagonal terms containing SM Yukawa couplings. These are negligible for the lighter fermions, but becomes large for the third generation, causing the left and right gauge eigenstates to mix. The matrix $\mathbf{m_{\tilde{f}}^2}$ can be diagonalized to give mass eigenstates $\begin{pmatrix} \tilde{f}_1 \\ \tilde{f}_2 \end{pmatrix} = \begin{pmatrix} \cos\theta_{\tilde{f}} & \sin\theta_{\tilde{f}} \\ -\sin\theta_{\tilde{f}} & \cos\theta_{\tilde{f}} \end{pmatrix} \begin{pmatrix} \tilde{f}_L \\ \tilde{f}_R \end{pmatrix}$, where $\tilde{f}$ is $\tilde{t}$, $\tilde{b}$ or $\tilde{\tau}$ [36].

1.2.3 R-parity

As seen in table (1.3) of section 1.2.2 the MSSM does not distinguish between quark/lepton fields and Higgs fields. As a consequence baryon- and lepton-number are not necessarily conserved. In order to preserve these conservations laws a discrete symmetry called R-parity is introduced:

$$R_P = (-1)^{3B+L+2s}, \tag{1.11}$$

where B is the baryon number, L the lepton number and s the spin of the particle. Thus Standard Model particles always have $R_P = +1$ while their superpartners have $R_P = -1$.

If R-parity is conserved sparticles will be produced in pairs and must decay to states which contain an odd number of sparticles. This implies that the lightest supersymmetric particle (LSP) is stable and weakly interacting. Each SUSY event will then produce an even number of LSPs that are only 'visible' through the large missing transverse energy (E_T^{miss}) they generate. Only R-parity conserving (RPC) scenarios will be studied in this thesis.

1.2.4 mSUGRA

In the unbroken minimal supersymmetric extension of the Standard Model, particles and sparticles in the same supermultiplet differ only by their spin quantum number. This means that the Standard Model particles and their partners should have the same mass. No scalar particles with the same mass as the SM fermions, or spin-half gauginos with the same mass as the vector bosons, have been discovered yet, and SUSY must be broken. There exists several models of supersymmetry breaking. The most common are by flavour-blind gravitational (mSUGRA), or gauge (GMSB) interactions [40].

If supersymmetry exists, even the lightest SUSY particle must be heavier than its SM partner. In order to achieve this, supersymmetry must be broken in a 'hidden' sector of fields isolated from SM particles and interactions [40]. Supersymmetry breaking is rather technical and no details will be given. A short description of mSUGRA which is the SUSY breaking model used in this thesis follows below.

In the minimal supergravity model (mSUGRA) supersymmetry is a local rather than a global symmetry [7]. It assumes that at the GUT-scale[9] all scalar particles have a common mass m_0, all gauginos and Higgsinos have a common mass $m_{\frac{1}{2}}$, and that all Higgs-sfermion-sfermion couplings have a common value A_0 [1]. In addition the ratio of Higgs vacuum expectation values $\tan\beta = \frac{\nu_u}{\nu_d}$, and the sign of the μ-parameter is used as input in the theory. mSUGRA reduces the number of parameters from 105 to 5, these are summarized below.

1. m_0 -common scalar mass.
2. $m_{\frac{1}{2}}$ -common gaugino and Higgsino mass.
3. A_0 -common Higgs-sfermion-sfermion coupling.
4. $\tan\beta$ - Higgs vacuum expectation value.
5. μ - sign of the μ-parameter.

These five parameters determines the masses and mixing of all SUSY particles and thereby indirectly their decays.

[9] The GUT-scale is defined as the energy scale where the coupling constants become equal. For the MSSM this happens at $\sim 10^{16}$GeV

1.2.5 Supersymmetry -the perfect model of nature?

Unfortunately there exists no model that describes nature perfectly, and supersymmetry is no exception. The greatest disadvantage of SUSY is that it is not experimentally confirmed. Experiments at CERN and Fermilab have so far failed to find evidence for it. It could of course be that the accessible energies at these experiments were out of range for SUSY discoveries, but it could also be that SUSY has not yet been found simply because it is not there.

Another disadvantage is the ad hoc introduction of R-parity in order to avoid interactions with baryon and lepton number violation. The fact that SUSY allows interactions that contradict experimental results could also be an indication of the theory not being the right description of nature.

Despite its disadvantages, SUSY is still one of the most popular extensions of the Standard Model. After all it does manage to solve many important problems and is well founded within the framework of existing and successful theories. Whether SUSY is a true symmetry of nature is left for the experiments at the LHC to find out.

Chapter 2

The ATLAS detector

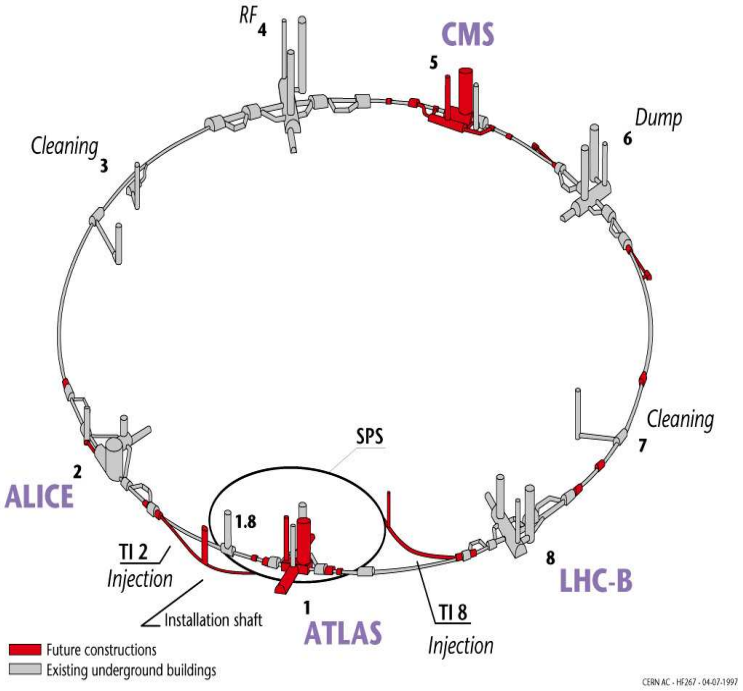

Figure 2.1: Underground accelerator system at CERN

2.1 The Large Hadron Collider

The Large Hadron Collider (LHC) at CERN is a circular particle accelerator designed to collide protons with a center of mass energy of 14 TeV. It is currently installed in a circular ring of radius 4 km, located hundred meters under ground on the French/Swiss border. Installation will be completed in 2007.

CERN contains a complex system of accelerators that will be in use when the LHC

starts running. Figure (2.1) shows the two largest accelerators, the LHC itself and the smaller SPS[1], together with the detector caverns. Before the protons are injected to the LHC ring they are accelerated to 450 GeV by smaller accelerators. The LHC accelerate each beam from the injection energy to 7 TeV [7]. The particles are accelerated by strong electric fields. While superconducting dipole magnets, cooled to temperatures below 2 K, provide an 8 Tesla magnetic field to bend the beams.

In addition to the large center of mass energy the LHC is also intended for operation with a large beam luminosity[2]. Design luminosity is $10^{34} cm^{-2} s^{-1}$, but during the first three years LHC will run at low luminosity which is a factor of ten less.

Protons will collide at four different, intersecting, points in the ring. Detectors are built at the collision points. The two largest, ATLAS and CMS, are multi purpose detectors while, LHCb and ALICE are designed for studies of B-physics and heavy ion physics respectively.

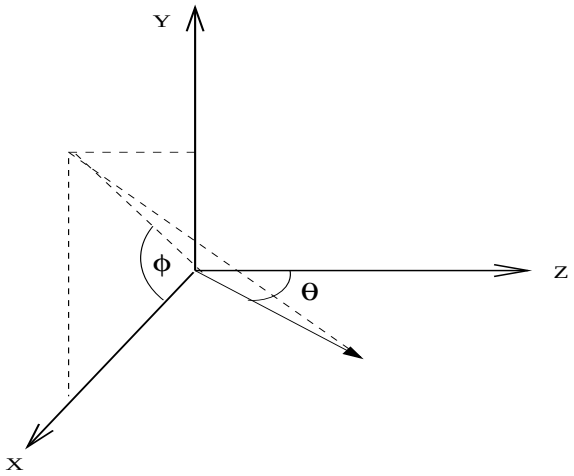

Figure 2.2: ATLAS coordinate system.

2.1.1 Nomenclature

A well defined coordinate system is necessary in order to properly describe the detector and the events it records. An illustration of the LHC coordinate system is shown in figure (2.2). The positive x-axis points toward the center of the ring while the positive y-axis points upward. This determines the positive z-axis, that will be parallel to the beams [1]. The azimuthal angle ϕ is measured around the z-axis and the polar angle θ is the angle from the z-axis, see figure (2.2).

Another important variable is the pseudorapidity, defined as

$$\eta = -\ln \tan \frac{\theta}{2}. \tag{2.1}$$

The pseudorapidity can be seen as a variable that indicates closeness to the beam. Small pseudorapidities are related to a large polar angles and vice versa.

[1] Super Proton Synchrotron

[2] Luminosity -number of particles per square-centimeter per second in a beam.

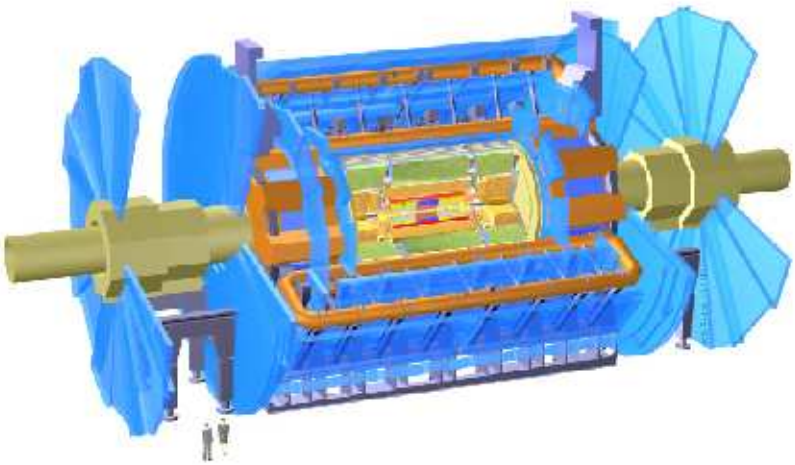

Figure 2.3: The ATLAS detector

2.2 ATLAS design and purpose

ATLAS [1] is an abbreviation for **A T**oroidal **L**HC **A**pparatu**S** and is the largest[3] of the four detectors at the LHC [1]. It is shaped like a cylinder and centered around the beam line. It will be used for Standard Model tests, for Higgs searches and investigations of new physics, like supersymmetry. ATLAS consists of different parts, each with a specific purpose. These are mainly the inner detector, the calorimeters and the muon chambers. The main detectors can again be divided into smaller, more specialized sub-detectors. A short description of the detector system follows.

2.2.1 Inner detector [1]

The inner detector is contained in a 7 m long cylinder of radius 1.5 m. It operates in a strong magnetic field of 2 T provided by the central solenoid. The main purposes of this detector are pattern recognition, electron identification and measurements of momentum and vertices. It consists of two high granularity detectors, the Pixel and Semi Conductor Tracker, and a low granularity detector, the Transition Radiation Tracker. The high granularity detectors perform relatively few precise measurements, while the low granularity detector compensates for its lack of precision with many measurements.

Pixel detector [1]

The pixel detector consists of 140 million $50\,\mu m \times 400\,\mu m$ silicon pixels. Its purpose is to give high precision measurements as close to the collision point as possible. The innermost barrel will be 5 cm from the beams. The system provides three measurements for each track.

[3] length 45 m, height 22 m

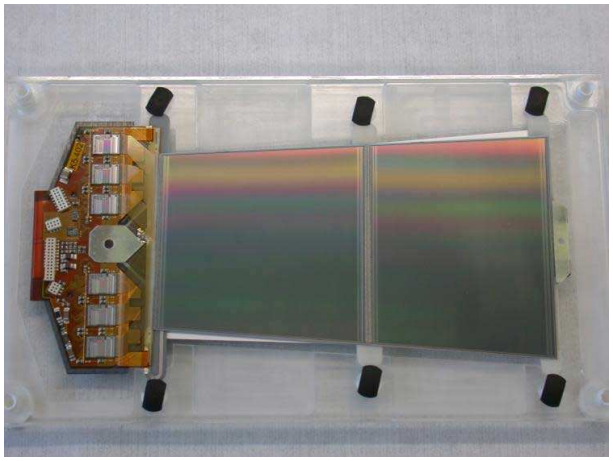

Figure 2.4: Detector module of the semiconductor tracker

Semiconductor tracker [1]

The Semiconductor tracker, SCT, consists of silicon micro-strip detectors. A SCT module, illustrated in figure (2.4), consists of four $6.36 \times 6.40\,cm^2$ silicon detectors. The two pairs are glued back to back, displaced by a 40 mrad angle. Eight layers of micro-strips provide eight precision measurements that contribute to the determination of momentum, impact parameter and vertex position.

Transition radiation tracker [1]

The Transition radiation tracker, TRT, uses straw detectors. Each straw is 4 mm in diameter, and is filled with a gas mixture of Xenon, CO_2 and O_2. The detector system will once in a while be flushed with CF_4 to promote electron drift velocity and delay aging [7]. Every straw is equipped with a sense wire in the center of the gas volume. Low precision is balanced by a large number of measurements, typically 36 for each track. Electron identification capability is added to the TRT through use of Xenon gas. It detects transition radiation photons created in plastic layers between the straws. Readout channels provide two independent thresholds for each straw. These allow the detector to discriminate between tracking hits, passing the lower threshold, and transition-radiation hits, passing the higher one.

2.2.2 Calorimeters

The ATLAS calorimeters are of two kinds, the electromagnetic calorimeter and the hadronic calorimeter. The electromagnetic part measures the energy of electrons, positrons and photons, while the hadronic part measures the total energy of hadrons.

Electromagnetic calorimeter [1]

The electromagnetic calorimeter is a sampling calorimeter that uses lead as absorber and liquid Argon as active material. The absorber plates have an accordion geometry, that provides full ϕ symmetry and hermeticity, and is a new technique made for large scale use in ATLAS. Most particles will suffer a significant energy loss in the inner detector, the solenoid coil and the cryostat. Finely segmented presamplers are therefore placed in front of the accordion calorimeters to compensate for the energy loss and for calibration purposes [8].

The barrel part of the calorimeter $|\eta| < 1.475$ consists of two identical half barrels separated by a 6 mm gap at $z = 0$. It is contained in the barrel cryostat that surrounds

the inner detector. The end cap calorimeters are contained in the end cap cryostat and subdivided into two coaxial wheels.

The electromagnetic calorimeter provides three energy samplings. The central part of the calorimeter, $|\eta| < 2.5$, is divided into three longitudinal sections. The first section is segmented into very narrow strips and acts as a preshower detector, enhancing particle identification and providing a precise η measurement. The next section is transversally segmented into square towers of size $\Delta\eta \times \Delta\phi = 0.025 \times 0.025$ while the last section has a granularity of 0.05 in η.

Hadronic calorimeter

The central part of the hadronic calorimeter, $|\eta| \leq 2.5$, is a sampling scintillation detector. Certain materials emit a small flash of light when traversed by electrically charged particles, they scintillate. When these materials are connected to a photomultiplier the light is transformed into electrical pulses which can be counted electronically and in that way give information on the incident radiation. In a sampling scintillator only a fraction of the energy deposited in the absorber is measured.

Plastic scintillator tiles contained in steel absorbers are used in ATLAS. These tiles are divided into cells and placed perpendicular to the beams. Scintillators are vulnerable to the large radiation at $|\eta| > 2.5$, so the Liquid Argon (LAr) technology is used instead.

The calorimeter thickness is of severe importance since it must give room for hardronic showers and reduce leakage into the muon system. At $|\eta| = 0$ the total thickness is 11 interaction lengths[4], λ, that corresponds to roughly 2.0 m, where approximately 10λ is active calorimeter and the rest is dead material. This is enough to give a satisfactory resolution for high energy jets. A good η coverage will also provide high quality missing transverse energy measurements.

2.2.3 Muon chambers [1]

Outside the calorimeters one finds the Muon Toroidal Magnets which bend the paths of the far reaching muons. The space between the Muon Toroidal Magnets are equipped with triggers and high precision tracking chambers. For $|\eta| < 1.0$ the muon trajectories are bent by the barrel toroid, and in the region $1.4 \leq |\eta| \leq 2.7$ they are bent by end cap magnets. In between, the tracks are bent by the combined field from both barrel and end cap magnets. The magnet configuration gives a field perpendicular to the muon trajectories.

The muon system consists of tracking and trigger chambers. The tracking system uses two different detectors, Monitored Drift Tubes in the barrel region and Cathode Strip Chambers at larger η. The trigger system consists of Resistive Plate Chambers in the barrel and Thin Gap Chambers in the end cap region. Chamber positions are optimized for full coverage and momentum resolution. Traversing particles will pass three chambers. The combination of barrel and end cap chambers gives an almost complete coverage in the pseudorapidity range $1.0 < |\eta| < 2.7$. There is an opening in the central $R - \phi$ plane ($\eta = 0$) to give exit for cables from the inner detector and the calorimeters.

A short description of the different muon chambers follows below:

Monitored Drift Tubes (MDT) [1]

The MDTs consist of small aluminum tubes, 30 mm in diameter. The tubes are filled with a non-flammable gas mixture of 93% Argon and 7%CO_2 at a pressure of 3 bar. Each tube has a read out in the end with a threshold five times larger than noise level.

[4]The interaction length is defined as the mean free path of a particle before interacting with the material in a given medium. For plastic scintillators $\lambda \approx 82.0 g/cm^2$ [9]

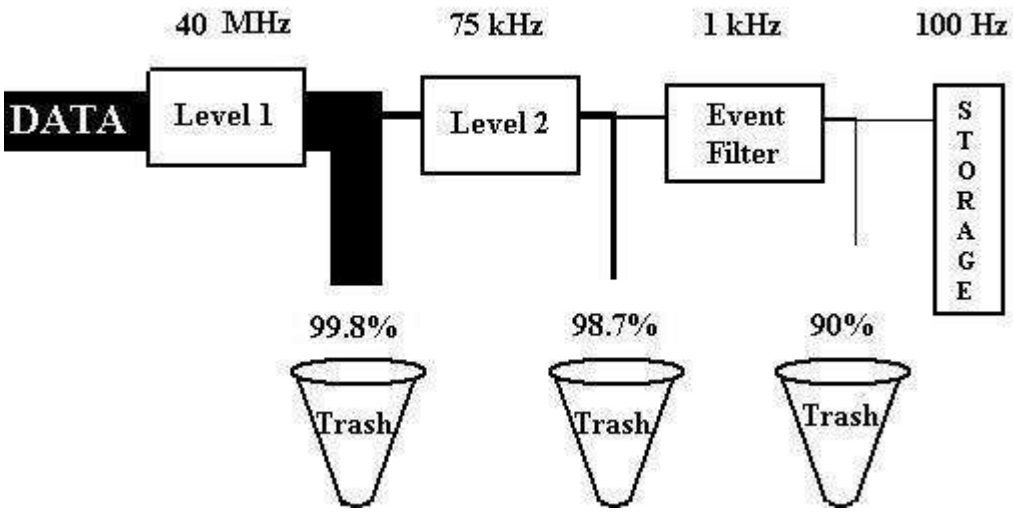

Figure 2.5: Data reduction in the ATLAS trigger system

Cathode Strip Chambers (CSC) [1]

The CSCs are multi-wire proportional chambers with cathode strip read out. The precision coordinate is measured through the charge induced on the cathode part. An Argon gas mixture is used as drift gas [7].

Resistive Plate Chambers (RPC) [1]

The RPCs are small gas gaps formed by two parallel Bakelite plates. The gas in between is an environment friendly mixture of thetrafluoretan $C_2H_2F_4$ and a small amount of SF_6.

Thin Gap Chambers (TGC) [1]

The TGCs use the same technology as the CSC. TGC is operated with a flammable gas mixture of 55% CO_2 and 45 % n-pentane ($n - C_5H_{12}$).

2.2.4 Trigger [1]

At the LHC bunches of protons will collide every 25 ns and approximately 25 interactions will occur in each bunch crossing. In fact nearly 10^9 interactions will occur every second at high luminosity. This enormous amount of data needs to be reduced to about 100 events per second for permanent storage. These extreme conditions require a fast and efficient trigger system. The event reduction procedure is illustrated in figure (2.5).

The trigger and data-acquisition system in ATLAS is based on three levels of online event selection. Each trigger level has a set of selection criteria usually based on the previous level.

Level 1: A hardware based trigger where selections are based on reduced-granularity information from a subset of detectors. Searches for high p_T electrons, photons, jets and τ-leptons.

Level 2: Operates on events that pass level 1 only, and use so called Region of Interest information (η, ϕ and p_T) provided by level 1. Rejects more events by using the full granularity calorimeters and sharpening the p_T thresholds.

Event Filter: Makes the final selection of physics events. Will confirm the level 2 decisions. Further rejection of the data will come from more specialized cuts and complex algorithms.

2.3 Measuring SUSY with ATLAS

As we will see later supersymmetric processes are characterized by multiple jets, leptons and missing transverse energy E_T^{miss}. ATLAS must be able to determine these measureables in a precise and correct way in order for supersymmetry to be discovered.

2.3.1 Jet identification

Jet reconstruction is particularly important for SUSY measurements. Most SUSY events are followed by one or two hard jets[5]. It is important to measure these jets, especially in relation to mass measurements. Badly measured jets could cause fake missing energy which could cause an increase of background. Hermeticity and good η coverage are essential to avoid these problems.

There exist at least three different jet algorithms that are tested for use in ATLAS. These are the cone algorithm, the K_T clustering algorithm and the MGS algorithm. Only the cone algorithm will be used in this thesis, the others are included for completeness.

The cone algorithm [10]: The calorimeter tower with the largest value of E_T is chosen as a jet seed. A cone of radius R is then built around the seed. Calorimeter cells that lie inside the cone are taken as a part of the jet. Cells belonging to a cone are not available for further jet searches.

K_T **clustering algorithm**[6] [10]: Initially every calorimeter cell is considered a protojet. The distance, $d_{ij} = min(E_{Ti}^2, E_{Tj}^2)(\Delta\eta_{ij}^2 + \Delta\phi_{ij}^2)$, between all protojets is calculated, as well as its "closeness" to the beam direction. For every protojet i the closeness is defined as: $d_{ib} = E_{Ti}^2 R_{CUT}^2$, R_{CUT} is a parameter. The minimum of all distances or closeness parameters is then defined as d_{min}. If d_{min} is identical to a distance between two jets, the two jets are merged into a new protojet and the process is repeated. If d_{min} is equal to the closeness d_{ib}, protojet i is not mergeable and is added to the list of jets. Finally a cut on the minimum E_T is applied and only clusters passing the cut are kept.

MGS algorithm [10]: The maximum E_T cell is found and defined as the first cluster, the initial cluster size is set equal to the resolution. Next the cell with the second largest E_T is found. The distance between the cell and the closest cluster is calculated. If this distance is smaller than the cluster size, the cell and the cluster are combined. If the distance is larger than the cluster size, the cell is defined to be a new cluster. The procedure continues until there are no more cells left.

2.3.2 Lepton identification

Two same flavour, opposite charged, leptons are part of the detectable decay products of some SUSY processes. The combination of invariant masses of leptons and jets gives, as we will see later, important information on the sparticle masses.

Electron identification is a combined task for the inner detector and the EM calorimeter. The common procedure is to match hits in the electromagnetic calorimeter with a

[5] "Hard jets" denote jets with large transverse energy
[6] Montreal version [10]

track in the Inner Detector. Electromagnetic showers provide electron-jet separation, since showers produced by electrons will be fully contained in the calorimeter. In addition, it will be possible to calculate E/p for electron candidates, where the energy E is measured by the calorimeter and the momentum p is measured by the inner detector. In an ideal world this ratio would be one, but due to bremsstrahlung not all electron momenta are correctly measured by the Inner Detector. This causes the value of E/p to slightly fluctuate around one, $E/p \in (0.96 - 1.04)$ [1]. The TRT will also contribute to electron identification through transition radiation measurements. If all sub-detectors operate as intended, the electron identification performance is estimated to give an overall electron efficiency of 68.6%, for electrons with $p_T = 20GeV$ [1].

Muon identification is done by matching tracks in the Inner Detector with tracks in the muon system. Muons are the only detectable particles produced at the collision point that will reach the muon system. Some muons could also arise from decay of π-mesons or originate from jets. The information from both the inner tracking detectors and the muon system makes it possible to distinguish between muons from primary and secondary vertices.

2.3.3 Missing transverse energy E_T^{miss}

Protons will collide at a center of mass energy of 14 TeV at the LHC. Being composite structures, it is not known how the collision energy is distributed between their constituents. However, the initial transverse energy, $E_T = E \sin\theta$, is approximately zero. Conservation of energy requires the final E_T to be zero as well. If all final particles were detectable and their transverse energy measured correctly by the detector, the sum over E_T for all of them should then be zero. Very weakly interacting particles, like neutrinos and the lightest stable supersymmetric particle, will escape the detector and no energy measurement will be made for them, in that case

$$\Sigma E_T \neq 0. \tag{2.2}$$

The missing transverse energy, E_T^{miss}, is the energy of the escaped particles, the number missing in order for the sum in equation (2.2) to be zero. The crucial elements for a satisfactory E_T^{miss} resolution are obviously hermeticity, a sufficient pseudorapidity coverage and accurate calibration of all calorimeters. The calibration should account for non-compensation[7], energy losses in material in front of the calorimeters and cracks. In addition the cell energy cut-off has to be carefully tuned in order to avoid contributions from low-energy cells, like cells outside jets.

[7]The calorimeter respond differently to electromagnetic and hadronic signals, typically $e/h \approx 1.1 - 1.35$ [11]. This non-compensation has to be taken into account when the calorimeter is calibrated.

Chapter 3

Event generators and detector simulations

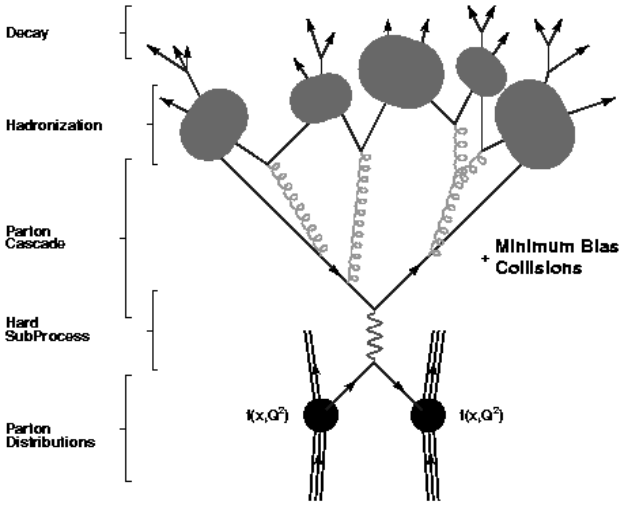

Figure 3.1: Schematic presentation of the basic structure of a generated pp-event including showering and hadronization [16].

Many preparations must be made by the time the Large Hadron Collider starts running in 2007. Computer simulations play an important role in these preparations. Event generators make it possible to study physics beyond the Standard Model and promote the development of new particle interaction models. Detector simulations may help discover detector design weaknesses while there are still time for improvements. Finally, simulated detectors and particle collisions will mimic the real experiment so that the diversity of physics processes can be analysed in advance.

3.1 Event generators

An event generator is a computer program that produces hypothetical events in agreement with theoretical predictions [15]. The event generators described in this chapter

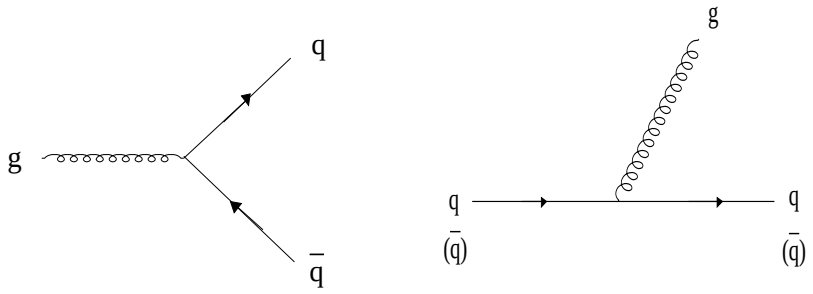

Figure 3.2: Parton splitting mechanisms

are referred to as showering and hadronization generators(SHGs).

For simulation of proton collisions the SHGs begin with a leading order hard subprocess. A hard subprocess is the fundamental particle interaction, usually a $2 \rightarrow 2$ scattering process [20], for instance $u\bar{u} \rightarrow Z^0 \rightarrow d\bar{d}$ [15]. Higher order effects are added using parton showers which allow partons[1] to split up into pairs, as illustrated in figure (3.2). The resulting partons are then hadronized, and unstable hadrons are decayed further.

It is not known how free quarks are merged into hadrons, and the event generators use different approaches at this point in the simulation process [7]. The generation of beam remnants and interactions from other partons in the collisions are done simultaneously [15]. Figure (3.1) illustrates the process described above.

3.1.1 Herwig and Pythia

HERWIG [17] and PYTHIA [4] are general purpose Monte Carlo event generators for simulation of lepton and hadron collisions, for instance e^+e^-, ep or pp. They are both written in Fortran[2] and designed in accordance with the idea presented in figure (3.1). One of the most important differences between the two is how the hadronization process is approached. PYTHIA uses the Lund string model [21] while HERWIG uses the cluster hadronization model [15]. Comparison with LEP data shows that the Lund string model gives the best agreement [20].

Both HERWIG and PYTHIA provide a wide variety of processes, including most Standard Model physics, Higgs production, supersymmetry and exotic physics like new gauge bosons and extra dimensions.

3.1.2 Generating Supersymmetry

ISAJET [18] is another widely used multi-purpose SHG. It provides a large range of SUSY models, including the Minimal Supersymmetric extension of the Standard Model (MSSM) and Supergravity (SUGRA). Supergravity models require an iterative solution to the SUSY renormalization group equations [22] and ISAJET provides these solutions up to second order corrections [15]. This feature makes ISAJET the best provider of SUSY parameters and masses. Since the sparticle mases and decay rates are output from the program, they are often used as input in other event generators like PYTHIA and HERWIG.

PYTHIA includes the possibility of simulating a large variety of production and decay processes in the MSSM. SUGRA is also included as a SUSY-breaking mechanism, but PYTHIA uses only an approximate analytical solution of the renormalization group

[1] parton is a generic term for quarks and gluons

[2] c++ versions of both generators are under development

equations. For this reason, calculation of parameters and masses by PHYTHIA in the SUGRA model do not represent state-of-the-art simulations [4]. If PYTHIA is used for event generation in the SUGRA model, masses and decay rates should be provided by ISAJET.

HERWIG does not contain any built-in models for SUSY scenarios beyond the MSSM, such as SUGRA. In all cases the SUSY particle spectrum and decay tables must be provided by input files [17]. ISAWIG is a package that has been created to work with ISAJET, and to produce a file containing the SUSY particle masses, lifetimes and decay modes. ISAWIG takes the output from ISAJET, and produces a data file in a format that can be read by HERWIG.

3.2 Detector Simulation

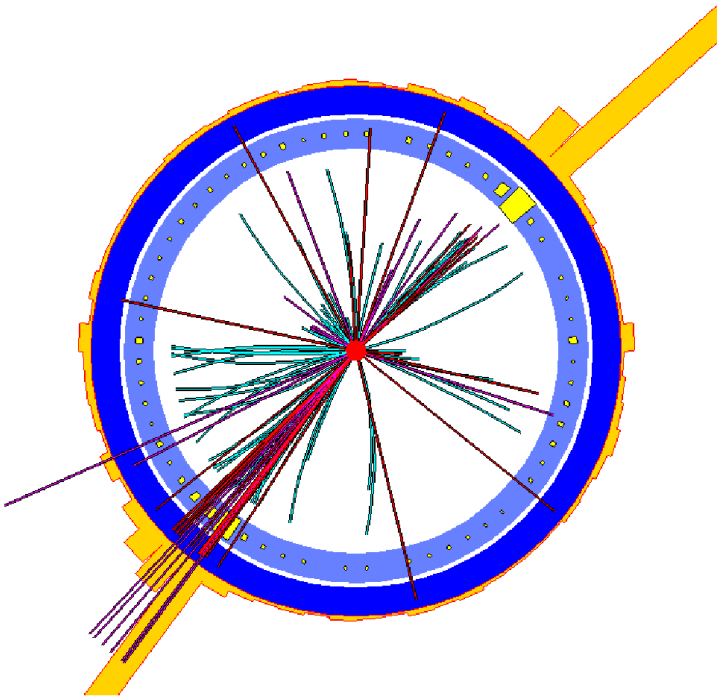

Figure 3.3: The Atlfast detector responding to a hard QCD event. Events like this will be common at the LHC. Image obtained using Athena 8.0.5 and Atlantis 8.0.1

3.2.1 Atlfast [27]

Atlfast is a 'fast' simulation program. Its main purpose is to illustrate good detector response in a minimum amount of time. This makes Atlfast excellent for feasibility and high statistics studies [7].

Simulation and reconstruction in Atlfast is based on the definition of a grid of calorimetric cells in the η and ϕ range. This grid constitutes the Atlfast detector simulation. Simulation of the detector response starts by assigning the energy of generated parti-

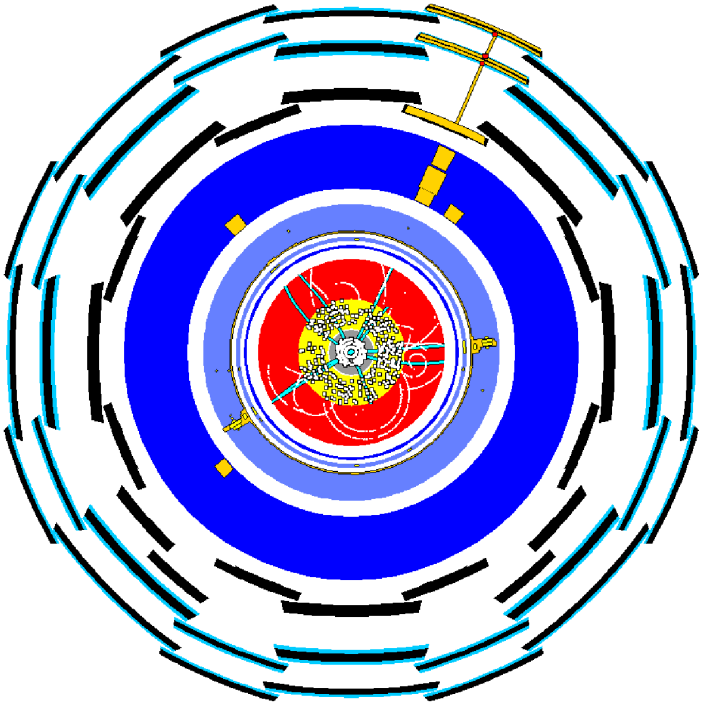

Figure 3.4: Full detector simulation. Example image from atlantis 8.0.1 [32] in a fisheyes view

cles [3] to cells in the grid. The η and ϕ of the generated particles decide to which cells in the grid the energy is assigned. Clustering begins once all generated energies are assigned to calorimeter cells. Groups of cells cluster according to the cone algorithm, see chapter 2, section 2.3.1.

Next, Atlfast starts to identify individual particles and applies realistic momentum resolutions. It begins with muons, continues with electrons and photons, and finishes with jets and taus. For generated final state leptons and photons the four-momenta are smeared according to a set of parameterizations; photon and electron energies use the same smearing, while a separate smearing is applied for muons. Atlfast parameterizations are given in detail in [44]. Each particle is then required to satisfy basic acceptance criteria: $|\eta| < 2.5$ and $p_T > 5$ GeV (6 GeV for muons). Isolation cuts are applied and are basically a requirement of lepton and photon cluster to have a certain distance in ΔR to other clusters. It is also required that the energy of clusters in the area around the isolated leptons and photons can not exceed 10 GeV. Clusters identified as isolated electrons or photons are then removed from the list of clusters.

The remaining clusters constitute the starting point of jet identification. All clusters are smeared according to a Gaussian energy resolution [44]. Then non-isolated muons will be taken as parts of jets and their energy will be added to the smeared cluster energy. If the resulting clusters are within acceptance ($|\eta| < 5.0$) and their transverse momenta exceed 15 GeV they are labelled reconstructed jets.

Missing transverse energy is calculated by summing the transverse momenta of all clusters associated to leptons, photons and jets as well as unused clusters, for instance clusters that do not pass the acceptance cuts. Cells that do not belong to any cluster are also added to the sum.

[3] All particles except from muons, neutrinos and stable weakly interacting SUSY particles

The total transverse energy in a hadron collider is expected to be zero,

$$\sum E_T = 0. \tag{3.1}$$

When particles escape detection this is no longer the case,

$$\sum E_T = \sum E_T^{vis}, \tag{3.2}$$

where $\sum E_T^{vis}$ is the transverse energy of the visible particles. The total missing transverse energy of all clusters and cells is then defined as

$$\sum E_T^{miss} = -\sum E_T^{vis}, \tag{3.3}$$

and is the value returned by Atlfast [44].

3.2.2 Atlsim

A full detector simulation of ATLAS is possible through the Atlsim program. Atlsim is a GEANT[4] [25] based program that simulates all the different sub detectors in ATLAS and their response to Monte Carlo generated particles. As opposed to Atlfast, Atlsim is comparable to the real detector in every detail.

GEANT makes it possible to design a detector by composition of geometrical objects, to which certain properties are assigned, material properties for instance [25]. When particles are transported through different detector regions, realistic effects like geometrical volume boundaries as well as interactions with matter and magnetic fields are accounted for. The particle trajectories and response of the sensitive detectors are recorded. The output from Atlsim is a zebra-file containing the raw detector simulation output. The output has to be digitized, and then reconstructed in order to translate signals into physical measurables like angles and energies.

Figure (3.3) and (3.4) illustrate the differences between fast and full detector simulation. In figure (3.3) the Atlfast combined calorimeter layer is illustrated. No inner detector or muon system is present and the tracks are obtained from the Monte Carlo generator. Figure (3.4) shows a completely different picture, the central part in grey, yellow and red shows the Pixel, SCT ant TRT subdetectors. The light and dark blue layers show the electromagnetic and hadronic calorimeters respectively. The elaborated muon system is placed outside the calorimeters. From the two figures the difference between the two simulation programs becomes clear. Atlsim simulates every detector in detail and gives a realistic picture of how the detector responds, while Atlfast is a calorimeter grid, useful for physics studies but not as a tool for understanding the detector.

3.3 The Athena Framework [31]

The Athena framework consists of a small program that by itself does not contain any functionality. Functionalities are compiled into shared libraries in the release and can be loaded on demand by the Athena main-program [26]. This means that event generation and fast detector simulation can be performed by running Athena only.

JobOption-files are the input of the Athena framework. Up to version 8.2.0 they were ordinary text files written in a programming language somewhat similar to c++. Recent Athena releases use python scripts instead of text files [28]. In jobOptions files the preferred event generator, the physics process, and the number of events wanted

[4]GEANT3(Fortran) was used up to ATLAS software release 6.0.3, after that GEANT4(c++) is used

for simulation are specified. By giving the correct specifications, Athena will call the desired event generator, PYTHIA for instance, and then send the generated events through the Atlfast detector simulation program. The output will be a file containing information on each simulated collision and the detector response, an ntuple. This file will be readable by standard data analysis programs like ROOT [29] and PAW [30].

Fast simulation procedures are fully contained within Athena while full simulation is not[5]. In order to produce an ntuple from full simulation, a complete full simulation chain must be preformed. Event-Generation is the first step in this chain. It is included in the Athena framework and preformed by using a jobOptions file made for this purpose. Atlsim is a standalone executable that runs outside the Athena framework. Atlsim takes the output from the event generation, usually a root-file, and transports the Monte Carlo generated events through the detector simulation. A zebra-file containing the raw detector simulation output is produced and used as input for the reconstruction. The reconstruction is also held within Athena and can be done by giving specification in a reconstruction jobOptions file [26].

3.4 Studies of detector efficiency

The detector efficiency will decide how many of the produced particles are actually measured by the detector. Studies of detector performance will tell us a lot about the quality of our discoveries and measurements at the LHC, and make it possible to improve calibration of the parts performing badly. In the search for supersymmetry it is especially important to study the reconstruction performance of relevant measurables. A brief study of detector efficiency will now be presented, while a more thorough study can be found in [2]. The studies presented in this section is partly a repetition of the work done by the ATLAS SUSY working group presented in [2], with some tentative improvements. The data set used is generated by the ATLAS SUSY working group for Data Challenge 1 (DC1). They produced a sample of all SUSY processes using Herwig(6.4) with the Isawig [19] interface, so that the mass spectra and decay rates were given by Isasusy (Isajet 7.64) [2]. The investigations in this section is not an attempt to study a particular process, but to see how ATLAS in general responds to measurables important to SUSY.

When detector efficiencies are studied we compare generated and reconstructed particles. In order to do this it is necessary to know how many and which particles were initially generated. Athena 6.0.3 provides a list of particles produced by the event generator and the detector simulation for each event. For leptons the following procedure was used: For each generated lepton a search is made among reconstructed leptons. In order to get a well defined match between the generated and reconstructed leptons the distance ΔR between them is calculated. ΔR is defined as

$$\Delta R = \sqrt{\Delta\eta^2 + \Delta\phi^2} \tag{3.4}$$

where $\Delta\eta = \eta_r - \eta_g$ and $\Delta\phi = \phi_r - \phi_g$, subscripts r and g indicate reconstructed and generated measurables respectively. The lepton candidate that has $\Delta R < 0.1$ is chosen and the generated lepton is considered reconstructed.

3.4.1 Electrons

Electrons are identified using requirements on E/p and shower shapes in the electromagnetic calorimeter[6]. Electromagnetic shower shape requirements are tuned for

[5] The new object oriented version of GEANT, GEANT4, is contained within Athena

[6] Cuts on shower shapes are contained in the variable *eg_isem* provided in CBNT_Athena ntuple (CBNT-ComBined NTuple). The variable returns zero if a cluster survives the cuts

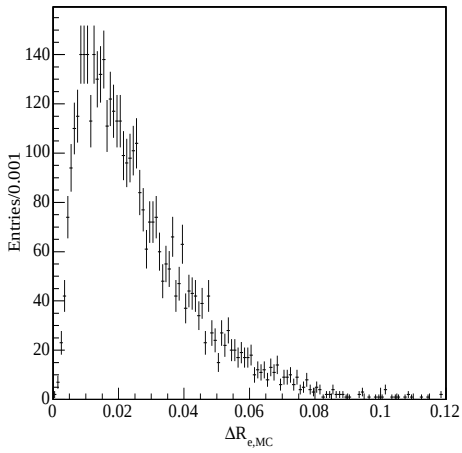

Figure 3.5: Distribution of the smallest distance ΔR between generated and reconstructed electrons.

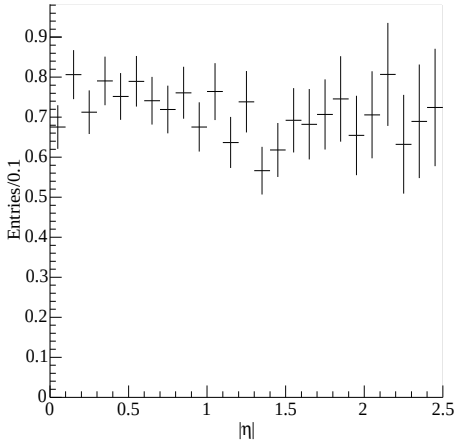

Figure 3.6: Electron reconstruction efficiency as a function of $|\eta|$

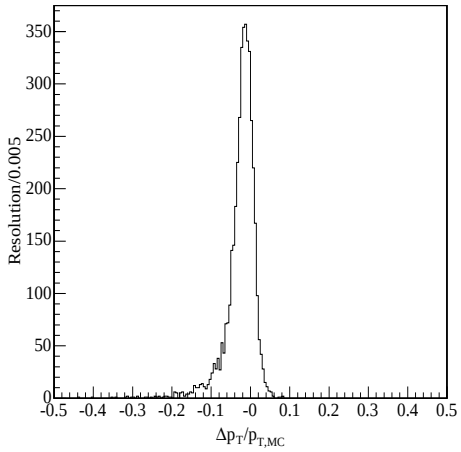

Figure 3.7: $\Delta E_T/E_{T,MC}$ for electrons with $\Delta R < 0.1$

electrons with $p_T = 25\,GeV$ and give a good jet rejection, while retaining high electron efficiency [2]. Clusters that pass the cuts on shower shape are in addition required to fulfill

$$\begin{array}{ll} 0.8 < E/p < 1.3, & |\eta| < 1.37 \\ 0.7 < E/p < 2.5, & |\eta| > 1.37. \end{array} \tag{3.5}$$

A narrower E/p range is required for smaller η, since the measurements in this part of the detector are more precise than for larger η. Only particles that pass these cuts are considered electron candidates and used further in the analysis. These cuts are the same as applied in [2].

Figure (3.5) shows the distance between each generated electron and the closest reconstructed match. Most pairs of generated and reconstructed electrons are within a distance of $\Delta R < 0.1$ of each other.

Figure (3.6) shows the reconstruction efficiency for electrons. It is obtained by dividing the histograms containing reconstructed pseudorapidity with the Monte Carlo

generated pseudorapidity. On average 71% of the generated electrons are reconstructed, which is close to 68.6% reported in [1], but below the result of approximatly 90% in [2]. The dissimilarity with regard to the latter could be due to the fact that isolation requirements are made for generated electrons in [2], no such requirements were made on the generated leptons in figure (3.6): Isolation cuts will reduce the number of generated particles and increase the efficiency. A drop in the efficiency at $1.3 < |\eta| < 1.5$ is expected due to the transition between the central and the endcap region of the calorimeter [2].

Figure (3.7) shows the distribution of $\Delta E_T / E_{T,MC}$, where $\Delta E_T = (E_T^{rec} - E_T^{MC})$. A shift towards negative values tells us that there is a tendency for the reconstructed E_T to be less than the generated. According to [2], the electromagnetic calorimeter is calibrated for photons rather than electrons in this version of Athena, which explains the negative tail.

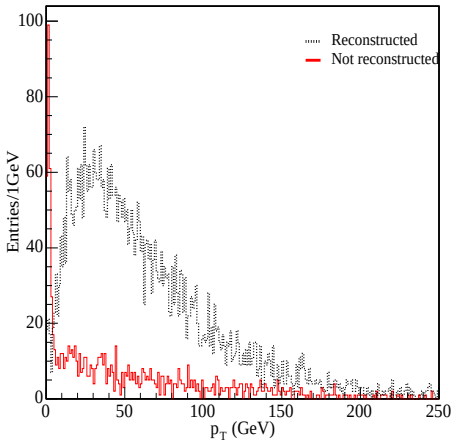

Figure 3.8: Generated transverse momentum of reconstructed electrons (dashed curve) and electrons that are not reconstructed (solid curve).

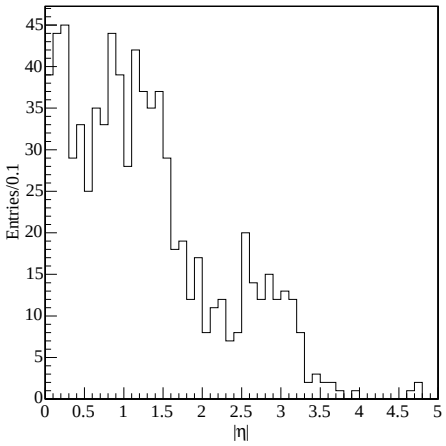

Figure 3.9: Generated pseudorapidity for electrons of $p_T > 10\,GeV$ that are not reconstructed.

It would be interesting to examine the properties of the remaining 18% of generated electrons that are not reconstructed. There are several reasons why ATLAS fails to identify or measure electrons. This includes electrons with low p_T, large η, those who disappear through inactive detector areas and electrons within jets.

Figure (3.8) shows the generated transverse momentum distribution for reconstructed (dashed curve) and non-reconstructed electrons (solid curve). There is an excess of events in the solid curve at very low transverse momentum values. Electrons generated with p_T of a few GeVs are very unlikely to be reconstructed. They are rejected either at the trigger level, which requires a minimum p_T, or at identification level.

Figure (3.9) shows the pseudorapidity distribution of non reconstructed electrons with $p_T > 10\,GeV$. The transverse momentum requirement is applied in order to avoid the low p_T electrons already mentioned. A large fraction is in the barrel/endcap transition region at $1.3 < |\eta| < 1.5$, where according to figure (3.6) only 60% of the generated electrons are reconstructed. Some electrons are found at large $|\eta|$ where the calorimeter granularity is larger and the measurements inaccurate [1]. Also these

electrons will have a smaller probability for being reconstructed.

From these investigations we have found that 35% of the non-reconstructed electrons are accounted for through low p_T, large η or inactive detector.

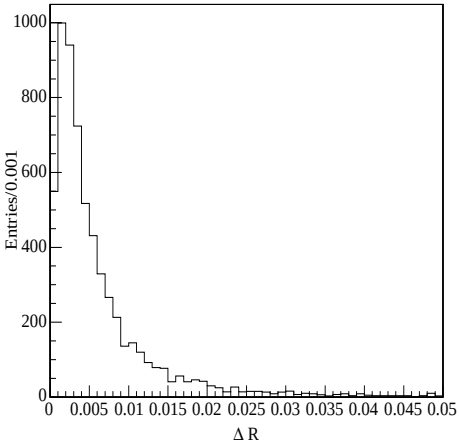

Figure 3.10: Distribution of distance ΔR between muons reconstructed with MuonBox and the closest Monte Carlo muon

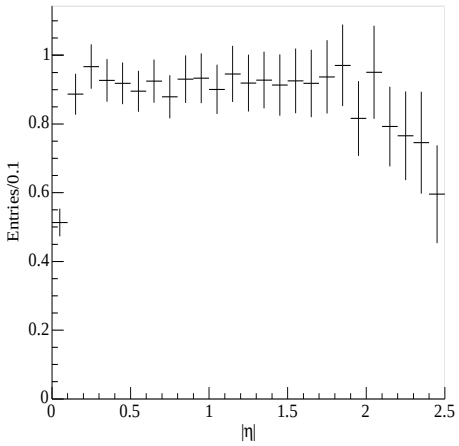

Figure 3.11: Muon reconstruction efficiency as a function of $|\eta|$

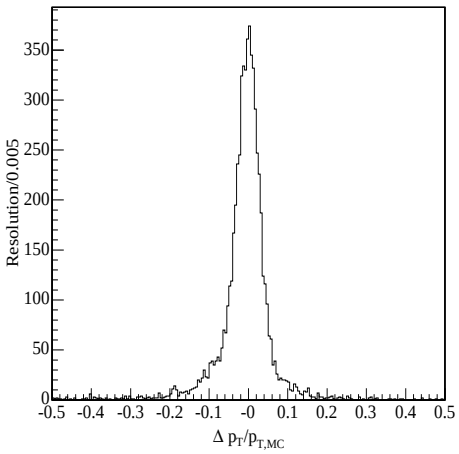

Figure 3.12: Muon momentum resolution, for muons with a good Monte Carlo match ($\Delta R < 0.1$).

3.4.2 Muons

Athena contains two muon reconstruction packages, MuonBox and Moore/Muid [12]. Due to the brief nature of this study, only variables made available through MuonBox are used in the investigations that follow. Reconstructed muons are simply identified by the number of tracks measured by the muon system[7].

[7]The variable Mb_ntrk in the CBNT_Athena ntuple

In order to see how 'good' our reconstructed muons really are, the distance ΔR (eq. 3.4) is calculated between each generated and reconstructed muon. As for electrons, the reconstructed muon that gives the smallest value of ΔR is selected. The ΔR-distribution is shown in figure (3.10). For most pairs of generated and reconstructed muons ΔR is below 0.05. A comparison between figures (3.10) and (3.5) show that ΔR for muons is in general less than it is for electrons. Because of bremsstrahlung the electron path is expected to deviate from the direction initially set (in ϕ and η). The muon path is nearly unaffected by outer disturbances, and the initial direction will only to a small extent diverge from the final measurement. This effect is most likely the cause of the difference between the electron and muon ΔR-distributions in figures (3.5) and (3.10) respectively.

Figure (3.11) shows the muon efficiency as a function of η. The plot is obtained in the same way as for electrons. On average the reconstruction efficiency is 86%, and larger than the electron efficiency. The ATLAS TDR [1] finds a muon efficiency of about 95%, but changes in the reconstruction software make comparison difficult. The ATLAS SUSY working group [2] finds a muon efficiency at roughly 90%. However, the exact procedure of obtaining the efficiency is not described, making it difficult to find the cause of this difference. The efficiency drops at $\eta = 0$ due to the exit for cables in the muon system. The decrease in efficiency for pseudorapidities in the range 2.1–2.5 is not understood, but was also observed in [2]. It could be an effect of low statistics, as the large error bars indicate.

Figure (3.12) shows the normalized difference between reconstructed and generated transverse momentum, $\Delta p_T / p_{T,MC}$ for reconstructed muons with $\Delta R < 0.1$ only. As seen in the figure the distribution peaks at zero with a slight shift toward negative values. As for electrons the reconstructed transverse momenta are smaller than the generated and indicates a small momentum loss for muons. A comparison with the electron case (figure 3.7) indicates a better electron resolution. The electron momentum is in this case reconstructed using the electromagnetic calorimeter only, which is calibrated to compensate for radiation loss such as bremsstrahlung. The muon momentum, however, is measured by the tracking detectors both in the muon system and in the inner detector. These do not account for the small radiation losses the muon suffers.

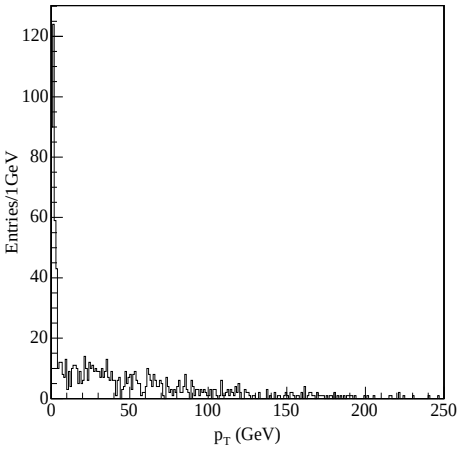

Figure 3.13: Transverse momentum of generated muons that are not reconstructed

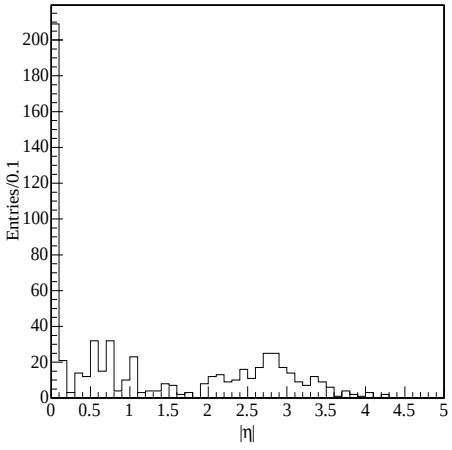

Figure 3.14: Pseudorapidity distribution for non reconstructed muons with p_T >10 GeV

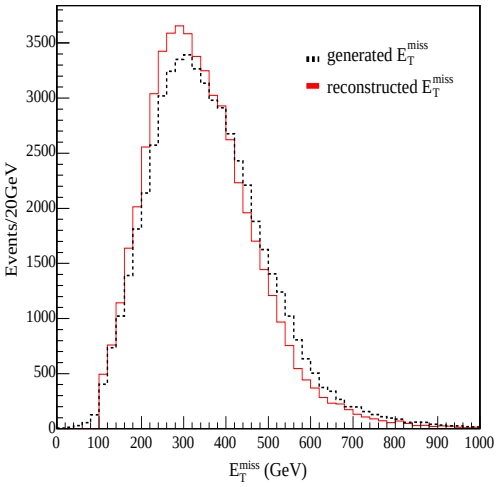

Figure 3.15: E_T^{miss} distribution, reconstructed solid, generated dotted.

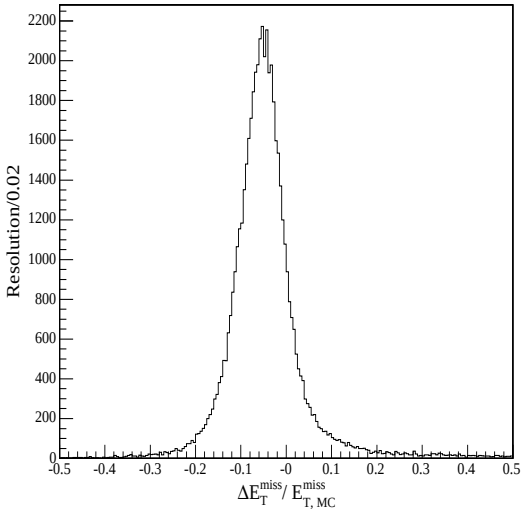

Figure 3.16: Normalized E_T^{miss}-distribution.

The reasons for muon reconstruction inefficiency are the same as for electrons. The transverse momentum of non-reconstructed muons shows, as for electrons, a spike at low p_T (fig. 3.13). Low muon transverse momentum is unlikely to be accepted by the trigger.

In figure (3.14) the pseudorapidity distribution for generated muons that fail reconstruction is shown. Again a transverse momentum requirement of 10GeV is applied in order to avoid the low-p_T range shown in figure (3.13). Figure (3.14) shows that a significant number of the muons are found at $\eta = 0$ where there are no detector. These muons will not be reconstructed. Low p_T, large η and inactive detector account for 35% of the lost muons.

3.4.3 Missing Energy

Missing transverse energy, E_T^{miss} was reconstructed using the Athena package MissingET [12] [8]. In figure (3.15) both the generated E_T^{miss} (dotted) and the reconstructed E_T^{miss} distributions are plotted. Generated missing transverse energy are slightly larger than the reconstructed, while the opposite is expected. Generated E_T^{miss} only accounts for the momenta carried away by weakly interacting neutral particles, such as neutrinos and LSPs. The reconstructed E_T^{miss}, however, will also include the momenta of those particles that by other means escape detection, and are therefore expected to be larger. Possible reasons for this shift in energies could be incorrect calibration or over-estimation at generator level.

The same tendency is shown in figure (3.16) where the normalized distribution of the reconstructed missing energy, defined as

$$\Delta E_T^{miss} = \frac{E_T^{miss,REC} - E_T^{miss,GEN}}{E_T^{miss,GEN}}, \tag{3.6}$$

is plotted. In an ideal world the value should be zero for every single event, but due to the difference between reconstructed and generated values of E_T^{miss} as already seen

[8] The package includes reconstructed variables of different calibrations and Monte Carlo truth information.

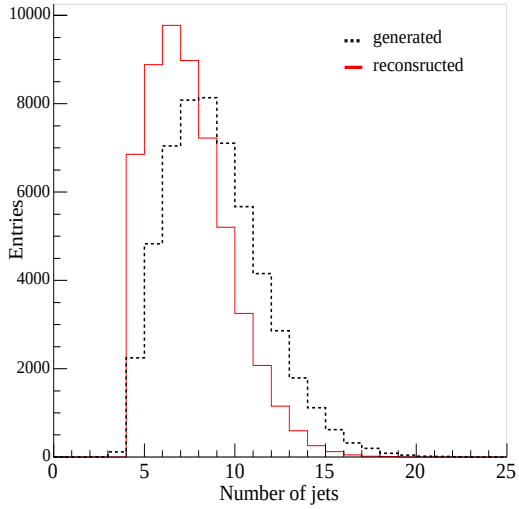

Figure 3.17: Multiplicity of jets.

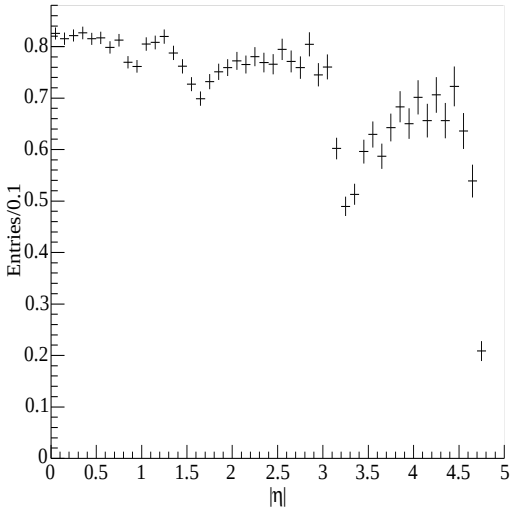

Figure 3.18: Jet reconstruction efficiency as a function of $|\eta|$.

in figure (3.15) the distribution peaks around -0.06. By fitting the distribution with a Gaussian we find an overall resolution of 5.3%.

3.4.4 Jets

The jets were reconstructed using the JetRec algorithm in Athena [12]. Jets are defined using both the cone algorithm and the K_T algorithm, see subsection 2.3.1, and information on both is available in the Athena ntuple. The jets studied in this section will be cone jets only, since this is the algorithm used by Atlfast.

Figure (3.17) shows the number of reconstructed jets plotted together with the number of generated jets. The jet algorithm used for reconstruction was applied to the particles produced by the event generator [2]. Overall the number of reconstructed jets is less than the number of generated jets. There are in fact 8.4 generated jets per event and 7.0 reconstructed jets. The cone algorithm defines all clusters within a cone of radius $R = 0.4$ as belonging to the same jet. One jet identified and measured by the hadronic calorimeter could in fact be two close jets originating from two distinct partons! This could of course explain the reduction in jet multiplicity between generation and reconstruction level. However, most jets will be lost through the beam pipe or inactive detector, as seen in the next paragraph.

In figure (3.18) the reconstruction efficiency as a function of $|\eta|$ is shown. The distribution is obtained in the same way as for electrons and muons. On average 76% of the generated jets were reconstructed. Significant loss of efficiency is observed in the $|\eta|$ regions 1.2-2.0 and 3.1-4.0. Transition between the hadronic barrel and endcap calorimeter causes the drop at $1.2 < |\eta| < 2.0$. The reconstruction efficiency is especially poor in the region around $|\eta| = 3.2$, due to the transition between the hadronic endcap calorimeter and the high density forward calorimeter.

3.4.5 Jet/lepton separation

Electrons and jets are not always separated in Athena release 6.0.3, some electrons are identified as both jet and electron. Figure (3.19) shows the distance ΔR between a reconstructed electron and the closest jet. For most electrons this distance is below

0.04, which is very short, and indicates that each electron is contained within a jet. Figure (3.20) shows the normalized difference between transverse momenta for these electrons and jets, the distribution peaks at -0.2.

One interpretation of these results is that a fraction of the reconstructed electrons are also registered as jets by Athena, so that the jet and electron are in fact the same. The negative shift in Δp_T (fig. 3.20) is then most likely due to different calibrations of the electromagnetic and hadronic calorimeters. In order to avoid ambiguities, the electron disguised as a jet has to be removed from the list of jets.

If the hypothesis in the above paragraph is correct, the ΔR-distribution in figure (3.19) does not show the real electron/jet separation. In order for the separation to be representative, electrons identified as jets must be excluded. When this is done a new ΔR-distribution is obtained. Figure (3.21) shows this distribution, which reveals a good electron/jet separation. This is expected because the requirements on electromagnetic shower shapes, used in electron identification, impose a powerful isolation cut [2].

Muons are identified by the inner detector and the muon system, and no ambiguities between muons and jets are observed. Figure (3.22) shows the distance between reconstructed muons and the closest jet. Approximately 6% of the reconstructed muons have a distance smaller than 0.1 to the closest jet and are probably a part of it. The figure shows that it is necessary to isolate the muons before they can be used in further calculations. This can for instance be done by requiring $\Delta R > 0.2$.

3.4.6 Conclusion

The brief investigations of this section have shown the ability of the ATLAS detector to measure electrons, muons, jets and missing transverse energy. The studies are not detailed enough to draw a definite conclusion, but they can be used as an indication for efficiency and resolution estimation.

The overall, average, lepton efficiency is 79% when no isolation cuts or transverse momentum requirements are applied. Lepton momentum is reconstructed to an accuracy of a few % compared to the generated momentum; 2.3% for electrons and 3.4% for muons. Jets are reconstructed with an overall efficiency of 76% and missing transverse energy reconstructed to an accuracy of 5%. With the unsophisticated methods of this section in mind these numbers are actually good, and suggest that ATLAS will perform well on all measurements related to SUSY searches.

One way to improve the numbers given in the last paragraph would of course be to isolate the leptons and impose momentum requirements on them. This would in fact have been a more realistic approach with respect to SUSY processes. Especially a p_T-requirement would have been appropriate, since leptons from supersymmetric decays are expected to have large transverse momentum. It would have been interesting to see the effect of such a requirement on lepton efficiency and momentum resolution. The same argument can be applied to jets, since jets from sparticle decays are expected to be very energetic. By imposing p_T-requirements on the jets we would expect to remove those coming from underlying events, and thereby change the reconstruction efficiency. Efficiency studies of a particular decay chain could also have been interesting.

Finally it needs to be mentioned that the tools used in these studies have impact on the results. Improvements of the software tools for ATLAS is an ongoing process and new versions are released all the time. Newer releases of the detector simulation and reconstruction programs would yield more realistic results.

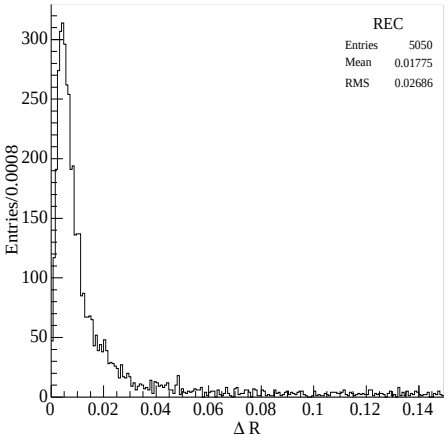

Figure 3.19: Distance ΔR from reconstructed electrons to the closest jet

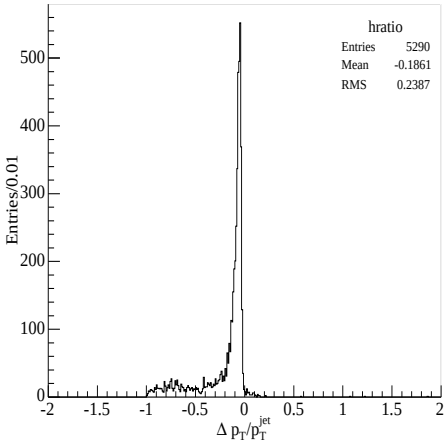

Figure 3.20: $p_{T,e}/p_{T,jet}$ for reconstructed electron and the nearest jet

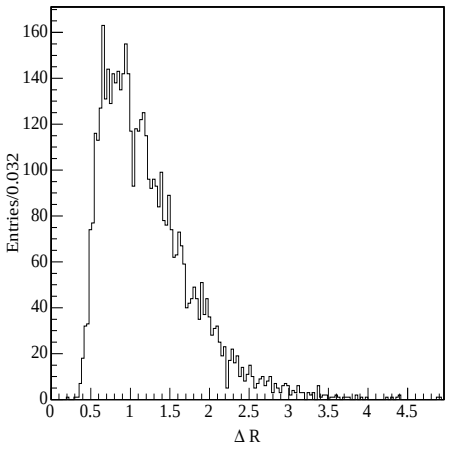

Figure 3.21: Distance ΔR between reconstructed electron and the closest jet, when the electron/jet ambiguity is removed.

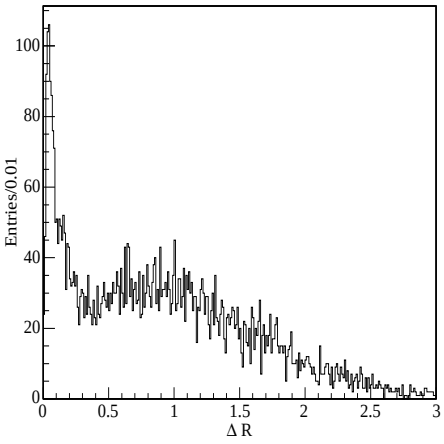

Figure 3.22: Distance ΔR from nearest jet for reconstructed muons

Chapter 4

Signal and Background studies

When it comes to supersymmetry two things are important; discovery and measurements. If supersymmetry exists, discovery is considered relatively easy due to clear signatures. A greater challenge is to measure particle properties, especially mass. Every supersymmetric process will have two neutral and weakly interacting LSPs that escape the detector, making it impossible to measure masses from peaks in invariant mass distributions. Different techniques have been developed in order to measure masses, but knowledge of a well defined decay chain is required.

The goal of this chapter is to illustrate the techniques and challenges of picking out one decay mode of a supersymmetric quark in a MSSM, mSUGRA model. We begin with a brief investigation of the SUSY discovery potential. Then we start looking at the artificial situation of a pure signal data sample, in order to study the features of the decay chain. Different backgrounds will be studied in order to see how they differ from the signal. Comparison of signal and background will constrain the value of some measurables in order to reduce the background, hopefully without removing too much of the signal.

All data samples used in this study are generated by Pythia using Atlfast as detector simulation, through the Athena 8.0.5 interface. Full simulation with a reduced data sample will be presented later. The reader should note that Athena release 8.0.5 calculates masses, energies and momenta in MeV. As a result all energy-related distributions in this chapter have units of MeV along the x-axis. It should also be noted that lepton identification efficiencies are not parameterized in Atlfast, this efficiency is 90% per lepton [6].

4.1 Inclusive measurements

QCD- annihilation and scattering processes, see figure (4.1), will dominate the LHC collisions. As a result, huge amounts of jets will penetrate the detector and deposit energy in the tracking systems and calorimeters. With a cross section of $\sigma_{QCD} \sim 10^7 pb$, these processes have the largest production rate at the LHC. Interesting events like supersymmetric processes will be rare compared to these (see tab. 4.2) and occur in the noise of everything else. For that reason it is important to know how SUSY processes are different from the dominating LHC processes.

One important difference between Standard Model and supersymmetry events is the large amount of missing transverse energy in the latter. As described in chapter 1, conservation of R-parity will lead to the production of two LSPs[1] that escape the detector in every SUSY event. Since sparticles in general are heavy, only collisions

[1] *L*igthest *S*upersymmetric *P*article

Sparticle	Mass (GeV)
$\tilde{g}$	736.9
$\tilde{u}_L$	649.6
$\tilde{u}_R$	625.6
$\tilde{d}_L$	653.6
$\tilde{s}_L$	653.6
$\tilde{c}_L$	649.6
$\tilde{t}_1$	418.1
$\tilde{e}_R$	159.1
$\tilde{\mu}_R$	159.1
$\tilde{\chi}_1^0$	120.6
$\tilde{\chi}_2^0$	231.7
$\tilde{\chi}_1^\pm$	231.2

Table 4.1: Selected sparticle masses calculated by Pythia 6.221

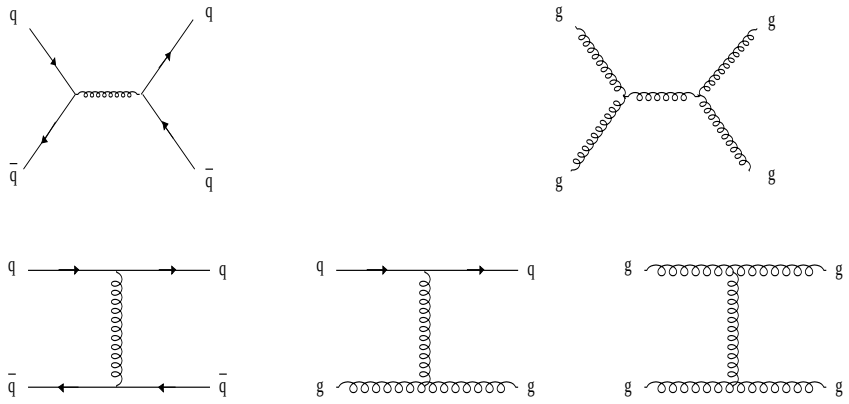

Figure 4.1: Low order QCD annihilation and scattering processes

with large momentum transfer will be able to produce them. This means that both the rest mass and the kinetic energy of the LSP will be larger than for Standard Model invisibles. That is why we expect the E_T^{miss} in SUSY events to exceed Standard Model values as figure (4.2) shows. The dashed curve in the figure shows the missing transverse energy distribution for all SUSY events in a given MSSM scenario[2] and the black curve shows the same distribution for QCD events. As we have seen the QCD cross section is enormous at the LHC and the QCD black curve has been scaled up 200 000 times in order to resemble a luminosity of[3] $30fb^{-1}$. For this reason the statistical uncertainties are large, as seen in the bin around 200 GeV (200000 MeV). Figure (4.2) confirms that SUSY events have a considerably larger missing transverse energy than Standard Model events. SUSY missing transverse energy exceed the QCD scattering at 200 GeV, and completely dominates at larger values.

If supersymmetry is discovered, a determination of the SUSY mass scale is needed. A common variable used for this purpose is the effective mass, M_{eff} defined as [5]:

$$M_{eff} = E_T^{miss} + p_{T,1} + p_{T,2} + p_{T,3} + p_{T,4}, \tag{4.1}$$

where $p_{T,i}$ is the transverse momentum of the four most energetic jets in the event. This

[2]The DC1 point, see next section
[3]Comparable to three years of running at low luminosity

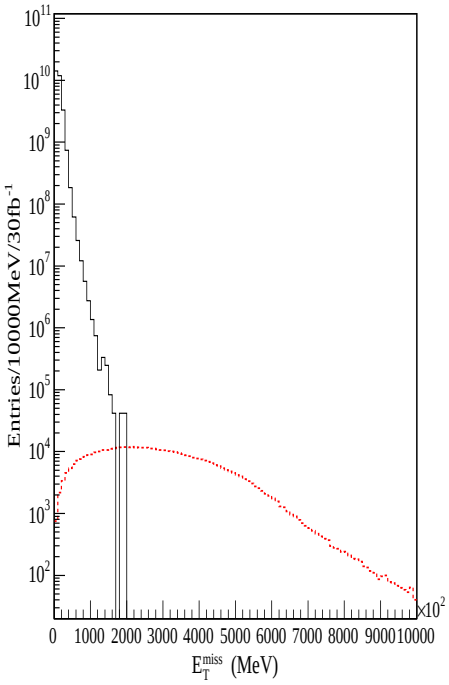

Figure 4.2: Missing transverse energy for all SUSY events, dashed curve, and QCD events, black curve

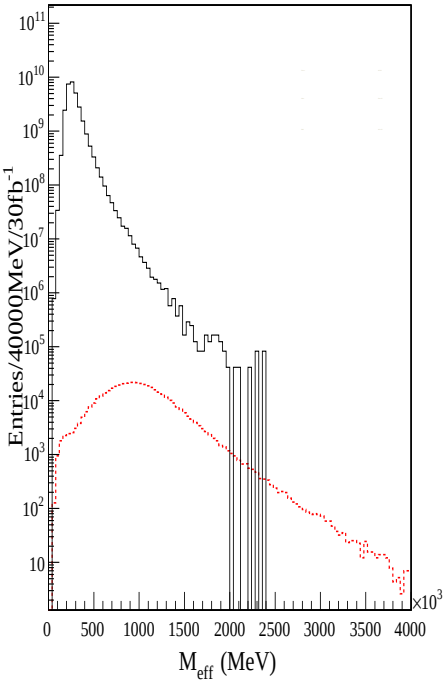

Figure 4.3: Effective mass for all SUSY events, dashed curve, and QCD events, black curve

variable is sensitive to the decay of squarks and gluinos, both of which always involve high energy jets. The peak of the M_{eff} distribution provides a good first estimate of the SUSY mass scale, defined as [5]:

$$M_{SUSY} = min(M_{\tilde{g}}, M_{\tilde{u}_R}), \tag{4.2}$$

meaning that the SUSY mass scale will give information on the squark masses.

Figure (4.3) shows the effective mass distribution for SUSY events (dashed curve) and Standard Model events (solid curve). It is the peak of the dashed curve that determines the SUSY mass scale. In figure (4.3) the peak is completely covered by the Standard Model distribution, but we expect requirements on jet transverse momentum and E_T^{miss} to improve the signal to background ratio. The distribution has a peak around 800 GeV, while from table (4.1) we see that the $\tilde{u}_R$ mass, which is the smallest of the the two masses in equation (4.2), is 625 GeV. Other methods are needed for precise measurements of the SUSY mass scale, but the M_{eff} distribution works fine as a first estimate.

In this section we have seen that the missing transverse energy distribution is a powerful tool in order to distinguish SUSY events from the common QCD events at the LHC. In addition, we have shown how to estimate the SUSY mass scale. At this point SUSY measurements and discovery seem easy but some remarks need to be made.

First we need to remember that there will be other processes at the LHC with larger missing transverse energy than expected in QCD. One such process is leptonic $t\bar{t}$ decay (see fig. 4.11) that will be studied in section 4.3. Even though figure (4.2) is a little bit too optimistic, studies later in this chapter will show that the SUSY transverse missing energy distribution also clearly exceeds the corresponding Standard Model distribution in processes where large E_T^{miss} is expected.

Secondly, in this section we have been studying supersymmetry events in general. No attempt has been made to describe the properties of a certain decay channel. A decay channel would be identified by measurables other than missing transverse energy. In many SUSY decays leptons and high energy jets are common. By requiring events to contain one or more leptons, or the jets to have large transverse momenta, we would discover that very few of the QCD scattering events could fulfill the requirements. By constraining our investigations, SUSY discovery could be even clearer.

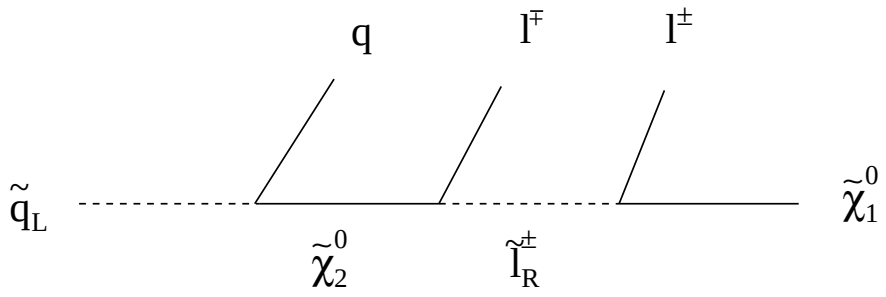

Figure 4.4: Cascade decay of $\tilde{q}_L$. The dotted line represent integer spin particles while the solid lines are fermionic particles

4.2 Signal

As already mentioned in chapter 1, all sparticle masses and mixings are determined by five input parameters in the mSUGRA model. These constitute points in the five dimensional mSUGRA space, and were defined in chapter 1, subsection 1.2.4. The parameter values in (4.3) below are referred to as the DC1-point[4] and will be used throughout the study:

$$m_0 = 100, \qquad m_{1/2} = 300, \qquad A_0 = -300, \qquad \tan\beta = 6.0, \qquad sign\,\mu = + \quad (4.3)$$

At this point in parameter space the following squark decay is allowed [1]:

$$\tilde{q}_L \rightarrow \tilde{\chi}_2^0 q \rightarrow \tilde{l}_R^{\pm} l^{\mp} q \rightarrow \tilde{\chi}_1^0 l^+ l^- q \quad (4.4)$$

The decay chain in equation (4.4), illustrated in figure (4.4), will be referred to as the signal, the signal chain or cascade decay. The signature of this process is two isolated, opposite charge, same flavour, leptons on one hand, and one jet and large missing transverse energy on the other hand. Squark production mechanisms are listed in table (4.2).

Table (4.1) shows that $\tilde{u}_L$, $\tilde{d}_L$, $\tilde{s}_L$ and $\tilde{c}_L$ are heavy particles of nearly the same mass. For that reason they are commonly referred to as $\tilde{q}_L$.

[4]The ATLAS SUSY working group chose this point for full simulation in ATLAS Data Challenge 1

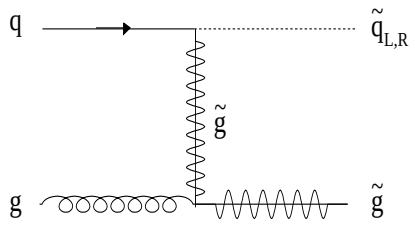

Figure 4.5: Low order squark and gluino production

Production	Pythia Process	Cross section (pb)
$q_j + g \rightarrow \tilde{q}_{j,R} + \tilde{g}$	259	4.0
$q_j + g \rightarrow \tilde{q}_{j,L} + \tilde{g}$	258	3.7
$g + g \rightarrow \tilde{g} + \tilde{g}$	244	1.2
$q_i + q_j \rightarrow \tilde{q}_{i,R} + \tilde{q}_{j,R}$	272	1.1
$q_i + q_j \rightarrow \tilde{q}_{i,L} + \tilde{q}_{j,L}$	271	0.96
$q_i + q_j \rightarrow \tilde{q}_{i,L} + \tilde{q}_{j,R}$	273	0.86
$q_i + \bar{q}_j \rightarrow \tilde{q}_{i,L} + \tilde{\bar{q}}_{j,L}$	274	0.17
$q_i + \bar{q}_j \rightarrow \tilde{q}_{i,R} + \tilde{\bar{q}}_{j,R}$	275	0.19
$q_j + g \rightarrow \tilde{q}_{j,L} + \tilde{\chi}_1^0$	246	0.008

Table 4.2: Production mechanism of high cross section SUSY processes obtained from Pythia 6.221

The decay chain in figure (4.4), starts with a squark decaying into a neutralino ($\tilde{\chi}_2^0$) and a jet. The mass difference between $\tilde{q}_L$ and $\tilde{\chi}_2^0$ is about 400 GeV as seen in table (4.1), increasing the probability of the jet from this decay to have high energy. Next $\tilde{\chi}_2^0$ decays into a right handed slepton ($\tilde{l}_R$) and a lepton. At last $\tilde{l}_R$ decays into a lepton and the lightest neutralino ($\tilde{\chi}_1^0$) also referred to as the LSP. We expect the lepton from the neutralino decay to have larger momentum than the lepton coming from the slepton decay. This is due to the mass difference between the supersymmetric mother and her daughters.

Table (4.3) shows the decay modes and branching ratios of left-handed squarks. The chargino ($\tilde{\chi}_1^{\pm}$) decay mode is the most probable. Approximately 30% of the squarks decay into a neutralino($\tilde{\chi}_2^0$), which is necessary to start the chain in figure (4.4). $\tilde{\chi}_2^0$ has several decay modes as well, stop plus top production is the most common, as seen from table (4.4). Only one in five neutralinos will decay into a right-handed slepton and a lepton. Right-handed sleptons however have one decay mode only, they will always decay into an LSP and a lepton, $\tilde{l}_R^{\pm} \rightarrow l^{\pm}\tilde{\chi}_1^0$.

Because of the many decay modes of both the squark and neutralino, squark production will give many different signatures. This makes it hard to generate the cascade decay only. For a pure signal study the following process was generated

$$q_j + g \rightarrow \tilde{q}_{j,L} + \tilde{\chi}_1^0, \tag{4.5}$$

see table (4.2). This process is attractive since only one left-handed squark, and a LSP, is produced. The LSP is stable and will not decay, while the squark will decay through the modes given in table (4.3). Since Athena 8.0.5 provides Monte Carlo truth information, the cascade decay can be identified and signal events selected.

Decay	BR (%)
$\tilde{q}_L \rightarrow \tilde{\chi}_1^{\pm} + q$	63.9
$\tilde{q}_L \rightarrow \tilde{\chi}_2^0 + q$	32.1
$\tilde{q}_L \rightarrow \tilde{\chi}_1^0 + q$	2.1
$\tilde{q}_L \rightarrow \tilde{\chi}_2^{\pm} + q$	1.4

Table 4.3: Branching ratios for squark decay

Decay	BR (%)
$\tilde{\chi}_2^0 \rightarrow \tilde{t}_1^{\pm} + t^{\mp}$	67.4
$\tilde{\chi}_2^0 \rightarrow \tilde{l}_R^{\pm} + l^{\mp}$	23.2
$\tilde{\chi}_2^0 \rightarrow \tilde{\chi}_1^0 + Z_0$	4.9
$\tilde{\chi}_2^0 \rightarrow \tilde{\nu}_{l_L} + \bar{\nu}_l$	2.2

Table 4.4: Branching ratios for $\tilde{\chi}_2^0$ decay

The motivation for using process (4.5) is to simplify the event topology. When we have only one decaying squark the features of the signal chain will become more apparent and combinatorial effects from other decaying particles will be significantly reduced. The process in equation (4.5) will be used in this section only. In sections 4.4 and 4.5 all processes in table (4.2) will be used for left-handed squark production. It is also important to remember that the 'signal' in this thesis is not a particular production mechanism, like the one in equation (4.5), but rather the decay of a squark through the chain in figure (4.4).

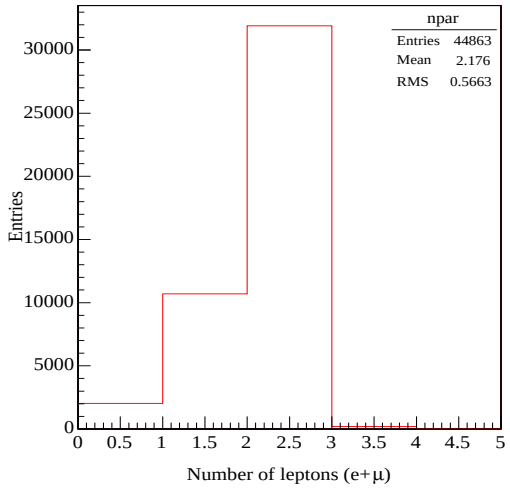

Figure 4.6: Number of leptons in the process $q_j + g \rightarrow \tilde{q}_{j,L} + \tilde{\chi}_1^0$ followed by decay chain (4.4)

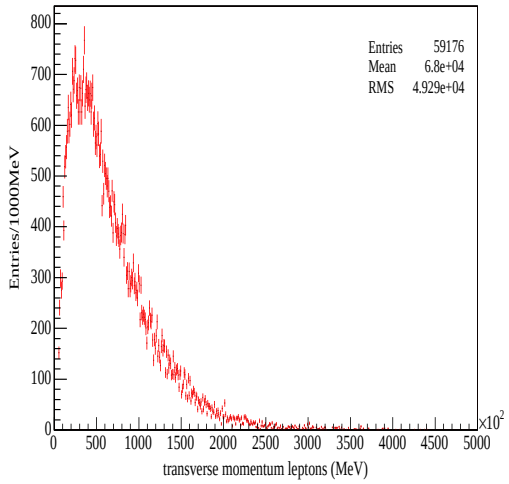

Figure 4.7: p_T distribution for 2-lepton events from figure (4.6)

In order to get a high statistics signal sample, 600 000 events were generated. This number does not correspond to any realistic production rate of process (4.5) within the years of running at the LHC. It is however, justified by the purpose of this section; to study the features of a pure signal sample without combinatorial or statistical effects.

From the branching ratios of table (4.3) and (4.4) we expect that about 44 000 of the generated events will decay through the chain in figure (4.4). Events that contained generated $\tilde{q}_L$, $\tilde{\chi}_2^0$ and $\tilde{l}_R$ were selected. The presence of all three particles uniquely identify the signal chain, due to the simple composition of process (4.5). Two same-flavour leptons of opposite charge are expected as well as large missing transverse energy, due to the two LSPs, and a hard jet.

The number of leptons in the selected signal events is plotted in figure (4.6). We

expect two leptons but due to Atlfast inefficiencies, events with one and zero leptons are also present. The efficiency tells how well a detector performs in measuring particles and is often calculated by dividing the number of reconstructed particles by the number of generated particles (see section 3.4). The probabilities for finding two, one and zero leptons as a function of efficiency are given in equations (4.6)-(4.8). This efficiency is a measure of the effect of isolation cuts and geometrical acceptance in Atlfast:

$$P_0 = (1-\epsilon)^2 = \frac{N_0}{N_{tot}} \tag{4.6}$$

$$P_1 = 2(1-\epsilon)\epsilon = \frac{N_1}{N_{tot}} \tag{4.7}$$

$$P_2 = \epsilon^2 = \frac{N_2}{N_{tot}}, \tag{4.8}$$

where P_i is the probability of finding i leptons, ϵ is the lepton efficiency, N_i the number of events with i leptons, and N_{tot} the total number of signal events.

From figure (4.6) we find $N_2 = 31914$ and $N_{tot} = 44858$, this gives $\epsilon = 0.84$. The calculated efficiency can be used to check whether it accounts for all events having less than two leptons, see table (4.5). We see that the Atlfast efficiency rate accounts for most events with one lepton and half of the events with zero leptons. It is however interesting to note that the sum of N_1 and N_0 is almost the same for both calculated and simulated values. Only events where both leptons are identified by Atlfast will be used further in the analysis.

	N_1	N_0
Calculated values	12058	1148
Simulated values	10692	2030

Table 4.5: Values calculated from efficiency compared to simulated values

As already mentioned, we expect the leptons to be relatively energetic. The lepton p_T distribution in reconstructed two-lepton events are shown in figure (4.7). Most leptons have a transverse momentum larger than 20 GeV.

One of the two leptons should be considerably more energetic than the other. The most energetic lepton should come from the $\tilde{\chi}_2^0$-decay, and its transverse momentum should be twice as large as the p_T of the lepton coming from $\tilde{l}_R$ decays[5]. In figure (4.8) the momentum ratio between the softest and the hardest lepton is plotted, and the mean value is actually close to 0.5 as we expect from kinematics. This ratio is expected to be very sensitive to the slepton mass, since a slepton close in mass to either $\tilde{\chi}_2^0$ or $\tilde{\chi}_1^0$ will produce a soft lepton [1]. In reality it will be hard to draw a definite conclusion from a plot like figure (4.8) since a clean signal sample will be nearly impossible to obtain. The soft and hard leptons could namely originate from particles other than $\tilde{\chi}_2^0$ and $\tilde{l}_R$, or be produced by sparticles in the other branch. This misidentification of the mother of the leptons has consequences when we try to reconstruct sparticle masses from the end points of invariant mass distributions.

Only one jet will be produced in the decay chain, while figure (4.9) shows 4.8 jets per event. These jets come from underlying events like multiple soft-to-hard parton interactions, initial/final state radiation, fragmentation and beam remnants [4]. Just one of the roughly five jets come from the decay of $\tilde{q}_L$ into $\tilde{\chi}_2^0$. This jet will in general differ from jets produced in underlying events by a significantly larger p_T.

[5]Two-body decay $M \to m_1 + m_2$: From energy and momentum conservation in the rest frame of the decaying sparticle of mass M, the momentum of the massless lepton p_1 is given as: $p_1 = \frac{M^2 - m_2^2}{2M}$.

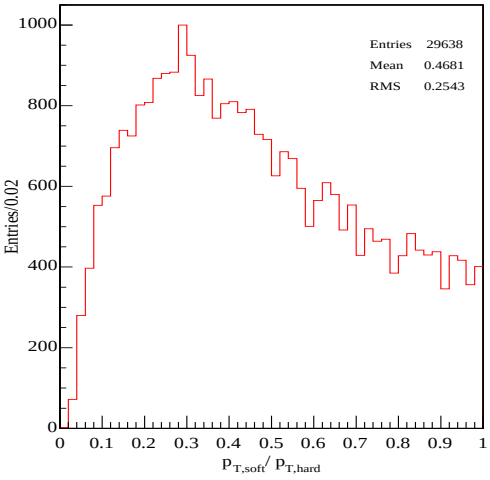

Figure 4.8: Ratio between low and high p_T for signal leptons

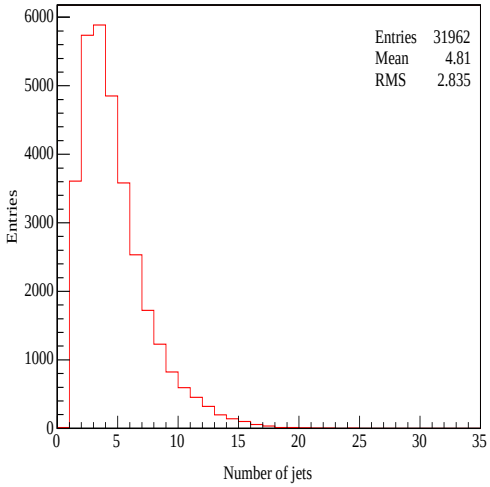

Figure 4.9: Number of jets in events with two leptons

Figure (4.10) shows the distribution of jet multiplicity in three different p_T ranges. The left plot shows the number of jets that have $p_T < 50\,GeV$, the central plot shows the distribution of jets in the range $50\,GeV \leq p_T < 100\,GeV$, while the right plot shows the jet multiplicity for $p_T \geq 100\,GeV$. Note that most jets are either in the low or high p_T-range, jets with intermediate transverse momentum are few compared to the other two ranges. It is also worth noticing that by increasing the transverse momentum, the jet multiplicity is reduced.

Most events have only one jet with p_T above 100 GeV. This is expected to originate from squark decay. The existence of events with both two and three high p_T jets causes difficulties in picking the right one, a problem that will be addressed later.

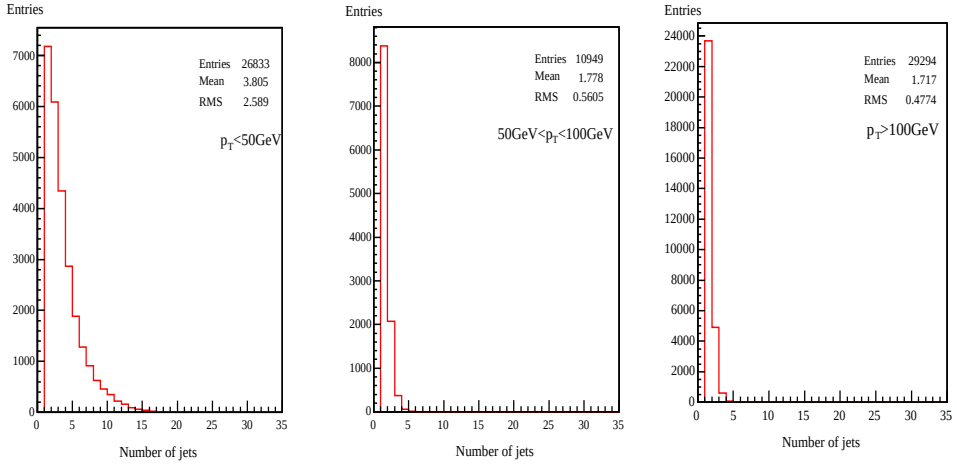

Figure 4.10: Number jets in three p_T ranges. Left $p_T < 50\,GeV$, central $50\,GeV \leq p_T < 100\,GeV$ and right $p_T \geq 100\,GeV$

Decay			BR (%)
$\tilde{g}$	$\rightarrow$	$\tilde{q}_L + \bar{q}$	11
$\tilde{g}$	$\rightarrow$	$\tilde{q}_L + q$	11
$\tilde{g}$	$\rightarrow$	$\tilde{q}_R + \bar{q}$	17
$\tilde{g}$	$\rightarrow$	$\tilde{q}_R + q$	17
$\tilde{g}$	$\rightarrow$	$\tilde{b}_1 + \bar{b}$	7.6
$\tilde{g}$	$\rightarrow$	$\tilde{b}_1 + b$	7.6
$\tilde{g}$	$\rightarrow$	$\tilde{b}_2 + \bar{b}$	4.6
$\tilde{g}$	$\rightarrow$	$\tilde{b}_2 + b$	4.6
$\tilde{g}$	$\rightarrow$	$\tilde{t}_1 + \bar{t}$	9.4
$\tilde{g}$	$\rightarrow$	$\tilde{t}_1 + t$	9.4

Table 4.6: Gluino decay with branching ratios from Pythia 6.221

Decay			BR (%)
$\tilde{b}_2$	$\rightarrow$	$\tilde{\chi}_1^0 + b$	56.6
$\tilde{b}_2$	$\rightarrow$	$\tilde{t}_1 + W^-$	28.5
$\tilde{b}_2$	$\rightarrow$	$\tilde{\chi}_1^- + t$	6.7
$\tilde{b}_2$	$\rightarrow$	$\tilde{\chi}_2^0 + b$	4.8

Table 4.7: Branching ratios of $\tilde{b}_2$ decays

4.3 Background

The signal signature is not unique. There are both Standard Model and SUSY processes that could give two leptons, high energy jets and large missing transverse energy. Processes with the same signature as the signal are usually referred to as background. A major task in many particle physics searches is to separate signal and background, supersymmetry is no exception.

4.3.1 Supersymmetric background

SUSY processes with large cross sections are listed in table (4.2), gluino and squark production dominates. Gluinos are assumed to be heavier than squarks at the DC1-point [1] and decay into them. This is also seen from table (4.6) where the dominating gluino branching ratios are listed. Background from SUSY processes will therefore mainly come from decaying squarks and gluinos. An investigation of the decay modes of these particles will follow in order to see which SUSY processes are capable of mimicking the signal.

Squarks most commonly decay through the process

$$\tilde{q}_{i,L} \quad \rightarrow \quad \tilde{\chi}_1^{\pm} + q_j, \qquad (64\%) \tag{4.9}$$

where the indices indicate that up-type squarks like $\tilde{u}_L$ and $\tilde{c}_L$ decay to down-type quarks in the same supermultiplet like d and s respectively. Similarly the down-type squarks decay to up-type quarks in the same supermultiplet. It is also important to note that the chargino $\tilde{\chi}_1^{\pm}$ has the same mass (see tab. 4.1) as the neutralino $\tilde{\chi}_2^0$ and the decays will be kinematically indistinguishable.

Decay			BR (%)
$\tilde{b}_1$	$\rightarrow$	$\tilde{t}_1 + W^-$	42.8
$\tilde{b}_1$	$\rightarrow$	$\tilde{\chi}_1^- + t$	32.1
$\tilde{b}_1$	$\rightarrow$	$\tilde{\chi}_2^0 + b$	23.0

Table 4.8: Branching ratios of $\tilde{b}_1$ decays

Decay			BR (%)
$\tilde{t}_1$	$\rightarrow$	$\tilde{\chi}_1^+ + b$	66.3
$\tilde{t}_1$	$\rightarrow$	$\tilde{\chi}_1^0 + t$	27.2
$\tilde{t}_1$	$\rightarrow$	$\tilde{\chi}_2^0 + t$	6.5

Table 4.9: Branching ratios of $\tilde{t}_1$ decays

The main decays of $\tilde{\chi}_1^\pm$ are through the processes[6]

$$\begin{array}{lcll} \tilde{\chi}_1^\pm & \rightarrow & \tilde{\chi}_1^0 + W^\pm & (49\%) \\ \tilde{\chi}_1^\pm & \rightarrow & \tilde{\tau}_1^\pm + \nu_\tau. & (49\%) \end{array} \tag{4.10}$$

The decay products of $\tilde{\chi}_1^\pm$ above have the following dominating decays

$$\begin{array}{lcll} W^\pm & \rightarrow & \bar{q}_i + q_j & (64\%) \\ W^\pm & \rightarrow & l^\pm + \nu_l(\bar{\nu}_l) & (20\%) \end{array} \tag{4.11}$$

$$\tilde{\tau}_1^\pm \rightarrow \tilde{\chi}_1^0 + \tau^\pm. \qquad (100\%) \tag{4.12}$$

While the most common decays[7] of τ are

$$\begin{array}{lcll} \tau^\pm & \rightarrow & \nu_\tau(\bar{\nu}_\tau) + \text{hadrons} & (64\%) \\ \tau^\pm & \rightarrow & l^\pm + \nu_l(\bar{\nu}_l) + \bar{\nu_\tau}(\nu_\tau). & (35\%) \end{array} \tag{4.13}$$

From the decay modes described above we see that leptons can be produced in many ways. A few examples will be given for clarity.

$$\begin{array}{ccccccc} \tilde{q}_L & & & + & & \tilde{q}_L & \\ \downarrow & & & & & \downarrow & \\ \tilde{\chi}_1^+ & + & q_j & & & \tilde{\chi}_1^- & + & q_j \\ \downarrow & & & & & \downarrow & & \\ \tilde{\tau}_1^+ & + & \nu_\tau & & & W^- & + & \tilde{\chi}_1^0 \\ \downarrow & & & & & \downarrow & & \\ \tau^+ & + & \tilde{\chi}_1^0 & & & l^- & + & \bar{\nu_l} \\ \downarrow & & & & & & & \\ l^+ & + & \nu_l & + & \bar{\nu}_\tau & & & \end{array} \tag{4.14}$$

Signal imitations can also occur from gluino decays, table (4.6):

$$\begin{array}{ccccccc} & & & \tilde{g} & & & \\ & & & \downarrow & & & \\ & & & \tilde{b}_1 & + & \bar{b} & \\ & & & \downarrow & & & \\ & & & \tilde{t}_1 & + & W^- & \\ & & & \downarrow & & \downarrow & \\ b & + & \tilde{\chi}_1^+ & & & l^- & +\bar{\nu}_l \\ & & \downarrow & & & & \\ \tilde{\chi}_1^0 & + & W^+ & & & & \\ & & \downarrow & & & & \\ \nu_l & + & l^+ & & & & \end{array} \tag{4.15}$$

[6] All branching ratios are obtained from Pythia 6.221
[7] Branching ratios obtained from [3] p.333

Both examples will lead to detectable l^+, l^- and jet (q_j), as well as large missing energy, due to neutrinos and LSPs. In supersymmetry the actual decay chain is of importance since long decay chains are used for sparticle mass measurements.

This section has shown that there are many SUSY processes that have the signal signature, and that there are no clear distinguishing features of either SUSY signal or background. This means that we will most probably make mistakes and pick the wrong processes when we are looking for cascade decays (see fig. 4.4). At this point however it is important to observe that the two leptons in the signal chain have the same flavour due to conservation laws, while leptons from W-bosons and τ-leptons do not. A pair of leptons coming from two Ws or two taus are uncorrelated with respect to flavour, if one W decays into a muon the other might decay into an electron.

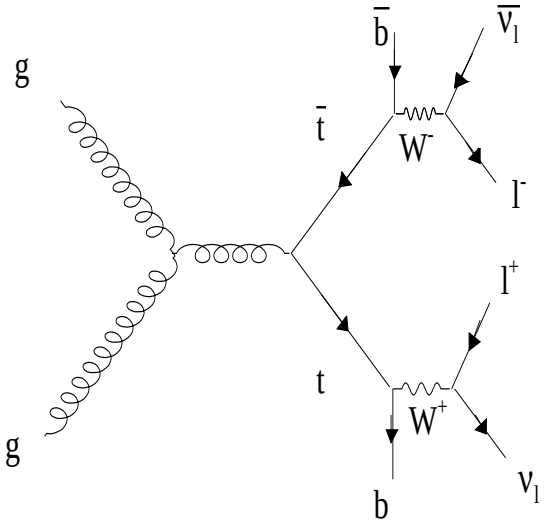

Figure 4.11: Decay of a top-quark to jet and leptons

4.3.2 $t\bar{t}$-background

Because of the large cross section of $t\bar{t}$ at the LHC, $780pb^{-1}$, it is the most dominant Standard Model background. The most significant decay mode for the t-quark is

$$t \rightarrow W^+ + b \qquad (99.8\%) \tag{4.16}$$

W-bosons decay predominantly to either 'light' quarks or leptons, as already seen in section 4.3.1, equation (4.11). Figure (4.11) illustrates how $t\bar{t}$ can resemble the SUSY signal with W-bosons decaying into leptons.

A few remarks should be made on this background process. Firstly, the leptons are uncorrelated just as they were for SUSY background processes. A detailed description of a technique that removes such leptons will be given in subsection 4.6. Secondly, the masses involved are also much smaller than in the signal process (figure 4.4). The mass of the t-quark is 175 GeV while the squark masses are around 650 GeV! Production of $t\bar{t}$ can occur at center of mass energies approximately four times lower than the energy required for squark production! Leptons and jets from low-energy top-production are expected to have less energy than leptons and jets originating from squarks. For high energy $t\bar{t}$ production, however, the energies of leptons, jets and missing energy could easily be comparable to signal energies.

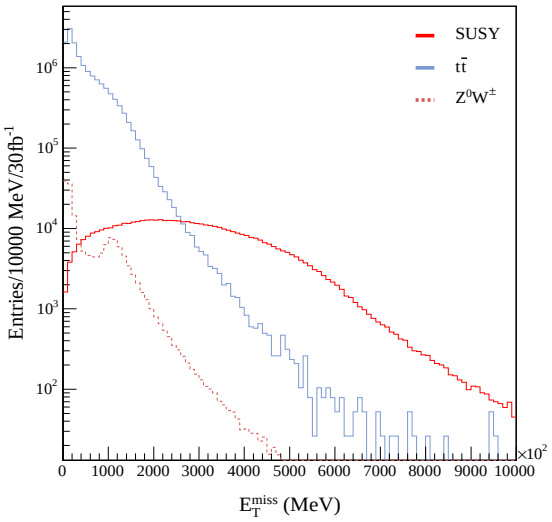

Figure 4.12: Missing transverse energy distributions for $t\bar{t}$ events (light) curve, SUSY events (dark) curve and $Z^0W^{\pm}$ dashed curve. No cuts are applied.

There are other processes that could resemble the signal as well, one is production of W/Z^0 together with jets. Figure (4.12) shows the missing transverse energy distributions for SUSY, $t\bar{t}$ and W/Z^0 processes, without any cuts applied. It shows that $t\bar{t}$ dominates W/Z^0 completely. $t\bar{t}$ constitutes in fact 95% of the total Standard Model background [6]. That is why $t\bar{t}$ is the only Standard Model background process that will be studied in this thesis. As we will see later the Standard Model background can be removed by very hard cuts, and our greatest concern will be background from other competing SUSY processes.

4.4 Signal and background comparison

The situation presented in section 4.2 is highly artificial. At the LHC we will have no such thing as Monte Carlo truth information available. If supersymmetry exists it will be produced with all other processes and the signature from SUSY processes will be mixed with Standard Model events, and possibly other new processes.

Comparing selected measurables for signal and background will increase our ability to understand how to distinguish them. Six hundred thousand events for each of the backgrounds were produced using Pythia through the Athena 8.0.5 interface. General supersymmetry was generated using Pythia command *pysubs msel 39* and $t\bar{t}$ events with *pysubs msel 6*. All data samples are scaled to an integrated luminosity of $30fb^{-1}$ corresponding to three years of running at low luminosity at the LHC. A minimum p_T-cut of 100 GeV was set at the generator level for the Standard Model processes in order to ensure high energy collisions, since soft $t\bar{t}$ events do not really imitate the signal. Most plots in the following section use log-scale on the y-axis in order to compare distributions of very different magnitude. Pure signal events (see fig. 4.4) are included for comparison. These originate from all squark production processes and not solely the one in equation (4.5) of section 4.2.

Leptons are easily measured, this makes them attractive for signal and background comparison. If the properties of leptons are significantly different in signal and background, we have found a way to distinguish the two. As mentioned in section 4.2, we

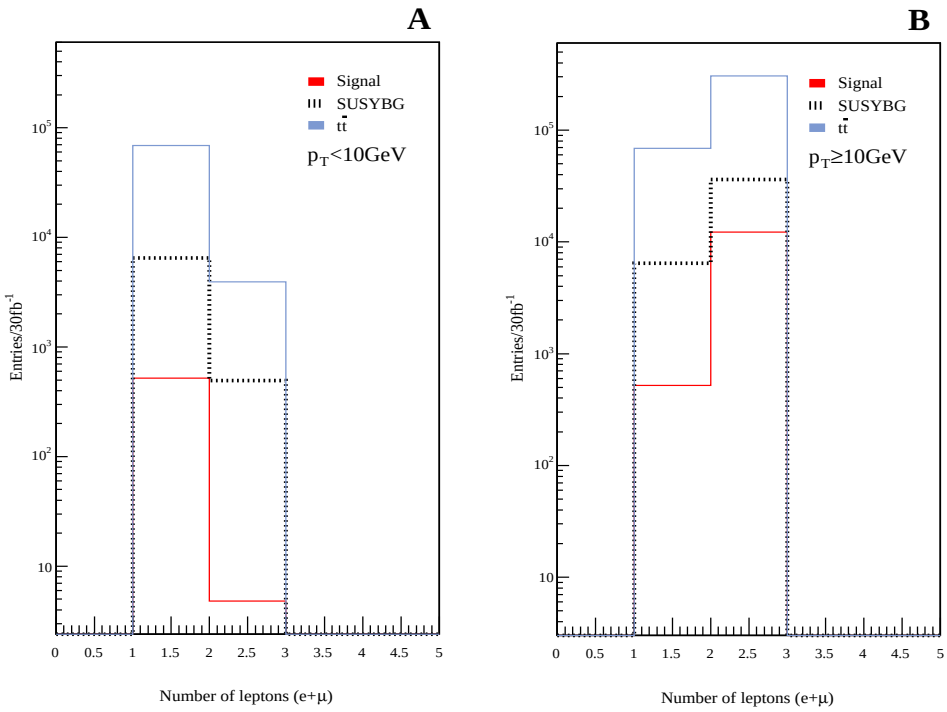

Figure 4.13: A: Number of leptons with $p_T < 10\,GeV$. B: Number of leptons with $p_T \geq 10\,GeV$

	Signal	general SUSY	$t\bar{t}$
$e^{\pm}$	0.93	0.19	0.23
$\mu^{\pm}$	0.87	0.19	0.16
$l^{\pm}$	1.83	0.38	0.39

Table 4.10: Average number of leptons in signal and background events. No cuts applied.

expect both leptons to be relatively energetic since they originate from heavy particle decays. In SUSY background processes, W-bosons and taus are the main sources of leptons. In $t\bar{t}$ decay only W-bosons contribute to the lepton multiplicity.

The most striking feature of the signal is the two final state leptons. Table (4.10) shows the average number of leptons in signal and background events. The signal has on average four times more electrons and muons than each of the backgrounds. In what follows, only events with two leptons will be used for signal and background comparison.

Figure (4.13) shows the lepton multiplicity distribution for the signal and the two background processes in two different p_T-ranges. Plot A shows the number of leptons with p_T below 10 GeV, while plot B shows the number of leptons with p_T above 10 GeV.

Separating leptons into two transverse momentum ranges has a huge impact on the lepton distribution for signal events. In the low p_T-range of figure (4.13)A the fraction of dileptonic signal events is negligible. There are however a large number of events with one lepton below 10 GeV and the other above. This feature is most striking for $t\bar{t}$-events where 23% of the events have leptons asymmetrically distributed around the

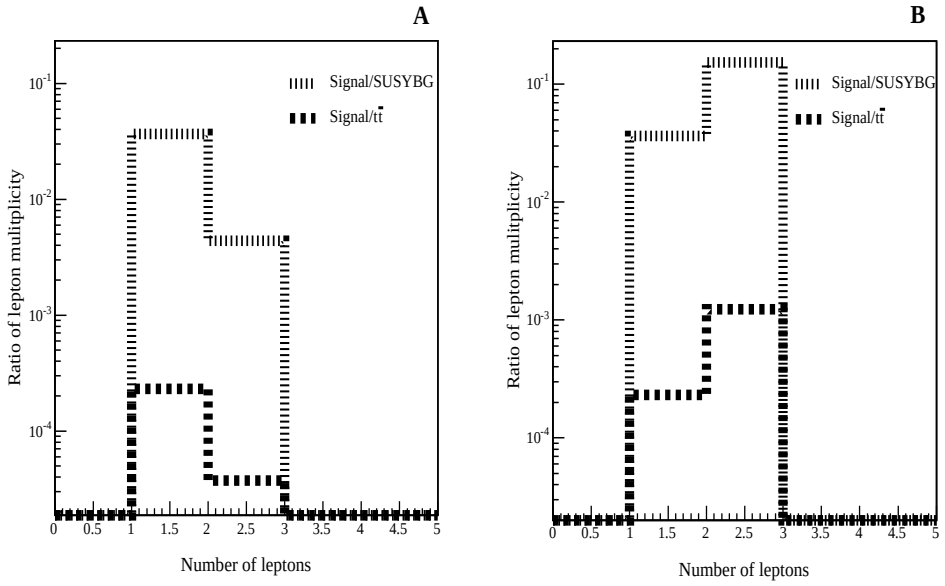

Figure 4.14: Ratio between signal and background lepton multiplicity for leptons with p_T below 10 GeV (A).p_T above 10 GeV (B).

10 GeV limit, while the corresponding numbers for SUSY background and signal are 13% and 5% respectively. Although the 2-lepton fraction in SUSY events improved significantly, figure (4.13)B is still dominated by $t\bar{t}$ due to the large cross-section. It is especially interesting that the fraction of two leptons in signal events rises from nearly none in figure (4.13)A to the same order of magnitude as SUSY background events.

In order to study the relative change of multiplicity in figures (4.13)A and B the signal to background ratio for the two p_T-ranges are plotted in figure (4.14). The darker of the two histograms shows the ratio of lepton multiplicity in signal events to lepton multiplicity in $t\bar{t}$-events while the lighter histogram shows the same ratio for signal and SUSY background events. A large number would of course give an indication of a huge signal, but since no direct cuts are applied to the data sample, the signal is still small compared to background and the ratio is below one. As before, plot A shows the ratio for soft leptons while plot B illustrates the case for harder leptons.

Figure (4.14)A shows that below 10 GeV both backgrounds dominate the signal especially in events with two soft leptons. In this p_T-range dileptonic $t\bar{t}$ events are five orders of magnitude larger than the signal while the SUSY backgrounds are three orders of magnitude larger. Requiring $p_T > 10\,GeV$ has a huge impact on the signal/background ratio for the two background processes. The effect is especially apparent in events with two hard leptons, as figure (4.14)B shows. When imposing $p_T > 10\,GeV$ both ratios increase by nearly a factor 100.

So far we have seen that most signal events have two leptons with $p_T > 10\,GeV$. There are signal events that have one soft and one hard lepton, but the number is low compared to both general SUSY and $t\bar{t}$ processes. A requirement of two leptons with transverse momentum above 10 GeV will not remove too much signal and will improve the signal to background ratio by two orders of magnitude. Above the 10 GeV threshold dileptonic signal and general SUSY background are comparable in magnitude.

It is important to note that no cuts on lepton flavour or charge are made yet. Section 4.5 will show that such requirements reduce the background further.

Another signal feature is one high energy jet coming from squark decay. Other supersymmetric processes will also have this feature. Most SUSY events contain squarks,

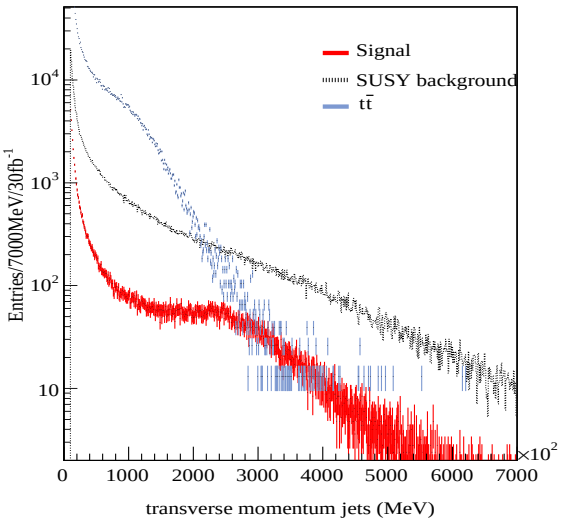

Figure 4.15: Jet-p_T distribution for signal and background

gluinos or a combination of them (see tab. 4.2). Squarks and gluinos usually decay into another SUSY particle and a jet, see tables (4.3) and (4.6). This jet is expected to have much higher energy than jets from $t\bar{t}$ events. That is why distributions of jet multiplicity as a function of transverse momentum could be of interest.

Figure (4.15) shows the transverse momentum distribution for jets in signal and background events. The plot shows that $t\bar{t}$ jets dominate the distribution at energies below 200 GeV. Above this value SUSY background processes take over. The plot indicates that requirements on transverse momentum for jets could help us reduce $t\bar{t}$ background to some extent.

Figure (4.16) shows the jet multiplicity for three ranges of p_T, in which the intervals are the same as in figure (4.10), section 4.2. The multiplicity of jets with transverse momentum below 50 GeV is plotted in figure (4.16)A, and the largest number of jets are found in this range for all processes. The average number of jets in this plot is 4.4 for SUSY signal and background and 5.0 for $t\bar{t}$. For SUSY processes most soft jets come from underlying events.

Figure (4.16)C shows the jet multiplicity for jets with transverse momentum larger than 100 GeV. At high transverse momenta the structure with two hard jets in SUSY events appear, both SUSY signal (solid curve) and background (dotted curve) have a peak at two jets. Three and four hard jets are also common in these events, probably originating from squark-gluino or gluino-gluino production respectively[8]. The average number $t\bar{t}$ jets in this high p_T-range is 1.6 against 2.5 for SUSY signal and background.

Table (4.11) summarizes how the fraction of jets for each process are distributed over the p_T-ranges above; the numbers are given in percent. Note the similarity between signal and SUSY-background events. The resemblance between the two is of no surprise since events where a squark decays through the signal chain (fig. 4.4) usually contains another decaying squark or gluino. As already mentioned, decay of squarks and gluinos always produce a jet, such that SUSY events in general have at least two hard jets. There is no reason why the hadronic activity in signal decays should be different from these, see tables (4.3) and (4.6). This point is also clear from the p_T-distributions in

[8]Three jets obtained through $\tilde{q}+\tilde{g} \rightarrow q\tilde{q}_L qX \rightarrow XXqq$ where X usually is a chargino or a neutralino (see table 4.3 and 4.6).

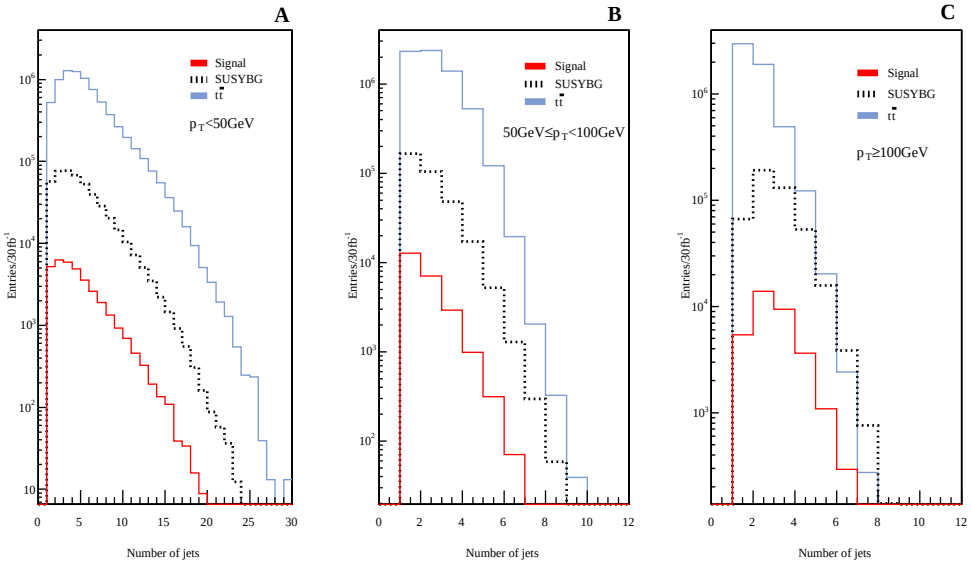

Figure 4.16: Distribution of jet multiplicity in tree different p_T ranges for signal and background. A:$p_T < 50\,GeV$. B:$50\,GeV \leq p_T < 100\,GeV$. C: $p_T \geq 100\,GeV$.

	Signal	SUSY background	$t\bar{t}$
$p_T < 50\,GeV$	54	54	63
$50\,GeV \leq p_T < 100\,GeV$	15	16	23
$p_T \geq 100\,GeV$	31	30	14

Table 4.11: Fractions of jet multiplicity in tree different p_T-ranges given in %.

figure (4.15) and (4.16). Table (4.11) and figure (4.16) show that jets from $t\bar{t}$ events are distributed differently, with more jets in the lower p_T ranges than in SUSY events. Only 14% of all $t\bar{t}$-jets have transverse momentum larger than 100 GeV, twice less than the SUSY case.

Jet investigations have shown that signal and SUSY background have the same jet topology, while $t\bar{t}$ jets are generally found in the low-p_T range. By imposing a minimum requirement on jet transverse momentum we are likely to exclude a significant amount of the $t\bar{t}$ events. Section 4.5 will study this in more detail.

Finally, comparison between signal and background transverse missing energy distributions is examined (fig. 4.17). SUSY signal and background are indistinguishable, and $t\bar{t}$ dominates at lower values of E_T^{miss}, but is suppressed by SUSY background events at larger values.

The main conclusion of this section is that $t\bar{t}$ events differ from signal events in both lepton and jet multiplicities, and the respective transverse momentum distributions. SUSY background, however, is more difficult to separate from the signal because of their common features. The choice of two regions of lepton transverse momentum, unveiled a significant difference in how the leptons were distributed as a function of p_T. These investigations should be kept in mind when we in the next section use a set of criteria that is believed to distinguish the signal chain from background.

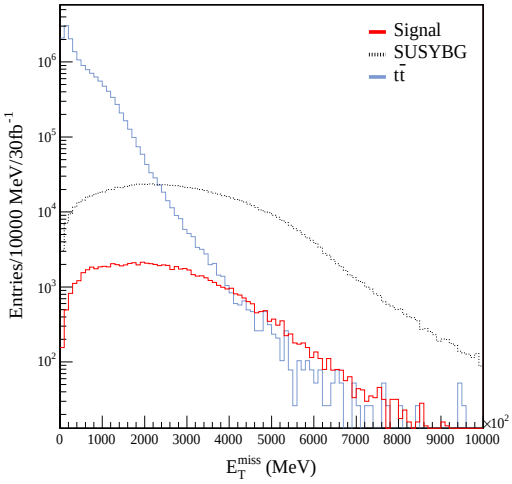

Figure 4.17: Missing transverse energy distribution

4.5 Effects of cuts

In this section no pure signal sample will be used. The general supersymmetry data sample used in the last section, contains both signal and background. If supersymmetry exists, all processes will be mixed together. We then have to be able to pick out the right decay chain in the mixture of both Standard Model and SUSY. We begin with a mixture of SUSY and $t\bar{t}$ samples from which we try to extract the signal decay chain.

The ATLAS Technical design report [1] present a number of requirements or cuts, that reduces Standard Model background and selects events containing the signal chain. A modified version of these is[9]:

1. two isolated opposite-sign leptons with $p_T > 10\,GeV$ and $|\eta| < 2.5$
2. at least four jets with $p_{T,1} > 100\,GeV$ and $p_{T,2,3,4} > 50\,GeV$
3. $E_T^{miss} > 100\,GeV$
4. $M_{eff} > 400\,GeV$

The effective mass M_{eff} is defined in equation (4.1) of section 4.1 and the pseudorapidity η is defined in chapter 3 section 3.4. In this section the effects of the above-mentioned cuts will be studied in detail. Their purpose is to extract the signal chain from a mixed sample of events and it is important to know how well they perform, together and individually. References will also be drawn to section 4.4 to better understand their motivation.

We begin with requirement (1) and reject all events that do not contain two same flavour, opposite charged, leptons. Only events with one e^+e^- or $\mu^+\mu^-$ pair are kept. In our sample of general SUSY and $t\bar{t}$, this very powerful cut rejects at least 95% of events from both processes (see tab. 4.12). Ideally none of these are signal, but due to Atlfast (see sec. 4.2) and ATLAS (chap. 3, sec. 3.4) inefficiencies, not every produced lepton is detected, causing a small fraction of the signal to be rejected as well. Two opposite sign, same flavour, leptons are the strongest identifiers of the signal chain. Without detecting both leptons, the signal cannot be recognized.

[9]The only difference is that the ATLAS TDR [1] requires $E_T^{miss} > \max(100\,GeV, 0.2M_{eff})$

An event can of course only be considered as a signal candidate when all stable decay products are detected, a minimum being two leptons and one jet. Events in a hadron collider always have many jets, while leptons are rare. That is why, throughout this section, cuts will be made on a data set that contains at least two same flavour, opposite sign, leptons.

There will also be SUSY events with production of two squarks that both decay through the signal chain, these however amount to only 0.6% of the events and will not be taken into account.

		S+B	SUSY	$t\bar{t}$
1.	No Cut	8 243 698	529 412	7 714 286
2.	$l_i^{\pm} + l_j^{\pm}$	415 139	43 246	371 893
3.	$l^+ + l^-$	198 020	28 555	169 466
4.	p_T leptons $\geq$ 10 GeV	169 117	25 399	143 717
5.	Number of jets $\geq$4	132 723	23 875	108 849
6.	$M_{eff} > 400\,GeV$	103 985	27 755	76 230
7.	$E_T^{miss} > 100\,GeV$	70 458	23 453	47 006
8.	Nb. jets $\geq$4, $p_{T1} > 100\,GeV$, $p_{T2,3,4} > 50\,GeV$	15 786	11 564	4 221

Table 4.12: Number of events passing cuts. The events below the double line are picked from a pre-selection that fulfills two same flavour opposite sign leptons

Table (4.12) shows the effect of cuts (1-4) separately, rows (4-8) list results that are independent of each other. All numbers are scaled to a luminosity of $30 fb^{-1}$ corresponding to three years of running at low luminosity at the LHC [1]. The first row in the table shows the number of events that are produced for each process at the given luminosity. It is followed by a row that shows the reduction of events by requiring two leptons regardless of flavour and charge, while the third row shows the effect of requiring two same flavour, opposite sign, leptons. Nearly 98% of the total number of events are rejected by this requirement. The third row is followed by a double line, the cuts below this line are made on events that have two same flavour, opposite sign, leptons. As previously mentioned in this section, only events that fulfill this requirement can be considered signal candidates. Percentages quoted below will all be calculated with respect to the numbers on the third row of table (4.12). The numbers in this row in the table will be referred to as *candidate events*.

The next cut, number four in the table, is made on lepton transverse momenta; $p_T > 10\,GeV$. A dramatic effect of this cut is not expected since Atlfast has trigger cuts on lepton transverse momentum, a minimum of 5 GeV for electrons and 6 GeV for muons. Still 11% of SUSY events and 15% of $t\bar{t}$ events are rejected, which is within the scope of the investigations in section 4.4 (see fig. 4.13). As from section 4.4 we do not expect to reject more than 2% of signal events by this cut, SUSY events rejected here are certainly mostly background.

Next, the effect of requiring events to have at least four jets in addition to the two leptons is shown. The combination of jets and leptons reduces $t\bar{t}$ by 35%, while SUSY events are reduced by 16%. $t\bar{t}$ decays to leptons through W-bosons and only two b-jets are produced. A high jet multiplicity is therefore not expected in such processes.

A cut on M_{eff} is in fact a cut on both missing transverse energy and jet transverse momentum (eq. 4.1). It is expected to accept SUSY processes and reject Standard Model processes [1]. Table (4.12) shows that this is indeed the case, 3% of SUSY-events and 55% of $t\bar{t}$ events are rejected. Supersymmetric events are expected to have large missing transverse energy due to the escaping LSP, and hard jets coming from decay of

heavy particles. $t\bar{t}$ will have some missing transverse energy coming from neutrinos and could in fact have some high energy jets. From table (4.13) however, we see that the mean value of both E_T^{miss} and jet p_T are considerably smaller than the corresponding values in supersymmetry events.

The considerations from the paragraph above are reinforced by the next cut on missing transverse energy. Large E_T^{miss} is generally considered the most distinct feature of supersymmetry events. Still the demand on events to have a missing transverse energy of at least 100 GeV exclude approximately 18% of all SUSY events. The reward is easily seen from the fraction of $t\bar{t}$ refused by this cut: 72% of all candidate events are excluded.

The last cut considered in table (4.12) is actually a composite one: p_T requirements are put on the four hardest jets, mostly to reduce Standard Model background. This cut alone removes 98% of the $t\bar{t}$ background, at the same time it also removes 60% of all SUSY-events. Among the latter is roughly 80% of the total number of signal events! Even though a considerable amount of $t\bar{t}$ events is removed, some effort should be put into the tuning of this cut, since so many signal events are rejected.

4.5.1 Visualizing the cuts

The invariant mass distribution of the two final leptons is important, and its triangular shape characteristic, to the signal. In figures (4.19)-(4.24) some of the cuts in table (4.12) are applied to this distribution. The dark (red) curve is the sum of SUSY and $t\bar{t}$ events, while the light (blue) and dashed (black) curves are the pure $t\bar{t}$ and SUSY distributions respectively. The figures are to be read from left to right and figures in the same row have the same range on the y-axis. By applying the cuts in table (4.12) one by one, we can see which cuts have the largest impact on the mixed sample of SUSY and $t\bar{t}$ events. The requirement of four hard jets are by far the most important, as seen by comparing figure (4.26) and (4.24).

Some of the cuts described above have a huge impact on the data sample. It is appropriate to investigate some of them further and study their impact on other variables. The requirement of two same flavour, opposite sign, leptons, the jet multiplicity in combination with transverse momentum conditions and the missing transverse energy requirements will be considered in the subsections that follow.

		$\langle p_T \rangle$ leptons (GeV)	$\langle Number \rangle$ of jets	$\langle p_T \rangle$ jets (GeV)	$\langle E_T^{miss} \rangle$ (GeV)
S+B	No cut	54.0	7.8	54.1	66.7
	Cut	56.9	5.2	55.3	102.6
$t\bar{t}$	No cut	54.0	7.8	51.3	52.1
	Cut	54.2	5.0	45.8	79.2
SUSY	No cut	53.8	7.8	95.6	279.8
	Cut	66.4	6.7	96.8	241.9

Table 4.13: Mean values of selected variables for signal plus background (S+B), before and after requiring two same flavour opposite sign leptons.

4.5.2 Requirement 1: Two same flavour, opposite sign, leptons

Requiring two same flavour, opposite sign leptons will have impact on other interesting measurables. Table (4.13) gives an overview of the effect this cut has on certain selected measurables. These are lepton transverse momentum, jet multiplicity, jet transverse momentum and missing transverse energy. The table shows the mean values of all these measurables for the sum of SUSY and $t\bar{t}$ events, referred to as S+B in the table, and for each process separately. Values with and without the cut applied are listed in the table for comparison.

The first column of table (4.13) shows the change in lepton transverse momentum. The overall lepton p_T is increased by a few GeV. Since the value for $t\bar{t}$ events remains unchanged, the increase is caused by SUSY events alone. Before requiring two same flavour, opposite sign leptons, SUSY leptons had an average transverse momentum of 53.8 GeV. After the cut is applied, lepton p_T is found to increase by approximately 12 GeV. Many leptons coming from W and τ decay are rejected, while signal events are kept. Due to the mass of the decaying mothers, leptons from W-bosons and τ-leptons are in general expected to have lower energy than leptons from sparticle decay.

The second column shows the average number of jets before and after the cut. The overall number of jets is reduced by roughly three, an effect mainly caused by the rejection of $t\bar{t}$-events. A reduction of the number of jets is expected in $t\bar{t}$-events when lepton multiplicity is imposed. $t\bar{t}$-decays could produce up to six jets. In events with two leptons, both Ws have decayed leptonically, and the hadronic activity is reduced. This causes the drop in the average number of jets in $t\bar{t}$-events seen in table (4.13). A similar, but not so dramatic effect, is seen for SUSY events where the average jet multiplicity decreases by one jet. Supersymmetric background consists mostly of Ws and τs, which generally decay further to hadrons or leptons according to branching ratios given in equation (4.11), section 4.3. The dilepton requirement removes the hadronic decay of Ws and τs, causing a decrease in jet multiplicity.

A reduction of jet transverse momenta in $t\bar{t}$-events is seen in the third column. One explanation for this effect is that the overall hadronic activity is reduced. Especially events with W-bosons decaying into jets are rejected. Some of these jets could have high energy and by excluding them the jet-p_T decrease slightly.

Finally, the effect of the cut on missing transverse energy is investigated. We expect an increase in the mean value of missing energy for $t\bar{t}$ events since neutrinos always follow charged leptons in W decays. From table (4.13), 4th column, the effect is clear, the missing transverse energy in top events is increased by nearly 30 GeV, when the cut is applied. In SUSY events the average E_T^{miss} is, more surprisingly, reduced by approximately 40 GeV after the cut. One reason could be that background events containing both neutrinos and LSPs, see eq. (4.14), are rejected. The missing

transverse energy in such events will in general be larger than in events with LSPs only. Whether this is the case requires further investigations.

		$\langle p_T \rangle$ leptons (GeV)	$\langle Number \rangle$ of jets	$\langle p_T \rangle$ jets (GeV)	$\langle E_T^{miss} \rangle$ (GeV)
S+B	No cut	56.9	5.2	55.3	102.6
	Cut	64.1	8.3	93.5	213.6
$t\bar{t}$	No Cut	54.0	5.0	45.8	79.2
	Cut	53.4	7.4	67.4	93.9
SUSY	No cut	66.4	6.7	96.8	241.9
	Cut	67.9	8.6	101.7	257.3

Table 4.14: Mean values of selected variables for signal plus background (S+B), before and after requiring two same flavour, opposite sign, leptons and four jets of $p_{T,1} > 100\,GeV$ and $p_{T,2,3,4} > 50\,GeV$.

4.5.3 Requirement 2: four high-p_T jets

Previously we studied how the jet multiplicity changed in three different p_T-ranges, for both signal, $t\bar{t}$ and SUSY background, see figure (4.16), section 4.4. SUSY events also tend to have a larger number of hard-p_T jets than $t\bar{t}$, as shown in table (4.11), section 4.4. This tendency is supported by table (4.13) where jets in SUSY-events have p_T twice as large as jets in $t\bar{t}$-events. These considerations motivate the next cut, where at least four jets are required. Since the signal produce one high-p_T jet, we require one of them to have $p_T \geq 100\,GeV$, and the three others to have $p_T \geq 50\,GeV$. This cut will be referred to as the hard-p_T cut. The effect of this cut can be seen in table (4.14), which is structured in the same way as table (4.13).

The most striking feature of the hard-p_T cut is the huge $t\bar{t}$ rejection factor, already shown in table (4.12) earlier in this section. This effect is also visible in table (4.14). All signal plus background values are dominated by SUSY-processes rather than $t\bar{t}$, after the cut is applied. With a mean p_T of 45.8 for jets before the cut, most $t\bar{t}$ events are rejected.

The overall lepton transverse momenta increases by 8 GeV as a result of the p_T cut on jets. However, no significant changes are observed in either $t\bar{t}$ or SUSY-events. We know from table (4.14) that SUSY events generally have leptons with higher transverse momenta than $t\bar{t}$ events. We also know that a significantly larger number of SUSY events survive the hard-p_T cut compared to $t\bar{t}$-events, see table (4.12). It then becomes evident that the increase in the overall lepton transverse momenta, is caused by the fact that SUSY-events now dominate the sample.

Next we see that the average number of jets increases for all processes as a result of the hard-p_T cut. Obviously it should, since requiring at least four jets per event automatically rise the average jet multiplicity, by roughly three per event.

The overall increase of jet transverse momentum (tab. 4.14) is also a trivial effect of the hard p_T cut. The average jet transverse momentum will get larger once the soft-jet-events are suppressed. Again we see that SUSY events dominate the sample causing the average jet transverse momentum to increase by nearly 40 GeV.

An increase in missing transverse energy is also seen in table (4.14) for both SUSY and $t\bar{t}$ events. This could be due to the fact that events passing the hard p_T cut are in general very energetic. The more energy available in a system the more likely it is for neutrinos or LSPs to carry away huge fractions of it.

		$\langle p_T \rangle$ leptons (GeV)	$\langle Number \rangle$ of jets	$\langle p_T \rangle$ jets (GeV)	$\langle E_T^{miss} \rangle$ (GeV)
S+B	No cut	56.9	5.2	55.3	102.6
	Cut	57.8	5.7	69.7	185.2
$t\bar{t}$	No Cut	54.0	5.0	45.8	79.2
	Cut	52.6	5.0	48.5	137.2
SUSY	No cut	66.4	6.7	96.8	241.9
	Cut	68.2	7.0	100.4	281.5

Table 4.15: Mean values of selected variables for signal plus background (S+B), before and after requiring two same flavour, opposite sign, leptons and $E_T^{miss} > 100\,GeV$.

4.5.4 Requirement 3: large missing transverse energy

In the last part of section 4.4 a comparison of the E_T^{miss}-distributions for signal and background was made. Figure (4.17) showed this variable to be very powerful in rejecting $t\bar{t}$-background, especially by requiring missing transverse energy to be larger than 100 GeV. Table (4.15) shows the effect of this cut.

Again, the huge $t\bar{t}$ rejection can be understood by looking at the mean value of missing transverse energy before the cut. Table (4.15) shows a value well below 79 GeV, indicating that most events will be rejected by a requirement of 100 GeV. SUSY events, with initially $\langle E_T^{miss} \rangle \simeq 240\,GeV$, are nearly unaffected by the cut, and dominate the sample.

The general impression from table (4.15) is that the cut on missing transverse energy seems to cause very few changes in other measurables. Jet multiplicity and transverse momenta, in $t\bar{t}$-events, are fairly similar before and after the cut, and is due to the correlation between missing energy and leptons. The E_T^{miss} cut is applied on a sample that already contains two same flavour, opposite sign, leptons. These events have a larger missing transverse energy than $t\bar{t}$-events in general, since leptonic decay of the top quark is always followed by neutrinos. The event topology is already determined by the cut on leptons and the missing transverse energy requirement does not change it further. Only small changes are seen in SUSY-events, where all values increase slightly after the cut is applied. Increase of missing transverse energy for both processes is of course observed, for $t\bar{t}$ the average rises by nearly 60 GeV while the SUSY average increases by 40 GeV.

	S+B	SUSY	$t\bar{t}$
All cuts	10 189	9 088	1 101
$-M_{eff}$	10 267	9 145	1 123
$-E_T^{miss}$	12 909	10 299	2 610
− lepton $p_T > 10\,GeV$	21 586	16 324	5 253
− jet $p_{T1} > 100, p_{T2,3,4} > 50$	26 777	17 889	8 889

Table 4.16: Effect of omitting one cut

4.5.5 All cuts except from one

It is of course interesting to see how effective and necessary the TDR-cuts are. One way is to study the effect of omitting one at a time. In this way the importance of each cut becomes clear. Table (4.16) shows the number of events that pass all cuts,

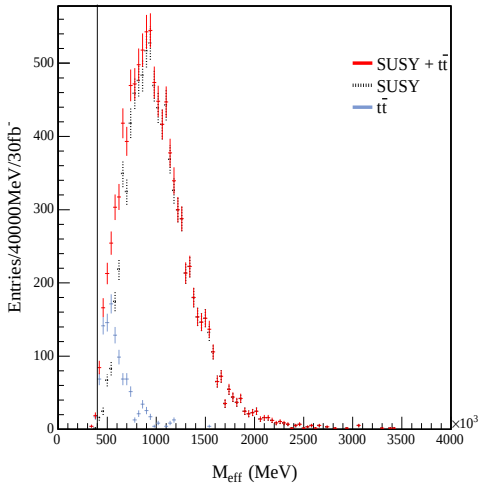

Figure 4.18: Effective mass distribution for events passing the following cuts to same flavour opposite sign leptons with $p_T \geq 10\,GeV$, and at least four jets that fulfill $p_{T1} \geq 100\,GeV, p_{T2,3,4} \geq 50\,GeV$ and $E_T^{miss} > 100\,GeV$.

and then how many that pass when one and only one cut is left out. If the numbers do not change much when a cut is omitted, then it is not necessarily effective.

The first cut omitted is the effective mass requirement. From table (4.16) we see that omitting this cut is of no important consequence. Figure (4.18) also shows that there is not much to gain on this cut when all other cuts are applied. 0.6% of SUSY events and 2% of $t\bar{t}$ events are rejected. The reason is of course that constraints are already put on missing transverse energy and jet transverse momentum which are the constituents of M_{eff}. This variable seems to be contained in the requirements on jet transverse momentum and missing transverse energy.

As expected, omitting the demand for large missing transverse energy, has very different effect on SUSY and $t\bar{t}$. The number of $t\bar{t}$ events is more than doubled, while SUSY events increase by approximately 18 %.

The first cut omitted that actually cause the total number of events to be doubled is surprisingly lepton transverse momentum. When this cut is omitted 56% more SUSY and 80% $t\bar{t}$ events are recovered. The most dramatic effect is obtained by leaving out requirements on jet multiplicity and p_T. Then the number of accepted SUSY events increase by 50% and the corresponding number for $t\bar{t}$ is 12%

Figures 4.25-4.29 shows the effect of omitting one cut at the time, giving a visual impression of the effect of the cuts.

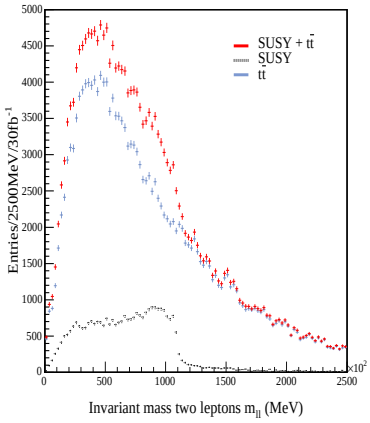

Figure 4.19: Invariant mass of two leptons

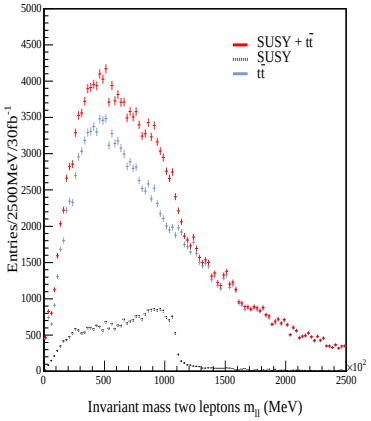

Figure 4.20: Invariant mass of two same flavour opposite sign leptons

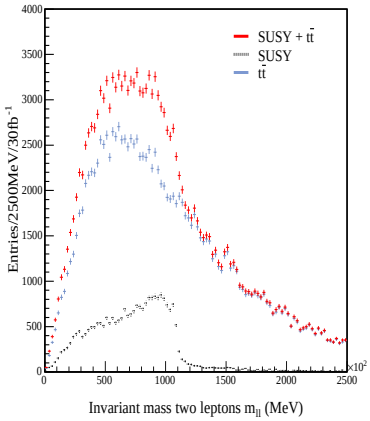

Figure 4.21: Invariant mass of two same flavour opposite sign leptons with $p_T > 10\,GeV$

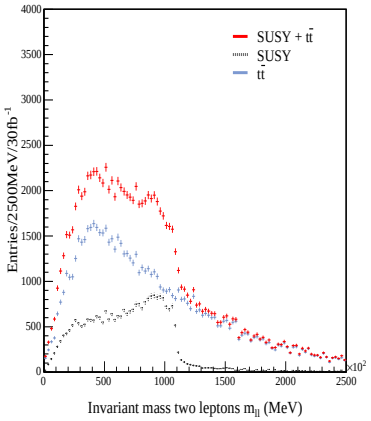

Figure 4.22: Invariant mass of two same flavour opposite sign leptons in events with $M_{eff} > 400\,GeV$

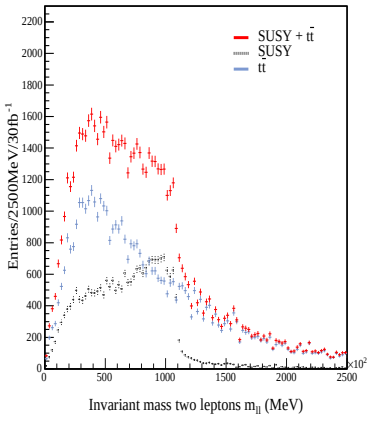

Figure 4.23: Invariant mass of two same flavour opposite sign leptons in events with $E_T^{miss} > 100\,GeV$

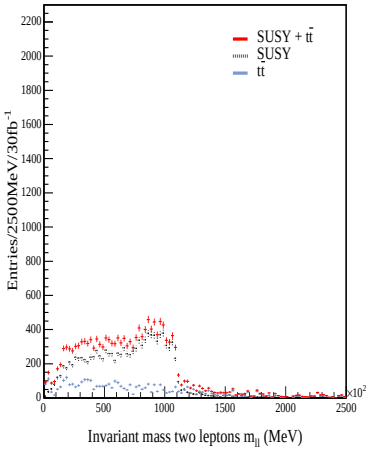

Figure 4.24: Invariant mass of two same flavour opposite sign leptons in events with four jets with $p_{T1} > 100\,GeV$ and $p_{T234} > 50\,GeV$

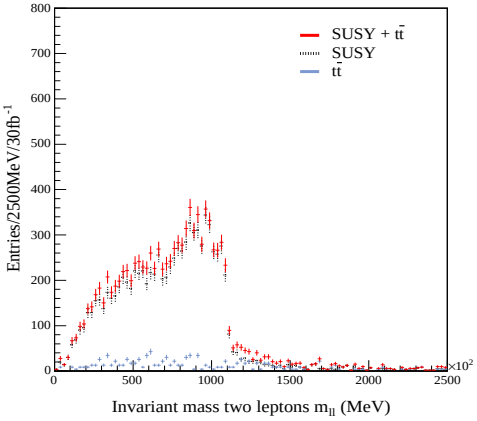

Figure 4.25: Invariant mass of two leptons, all cuts applied

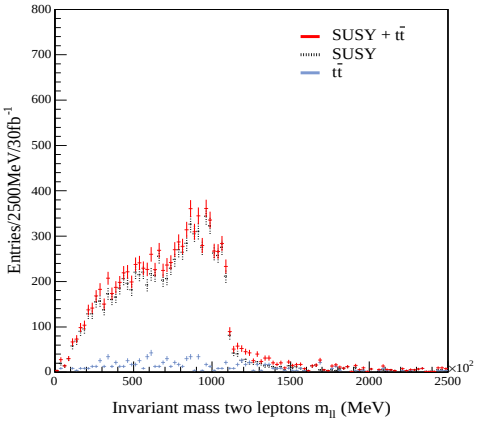

Figure 4.26: Invariant mass of two leptons, all cuts except $M_{eff} > 400\,GeV$

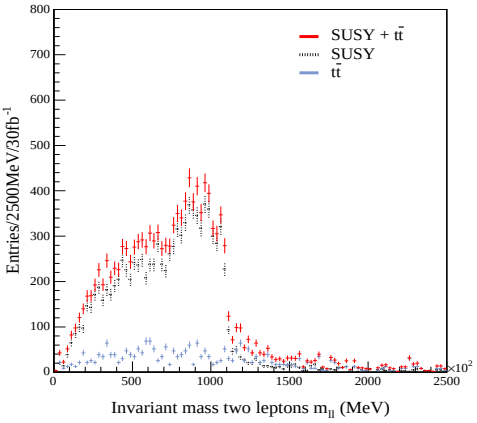

Figure 4.27: Invariant mass of two leptons, all cuts except $E_T^{miss} > 100\,GeV$

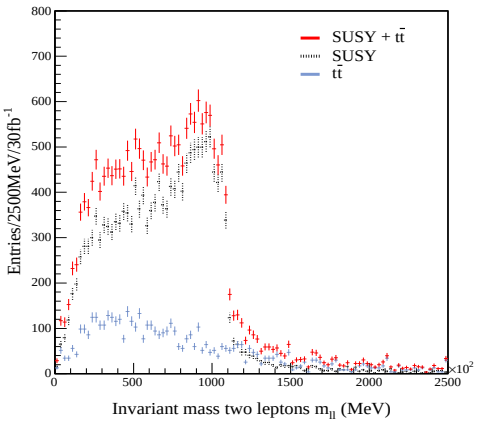

Figure 4.28: Invariant mass of two same leptons, all cuts except lepton $p_T > 10\,GeV$

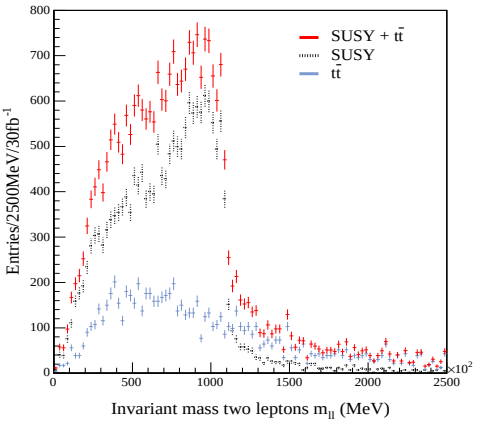

Figure 4.29: Invariant mass of two leptons, all cuts except jet $p_{T1} > 100\,GeV, p_{T234} > 50\,GeV$

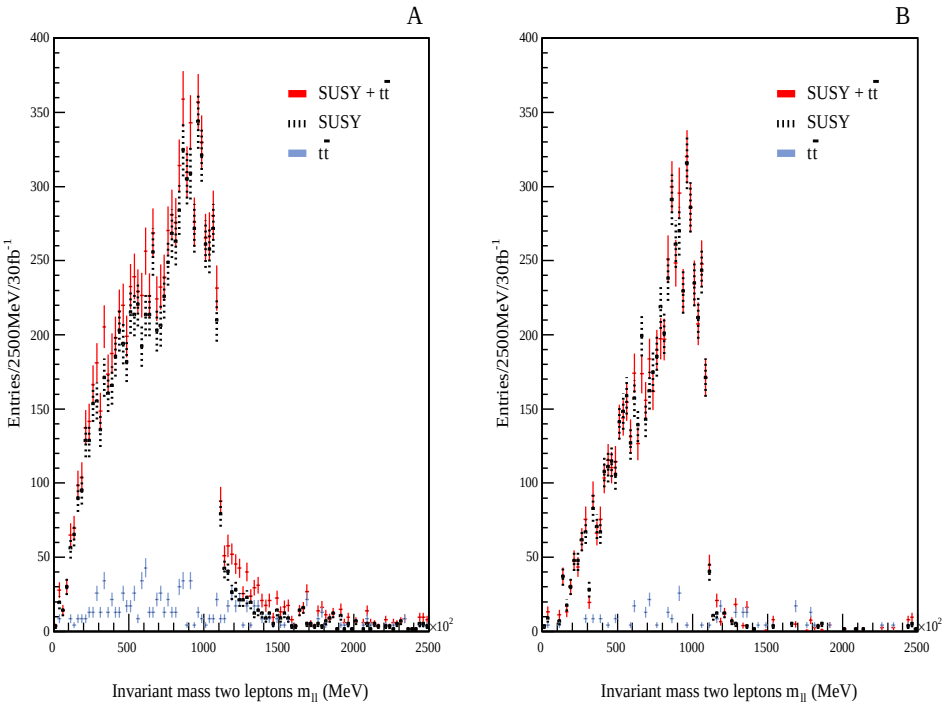

Figure 4.30: Invariant mass distribution for two leptons. A: Events that passed all the cuts in section 4.5. B: Events from A flavour subtracted.

4.6 Flavour subtraction

When all cuts are applied there is still one more technique left to remove so called uncorrelated leptons. We know from section 4.3 that two same flavour, opposite sign, leptons can be produced in background processes. We saw that the leptons usually were produced in decay of W-bosons or taus, and that the two leptons came from two different branches in the decay. This means that the flavours of the two leptons are uncorrelated, they have the same flavour only by chance. This is not the case for the signal decay chain, where flavour conservation forces the leptons to be of the same kind.

In the case of background processes the probability is equal of getting e^+e^-, $\mu^+\mu^-$, $e^+\mu^-$ and μ^+e^-. Subtracting opposite flavour, opposite charge events, $e^+\mu^-$, is then statistically the same as subtracting uncorrelated same flavour, opposite charge events, e^+e^-. This is a very powerful technique for removing background in invariant mass distributions containing leptons and is usually referred to as flavour subtraction.

Figure (4.30)A shows the invariant mass distribution of two leptons from data sample that passing all cuts described in section 4.5. Part B shows the flavour subtracted distribution. Both the shape and the maximum of the distribution are predicted by kinematical constraints (see chap. 5). It is important to note that all events in figure (4.30)A have two same flavour opposite sign leptons. The point is however, that some of these do not come from the signal chain, but from W and τ decays in SUSY or Standard Model background. These uncorrelated leptons pollute the invariant mass distribution by changing its shape and distorting its maximum. This polluted invariant

mass distribution is shown in figure (4.30)A.

If we during our analysis also calculate the invariant mass of every pair of $e^+\mu^-$ and μ^+e^- and subtract this distribution from the distribution in figure (4.30)A we end up with (4.30)B. By doing this we remove most uncorrelated leptons coming from the background while keeping the correlated leptons from the signal, since pairs of $e^+\mu^-$ and μ^+e^- never arise from the cascade decay. The distribution in (4.30)B resembles the theoretical prediction of the shape, making us believe that the background in this distribution is negligible.

4.7 Summary and Conclusion

In this chapter we have studied the features of the signal chain in detail and seen that even in an artificial pure signal sample the signatures are not completely clear. Even if only one jet and two leptons are expected we saw events with more jets and less leptons. Atlfast is only a parameterization of the real ATLAS detector but the premature studies of section 4.2 still have an important lesson for us. Some signal will be lost due to detector efficiency, this loss can only be avoided by making the detector perfect. We also saw the effect of underlying events by getting a jet multiplicity far beyond what was expected from the signal chain alone. This indicate the crucial role of QCD scattering at the LHC and illustrates the difficulty in picking the right jet in the cascade decay.

We then continued by studying processes that could mimic the signal signatures. Processes from both supersymmetry and the Standard Model were taken into account. We found that the clearest general difference between signal and background was whether the lepton flavours were correlated or not. In signal events lepton flavours were always similar, while in background events they were similar by chance.

We moved on to apply a set of cuts to a data sample containing a mixture of signal and background (both SUSY and $t\bar{t}$) hoping to extract the signal chain from the background processes. We based our investigations on a sample that already fulfilled two same flavour opposite sign leptons since this is the leading measurable feature of signal events. We studied the effects of the cuts and their impact on each other.

Worth mentioning is that a requirement of at least four jets, where one is required to have transverse momentum above 100 GeV and the three others above 50 GeV, alone removed 98% of $t\bar{t}$ and 60% of SUSY processes. This cut seems too hard and needs further investigation and possibly tuning. Tuning of the cuts were unfortunately not compatible with the time limits on the investigations in this thesis.

The importance of each cut was also studied, by omitting one at a time. Lepton and jet transverse momentum requirements were found to have the largest rejection factor.

When all cuts were applied 20% pure signal, 0.5% SUSY background and 0.01% $t\bar{t}$ events passed the cuts, the percentages are relative to the number of events before any cuts were applied. In these events, the internal distribution of signal, SUSY and $t\bar{t}$ background is 70%, 23% and 7% respectively. The fact that 80% of pure signal events are lost after applying the cuts strongly suggests that the cuts are too hard.

This chapter have shown that it is possible to extract a nearly pure signal sample by applying certain requirements on events. Such a sample is needed in the next chapter when the signal chain (fig. 4.4) will be used for determination of sparticle masses.

Chapter 5

Mass measurements

Chapter 4 showed how to extract a certain squark decay chain from a data sample consisting of SUSY and $t\bar{t}$-processes. After selecting and extracting the decay chain from the background, the question of mass measurements arises. Sparticle mass measurements are interesting and necessary for a complete description of a supersymmetric theory of particle physics.

This chapter will illustrate sparticle mass measurements through the determination of endpoints of various invariant mass distributions. A description of how to move from endpoint measurements to masses will be given. The method will be used to determine the masses of sparticles, using data from both fast and full simulation.

Data from full simulation were obtained from the web page of the ATLAS SUSY working group [14], which produced a sample of 10^5 events using Herwig(6.4) through the Athena 6.0.3 interface. In addition, Herwig (6.5)and Athena 7.0.3 were used for fast simulation. The number of events, for both full and fast simulation, corresponds to an integrated luminosity of $5.13 fb^{-1}$, or roughly six months of running at low luminosity.

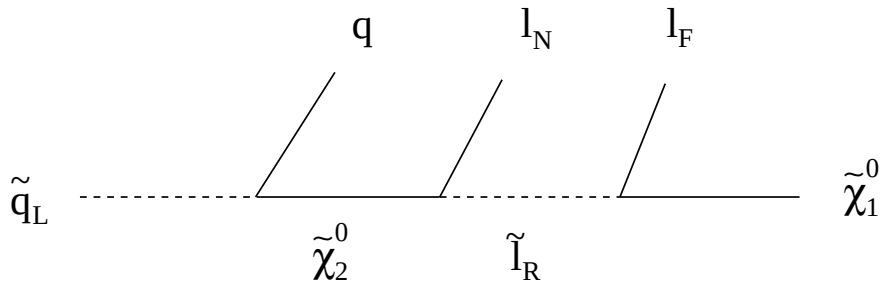

Figure 5.1: Squark decay

5.1 The nature of supersymmetric mass measurements

Every sparticle decay in an R-parity conserving theory has a stable lightest supersymmetric particle (LSP) as an end product. As already mentioned in chapter 4, the LSP is $\tilde{\chi}_1^0$ at the DC1-point. It is a heavy neutral, weakly interacting particle that will traverse ATLAS undetected, resulting in a large missing energy. For this reason the invariant mass of the decay products will not peak at the mass of their mother but be continuously distributed within kinematical limits. Luckily particle decays do have kinematical constraints, an example of which will be given in section 5.2. The constraint will be visible as an endpoint in the invariant mass distribution of the detectable particles. If there are as many endpoints as unknown masses, the former can be used for calculating the latter [6].

In the squark decay chain in figure (5.1) there are four unknown sparticle masses $m_{\tilde{q}_L}$, $m_{\tilde{\chi}_2^0}$, $m_{\tilde{l}_R^\pm}$ and $m_{\tilde{\chi}_1^0}$. In order to measure these masses, we need four invariant mass distributions of the detectable particles in the signal chain. These are; the invariant mass of the two final leptons m_{ll}, the two leptons and the jet q from squark decay, m_{qll}, the invariant mass of the quark q and the nearest lepton l_N[1] from the χ_2^0 decay, m_{ql_N}, and finally, the invariant mass of the quark q and the lepton that originates from $\tilde{l}_R$, m_{ql_F}[2]. The notation using subscripts N and F to distinguish leptons was introduced in [13]. All these distributions are theoretically obtainable, but problems arise when the masses are to be constructed from data.

The invariant mass distribution of the two final leptons is relatively easy to obtain. There are good reasons to believe that the experimental curve will resemble the theoretical one, simply because the only way to pick the 'wrong' electrons, i.e. electrons not coming from the signal chain, is from a background process. Cuts and flavour subtraction have reduced the number of leptons coming from such processes to a minimum, and we expect the majority of leptons to originate from the cascade decay.

Invariant mass distributions containing jets are more difficult to obtain from experimental data. Section 4.2 of chapter 4 showed that the jet multiplicity in signal events is high. The section showed that if a single signal chain is considered, it is not necessarily possible to pick out the jet coming from squark decay. In events containing more than one decaying sparticle the situation gets even more complicated. A pair of sparticles is produced in every SUSY event, and if one decays through the chain in figure (5.1), the other is free to decay through any allowed mode. If the latter is a gluino or a squark, its decay will involve a high energy jet as seen in tables (4.3) and (4.6), chapter 4. That is why events passing all cuts usually have more than one high-p_T jet. It is also apparent that it is difficult to distinguish a jet from the signal chain from jets of other origins.

For the invariant mass distribution of two leptons and a jet the strategy has been to pick out the two hardest jets in the event and use them to calculate two values for m_{qll}. These values are ordered and stored in two different histograms, one containing the smaller values and the other containing the larger ones. Usually one chooses to use the jet that gives the lowest value of m_{qll} in order to prevent the background from hiding the endpoint. Both the lower and higher mass distributions (fig. 5.2 and 5.3) drop at approximately 500 GeV, the drop being more distinct in figure (5.2) than in figure (5.3), which is polluted by background. The two plots show that the endpoint can be easily lost if jets are not carefully chosen. It is however important to notice that even when we choose the jet giving the lowest value for m_{qll} we do not know if it comes from the signal chain or not. This leads to a systematic uncertainty we have to deal with.

At the LHC it will not be possible to distinguish l_N from l_F, causing difficulties for

[1] The lepton is denoted l_N, N for Near (the squark)

[2] F for Far, the lepton that is far from the decaying squark

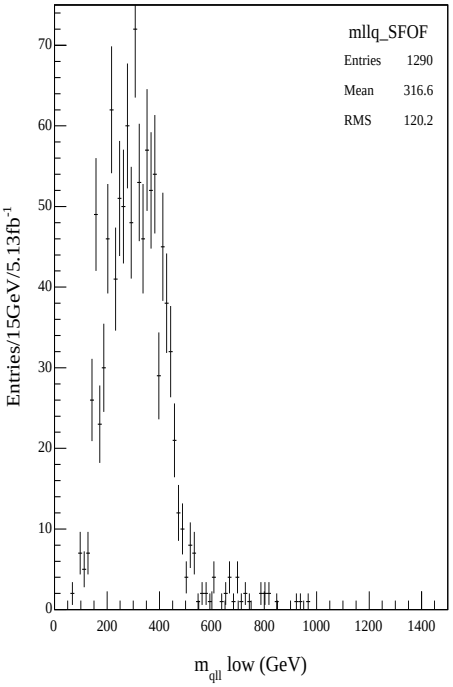

Figure 5.2: Invariant mass of two leptons and a quark. Jet configuration that gives the lowest mass

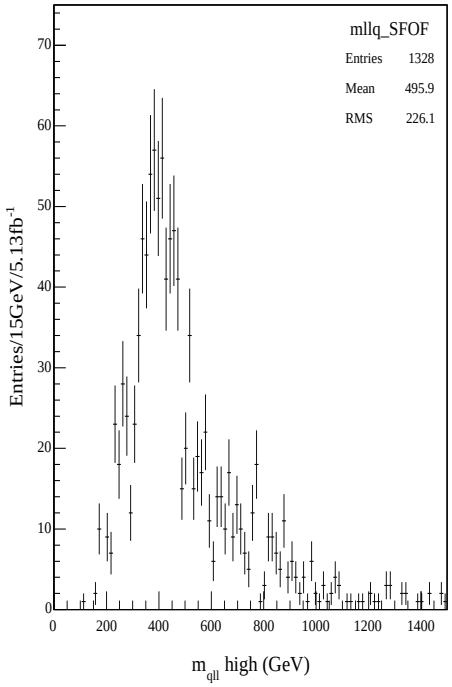

Figure 5.3: Invariant mass of two leptons and a quark. Jet configuration that gives the highest mass

the calculation of m_{ql_N} and m_{ql_F}. Instead one chooses to create two new distributions m_{ql}^{high} and m_{ql}^{low} related to the theoretical m_{ql_N} and m_{ql_F} through equation (B.3) in appendix B. These distributions are built in more or less the same way as for the m_{qll} distribution.

The jet that gives the lowest value of m_{qll} is selected and then used in combination with the two leptons to calculate m_{ql}. m_{ql}^{high} is the largest of the two values and m_{ql}^{low} the lowest. Both distributions are kept and their endpoints are measured and used for calculating the sparticle masses.

The considerations above show that when leptons and jets are selected and used as input to invariant mass distributions, the uncertainties in picking up the wrong combinations subsist, even in data samples that passed all cuts.

5.2 Extracting masses from endpoints

The theoretical endpoint or maximum of an invariant mass distribution is obtainable through kinematical considerations. This is easily illustrated by an example. Consider the part of the squark decay chain in figure (5.1) where $\tilde{\chi}_2^0$ decays into $\tilde{l}_R$ and l_N, and $\tilde{l}_R$ continues decaying into $\tilde{\chi}_1^0$ and l_F. This decay is illustrated in figure (5.4), where on the left hand side the neutralino ($\tilde{\chi}_2^0$) decays into slepton and lepton while the slepton on the right hand side decays in its rest frame.

Let us assume massless leptons for simplicity. In the rest frame of $\tilde{\chi}_2^0$ energy and

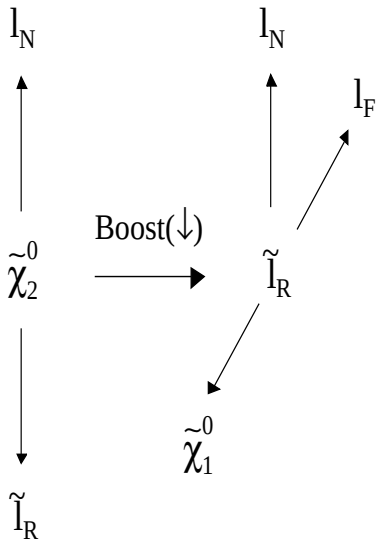

Figure 5.4: $\tilde{\chi}_2^0$ decay from a kinematical point of view

momentum conservation gives

$$\begin{aligned} m_{\tilde{\chi}_2^0} &= E_{\tilde{l}_R} + E_{l_N} && (5.1)\\ \boldsymbol{0} &= \boldsymbol{p}_{\tilde{l}_R} + \boldsymbol{p}_{l_N} && (5.2) \end{aligned}$$

Equation (5.2) implies that $\boldsymbol{p}_{l_N} = -\boldsymbol{p}_{\tilde{l}_R}$. Next in natural units ($\hbar = c = 1$) the relativistic energy/momentum relation gives

$$\begin{aligned} p_{\tilde{l}_R}^2 &= E_{\tilde{l}_R}^2 - m_{\tilde{l}_R}^2 \\ &= (m_{\tilde{\chi}_2^0} - E_{l_N})^2 - m_{\tilde{l}_R}^2 \\ &= (m_{\tilde{\chi}_2^0} - p_{l_N})^2 - m_{\tilde{l}_R}^2 \end{aligned}$$

$$\begin{aligned} 2m_{\tilde{\chi}_2^0} p_{l_N} &= m_{\tilde{\chi}_2^0}^2 - m_{\tilde{l}_R}^2 \\ p_{l_N} &= \frac{(m_{\tilde{\chi}_2^0}^2 - m_{\tilde{l}_R}^2)}{2m_{\tilde{\chi}_2^0}} && (5.3) \end{aligned}$$

In the rest frame of $\tilde{l}_R$ the expressions for p_{l_N} and p_{l_F} is obtained in a similar manner:

$$p_{l_N} = \frac{(m_{\tilde{\chi}_2^0}^2 - m_{\tilde{l}_R}^2)}{2m_{\tilde{l}_R}} \quad (5.4)$$

$$p_{l_F} = \frac{(m_{\tilde{l}_R}^2 - m_{\tilde{\chi}_1^0}^2)}{2m_{\tilde{l}_R}} \quad (5.5)$$

The invariant mass of the final two leptons l_N and l_F becomes

$$\begin{aligned} m_{ll}^2 &= (E_{l_N} + E_{l_F})^2 - (\boldsymbol{p}_{l_N} + \boldsymbol{p}_{l_F})^2 \\ &= 2p_{l_N}p_{l_F} - 2\boldsymbol{p}_{l_N} \cdot \boldsymbol{p}_{l_F} \\ &= 2p_{l_N}p_{l_F}(1 - \cos\theta). && (5.6) \end{aligned}$$

Where we have used that $P_l = E_l$ since the leptons are assumed massless. By combining equation (5.6) with equations (5.4) and (5.5) and requiring $\cos\theta = -1$, the following expression, for the maximum value of the m_{ll} distribution, is obtained:

$$(m_{ll}^{max})^2 = \frac{(m^2_{\tilde{\chi}^0_2} - m^2_{\tilde{l}_R})(m^2_{\tilde{l}_R} - m^2_{\tilde{\chi}^0_1})}{m_{\tilde{l}_R}}. \tag{5.7}$$

Equation (5.7) shows how the endpoint of the invariant mass distribution of the two leptons is theoretically determined by the three sparticle masses involved in the decay. Similar relations between masses and endpoints can be obtained for the other invariant mass distributions mentioned but the calculations are more complicated and out of scope for this thesis. In addition is the $(m_{ll})^{max}$ endpoint the only one to be uniquely determined, the other endpoints depend on relations between the sparticle masses involved. The full formulae are shown in appendix B, section B.1.

When the endpoints are measured the sparticle masses can be extracted by inverting the formulae in section B.1. Since the number of endpoints coincides with the number of unknown masses a set of four equations with four unknowns is obtained. Solving this set of equations is not as easy as it sounds due the non-uniqueness of the endpoint/mass relations. Instead of one set of unique expressions for the sparticle masses we get six sets, see section B.2, all depending on the relation between the sparticle masses given in equations (B.2) and (B.3). Since the masses are unknown, the mass relations are unknown too, making it impossible to know which mass/endpoint relation to use. Instead we need to consider all six solutions in section B.2 and use the measured values of the endpoints as input. Luckily it turns out that most sets of solutions will return unacceptable masses for a given set of endpoints [6]. However this does not mean that only one solution remains, but that the number of acceptable solutions will be reduced.

5.3 Endpoint measurements from Atlfast and Atlsim data

In order to find the endpoints of invariant mass distributions, straight lines were used to fit the endpoint region (also referred to as the edge). Seven measurements were made by changing the binning and/or the fit range for both simulations. Variations in the fit parameters cause some endpoint values to vary dramatically. Independent criteria for which measurement to pick were therefore needed. We decided to choose a measurement as long as

$$\frac{\chi^2}{NDF} < 2.5, \tag{5.8}$$

and all measurements in this section are chosen on the basis of this criteria. χ^2, or chi-square, is defined as;

$$\chi^2 = \sum_{i=1}^{n} \left(\frac{x_i - \mu_i}{\sigma_i} \right)^2, \tag{5.9}$$

where x_i are the measured variables, μ_i theoretical means and σ_i standard deviations. The chi-square characterizes the fluctuations in the data x_i with respect to the theoretical mean. NDF stands for Number of Degrees of Freedom and is related to the number of independent variables or measurements in χ^2. The fraction $\frac{\chi^2}{NDF}$ should be close to one for a good fit [43]. All measurements in this section are chosen on the basis of this criteria.

The results from fast simulation measurements are stated in table (5.1), see appendix C for full details. 876 events passed all cuts and the corresponding invariant mass distributions are plotted in figures (5.5)-(5.8), where also linear fits to the endpoints are shown. The light (blue) histograms are the theoretical predictions, while

the black points with error bars are obtained from Atlfast data. The theoretical distributions are obtained from the formulae of section B.1 in appendix[3] B with masses calculated by ISASUSY [18] as input.

Endpoints measured for full simulation data are summarized in table (5.2), see appendix C. Figures (5.9)-(5.12) show the four invariant mass distributions for this data set. 839 events pass all cuts which is 5% less than the signal events in fast simulation.

n	m_{ll} (GeV)		m_{qll} (GeV)		m_{ql}^{low} (GeV)		m_{ql}^{high} (GeV)	
	Endpoint	Error	Endpoint	Error	Endpoint	Error	Endpoint	Error
1	101.2	0.48	501.2	4.3	316.7	5.1	429.1	9.2
2	100.2	0.43	498.0	4.0	317.4	4.7	457.6	9.6
3	102.7	0.87	503.0	6.4	321.0	4.8	445.7	10.0
4	103.7	0.60	502.6	6.1	322.6	5.1	413.9	9.6
5	103.3	0.24	500.2	6.5	330.8	4.9	447.2	9.2
6	102.7	0.61	498.4	5.8	325.1	4.7	425.9	9.2
7	102.8	0.92	500.4	4.2	325.5	4.7	408.5	9.0
Mean	102.4	0.6	500.5	5.4	322.7	4.9	432.6	9.4

Table 5.1: Results of endpoint measurements from fast detector simulation data

n	m_{ll} (GeV)		m_{qll} (GeV)		m_{ql}^{low} (GeV)		m_{ql}^{high} (GeV)	
	Endpoint	Error	Endpoint	Error	Endpoint	Error	Endpoint	Error
1	101.8	0.58	502.6	4.8	326.3	6.6	422.9	5.7
2	103.9	0.74	498.4	5.8	320.0	6.1	421.8	5.1
3	105.1	0.78	498.4	5.7	324.1	6.2	418.2	6.5
4	104.0	0.71	505.1	5.9	321.9	5.9	421.8	4.9
5	101.9	0.58	502.2	5.0	311.9	6.3	423.4	6.1
6	104.3	0.78	500.2	5.2	322.6	5.5	413.0	4.9
7	101.7	0.52	503.2	5.4	328.4	5.5	425.4	5.2
Mean	103.2	0.7	501.4	5.4	322.2	6.0	420.9	5.4

Table 5.2: Results of endpoint measurements, full simulation data

By comparing tables (5.1) and (5.2), we find that the mean values in the last row are in agreement with each other. The exception is m_{ql}^{high} which differs by 12 GeV. This is also reflected in the errors, which are purely statistical and obtained from the fitting procedure. For fast simulation the error in m_{ql}^{high} is 9.4 GeV, while the corresponding number in table (5.2) is 5.4 GeV. A possible explanation for this difference is seen by comparing figures (5.7) and (5.11). The former has a polluted endpoint region, making a good fit hard to obtain, while the latter endpoint is rather distinct and easier to fit.

[3]The solution in Region(1,3) is the correct one

It is also worth mentioning that the error in both m_{ll} measurements are significantly smaller than the rest. As seen in figures (5.5) and (5.9) the edge and endpoint is clearly defined. This makes them easy to fit and the statistical error decrease.

Also the simulated points in figures (5.5)-(5.12) need commenting. Except from the m_{ll}-distributions (fig. 5.5, 5.9), none of the curves reproduce the theory distributions. This is due to the difficulties in picking the correct particles for the different distributions, and constitutes the combinatorial background. Dilepton distributions are hardly influenced by such background, since the leptons in an event sample most likely come from the cascade decay. For the other invariant mass distributions the situation is different. In the m_{qll} and m_{ql}-distributions problems arise because of the jet selection. We can never be sure to pick the jet coming from the signal squark and this is mainly the reason for the observed deviation from theory, as seen in figures (5.6-5.8) and (5.10-5.12).

Additional pollution in the simulated distributions come from background processes, especially $\tilde{\chi}_2^0$s produced by other sparticles than $\tilde{q}_L$, see for instance table (4.7). From chapter 4 however, we know that this background is small.

Another reason for the difference between theoretical and simulated shapes is simply the low statistics. Each event sample contains roughly 850 events, with the effect that statistical variations play an important role. An increase of statistics is expected to give simulated distributions more similar to the theoretical ones. Improvements, with respect to the shape, are also obtainable through reduction of combinatorial background [6].

At this point it would be reassuring to see simulated distributions that actually follows the theoretical prediction. Full simulation ntuples contain Monte Carlo truth information. This information makes it possible to select pure signal events, and calculate the invariant mass distribution using particles from the correct decays in the decay chain. Figure (5.13) shows these distributions. Despite low statistics, the shape of the generated distributions agrees well with the theoretical prediction. Figure (5.13) gives us confidence that the kinematics of signal events behaves as predicted. By comparison with the previously studied distributions, it also illustrates the huge impact of combinatorial background.

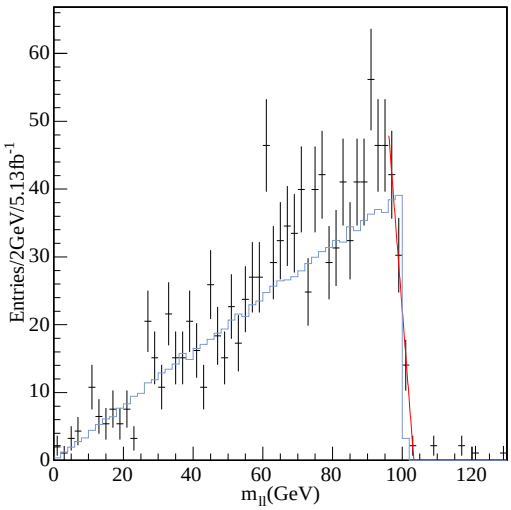

Figure 5.5: Invariant mass distribution of the two final leptons (points with error bars) together with the theoretical prediction (light curve). Fast simulation data.

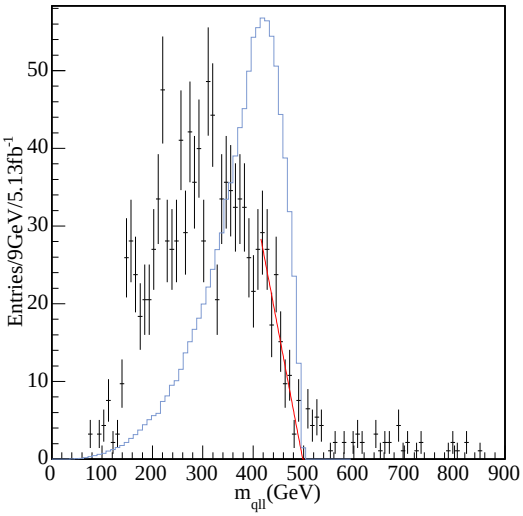

Figure 5.6: Invariant mass distributions of the two final leptons and a quark (points with error bars) together with the theoretical prediction (light curve). Fast simulation data.

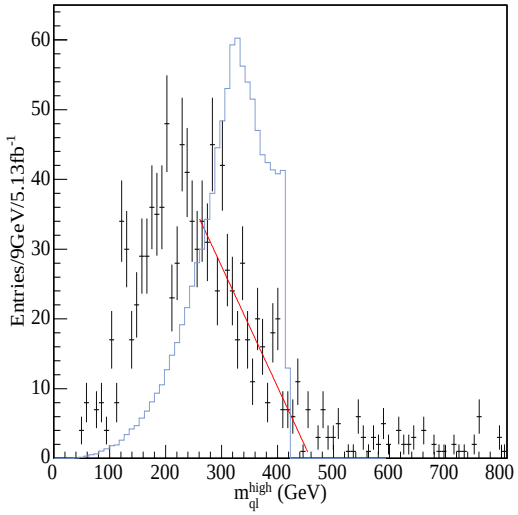

Figure 5.7: Invariant mass distribution of lepton and quark, the combination that gives the largest mass (points with error bars) together with the theoretical prediction (light curve). Fast simulation data.

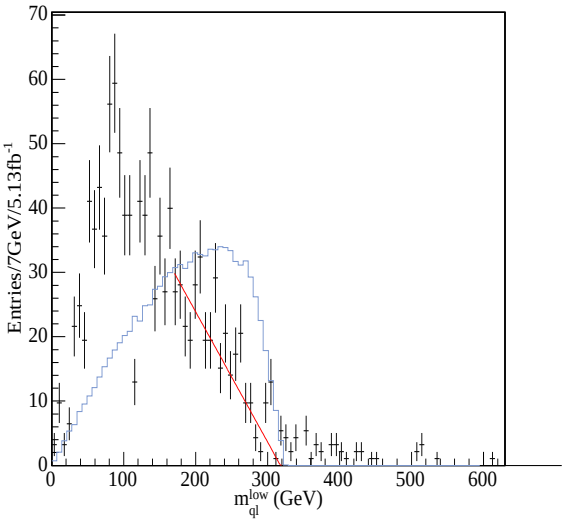

Figure 5.8: Invariant mass distribution of lepton and quark, the combination that gives the smallest mass (points with error bars) together with the theoretical prediction (light curve). Fast simulation data.

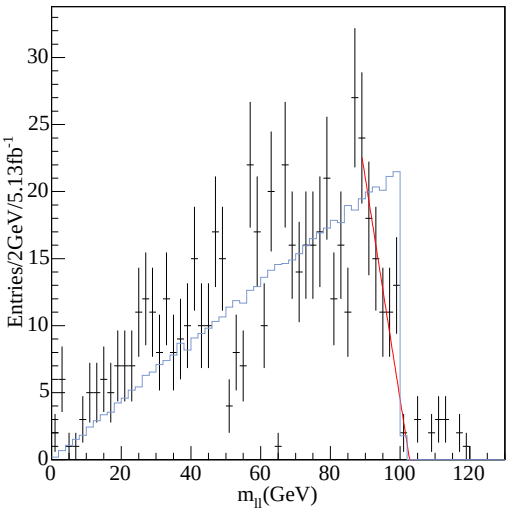

Figure 5.9: Invariant mass distribution of the two final leptons (points with error bars) together with the theoretical prediction (light curve).

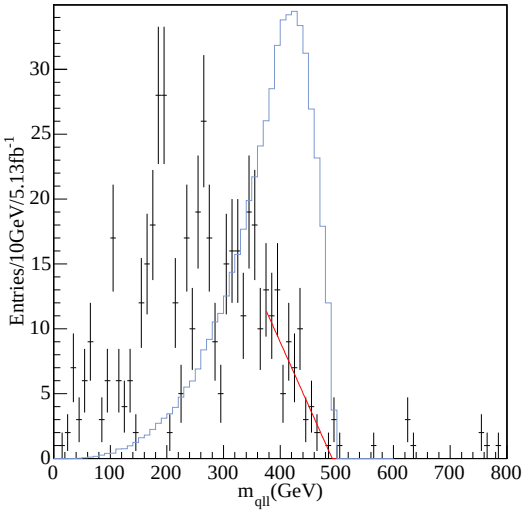

Figure 5.10: Invariant mass distributions of the two final leptons and a quark (points with error bars) together with the theoretical prediction (light curve).

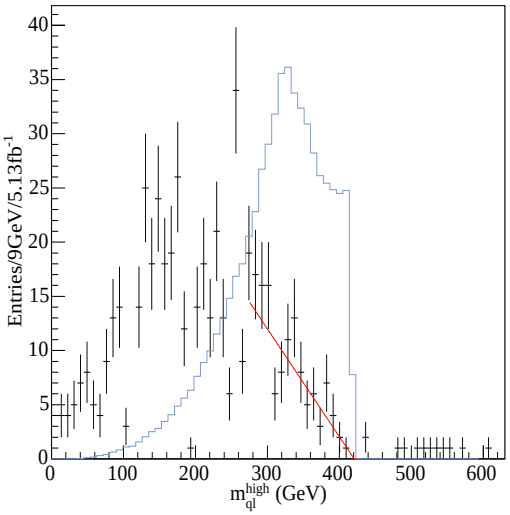

Figure 5.11: Invariant mass distribution of lepton and quark, the combination that gives the largest mass (points with error bars) together with the theoretical prediction (light curve).

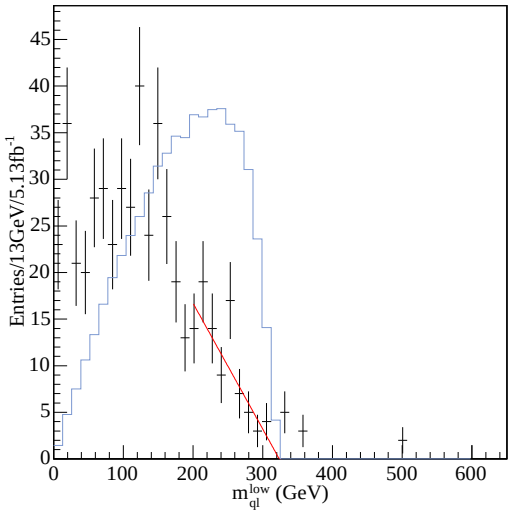

Figure 5.12: Invariant mass distribution of lepton and quark, the combination that gives the smallest mass (points with error bars) together with the theoretical prediction (light curve).

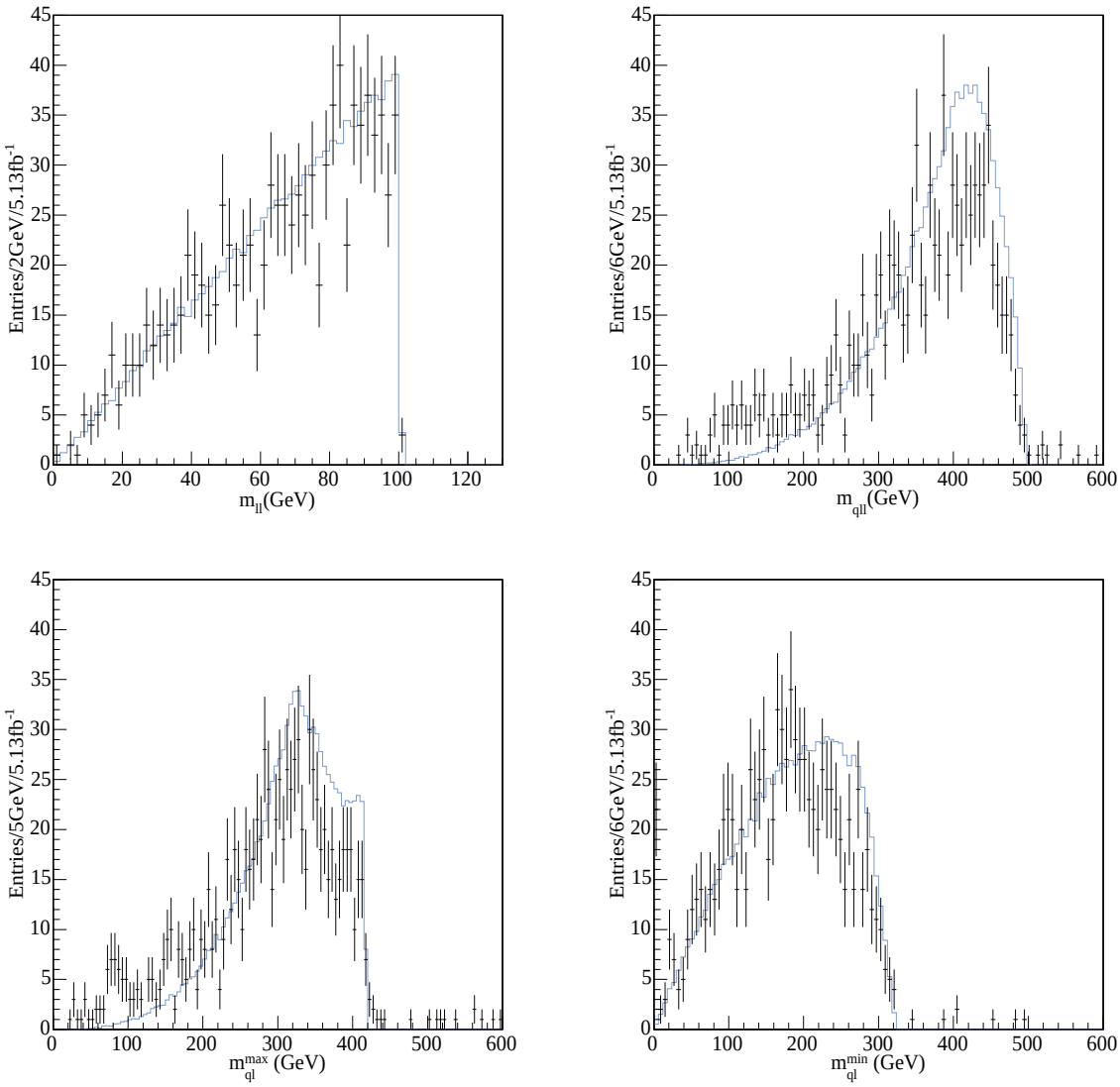

Figure 5.13: Invariant mass distributions from generated particles (points with error bars) together with theoretical predictions (histograms)

Table (5.3) summarizes the endpoint measurements, and lists the mean values together with the corresponding nominal value. By inspection it becomes apparent that the statistical errors do not account for the variation within the measured endpoints. The discrepancy itself is therefore interpreted as a systematic error and added to the table. Systematic errors at ATLAS, are believed to be reduced far below the statistical ones, at least when the detector is properly understood and calibrated [6]. The values listed in table (5.3) are all larger than the statistical errors, and therefore not representative.

Straight lines have been used to fit the edges of various invariant mass distributions. This is a simple, but not necessarily good approach. In all theoretical distributions, except m_{ll}, the straight line approximation is not optimal, especially if the line is drawn from the maximum of the curve, see figure (5.13).

In simulated distributions with low statistics it is usually unclear where the edge

	Endpoint values (GeV)						
Endpoint	Nominal	Fast			Full		
		$\langle m \rangle$	Statistical Error	Systematic Error	$\langle m \rangle$	Statistical Error	Systematic Error
$(m_{ll})^{max}$	100.2	102.4	0.6	3.5	103.2	0.7	3.4
$(m_{qll})^{max}$	498.9	500.5	5.4	5.0	501.4	5.4	6.7
$(m_{ll}^{high})^{max}$	416.4	432.6	9.4	49.1	420.9	5.4	16.5
$(m_{ll}^{low})^{max}$	323.4	322.7	4.9	14.1	322.2	6.0	12.4

Table 5.3: Nominal and experimental endpoint values

is, making the endpoint measurement even more uncertain. An example is the m_{ql}^{high}-distribution in figure (5.7). Here is the theoretical edge a vertical line. Some simulated points are actually close to the this edge, but they are not by far many enough to uncover its steepness. The result is that the points used for the linear fit do not belong to the edge. Which again, causes huge variations in the values obtained when the fit parameters are changed and is the reason for the discrepancy accounted for by the systematic errors in table (5.3).

5.4 Determination of sparticle masses

We are now ready to use the measured endpoints in table (5.3) as input in the six set of formulae in appendix B, section B.2, and obtain values for the sparticle masses. The masses resulting from these calculations[4] are listed in table (5.4).

	Solution 1 (GeV)			Solution 2 (GeV)		
Mass	Nominal	Fast	Full	Nominal	Fast	Full
$m_{\tilde{\chi}_0^1}$	356.45	242.5±116	365.4±163	117.91	86.7±44	128.0±65
$m_{\tilde{l}_R}$	420.10	310.7±114	432.0±161	155.42	121.5±45	165.7±63
$m_{\tilde{\chi}_0^2}$	460.77	351.2±114	473.3±160	218.61	190.1±41	232.1±60
$m_{\tilde{q}_L}$	912.24	775.9±123	919.8±153	631.51	593.7±54	644.4±77

Table 5.4: The two possible solutions of sparticle masses obtained from fast and full simulation measurements including mass widths.

Solution 1 and solution 2 in the table corresponds to mass relation regions (1,1) and (1,3) with respect to the equations given in section B.1. Nominal masses are provided by ISASUSY.

Two comments need to be made about the results. Firstly, the set of measured endpoints satisfy two solutions for the sparticle masses, but multiple solutions are common, as mentioned in section 5.2. The challenge is, however, to see if there is any method available that can help us choose one solution at the other's expense. Knowing the input of our simulation program we recognize solution 2 to be correct. At the LHC the input is unknown, and we need to discriminate between the two solutions by other means. This problem will be addressed further in subsection 5.4.1.

Secondly, the results from fast simulation are not similar to the results from full

[4]The masses and errors are calculated by a program written by B.K. Gjelsten, co-author of [6]

simulation. Ideally the results should be somewhat alike since the main difference between them is only caused by the way detector simulation performs. From table (5.4) we see that this is not the case, the masses from fast simulation data are smaller than the corresponding masses from full simulation. The latter results are also closer to the nominal values for both solutions. For solution 1 the masses measured by full simulation data are on average 10 GeV larger than nominal values, while the fast simulation results are 110 GeV lower. Solution 2 gives a somewhat better result, full and fast simulation endpoints give masses that are on average 11 GeV above and 33 GeV below nominal values, respectively.

The difference between the masses obtained from fast and full simulation data can only be caused by differences in the measured endpoints. As we saw in table (5.3) the only endpoint measurement that differs significantly is m_{ql}^{high}. The value from fast simulation is 12 GeV larger than the value from full simulation, inferring that masses are very sensitive to endpoint values.

A way of knowing whether the masses from the two simulations actually disagree with each other is to estimate the mass width or error. For this purpose the method of 10 000 ATLAS experiments [6] is used. The method smears the statistical error with a Gaussian distribution of mean 0 and variance 1 and adds it to the measured endpoint. The new endpoint value is then used for mass calculations. By repeating the procedure 10 000 times we obtain one distribution for each mass. It is the width of these distributions that are listed as errors in table (5.4). The table shows that mass widths are huge. This reflects the uncertainties in endpoint measurements. However, within the rather large errors the masses obtained from both simulations are compatible.

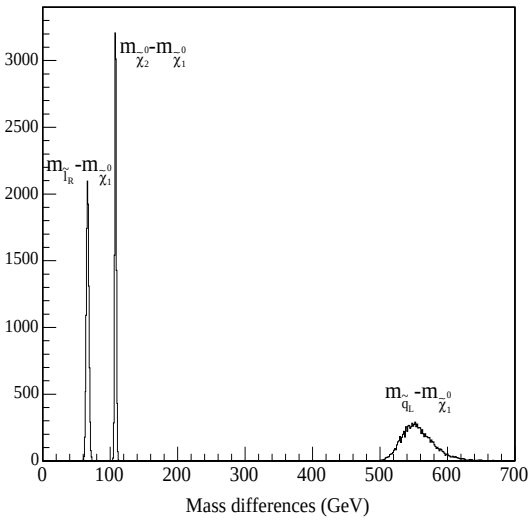

Figure 5.14: Mass difference distributions for solution 1, from full simulation endpoints

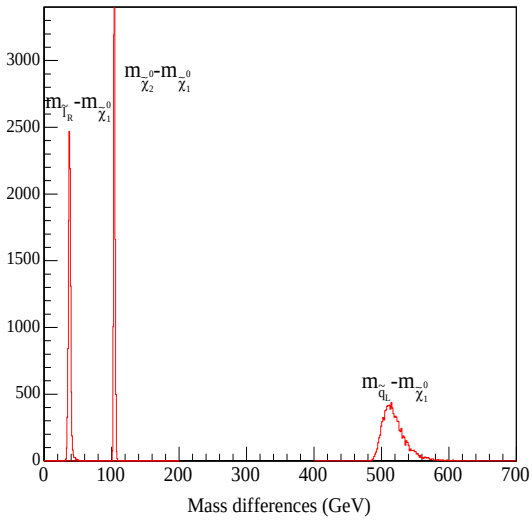

Figure 5.15: Mass difference distributions for solution 2, from full simulation endpoints

The large errors in table (5.4) rise the question whether the investigations presented in this section were worthwhile. According to [6] the sparticle masses have a strong positive correlation. Mass differences are therefore expected to be more accurate than direct mass measurements at the LHC. This is indeed the case as seen in table (5.5). Especially the lightest sparticle masses are strongly correlated and the differences between

	Solution 1 (GeV)					Solution 2 (GeV)				
	Nom.	Full		Fast		Nom.	Full		Fast	
	$\langle m \rangle$	$\langle m \rangle$	σ	$\langle m \rangle$	σ	$\langle m \rangle$	$\langle m \rangle$	σ	$\langle m \rangle$	σ
$m_{\tilde{l}_R}$ -$m_{\tilde{\chi}_0^1}$	63.7	66.7	1.9	68.3	2.4	37.5	37.9	1.9	34.9	2.6
$m_{\tilde{\chi}_0^2}$-$m_{\tilde{\chi}_0^1}$	104.3	108.0	1.1	108.8	1.8	100.7	104.3	1.0	103.5	1.0
$m_{\tilde{q}_L}$ -$m_{\tilde{\chi}_0^1}$	555.8	557.5	25.0	536.5	21.8	513.6	519.9	18.9	509.7	13.2

Table 5.5: Mass differences with errors for full and fast simulations

them are small, as seen both from the table and figures (5.14) and (5.15). The nominal and measured values are much closer than they were for direct mass measurements and the errors are significantly smaller for both solutions and detector simulations. In addition there is a good agreement between full and fast measurements.

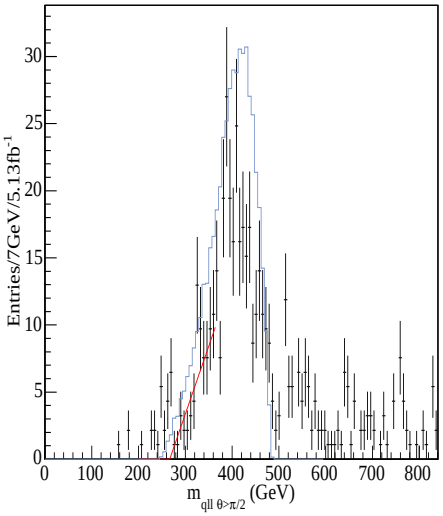

Figure 5.16: Distribution of $m^{min}_{qll(\theta>\pi/2)}$ with fast simulation data (error bar curve) together with the theoretical distribution (continuous curve)

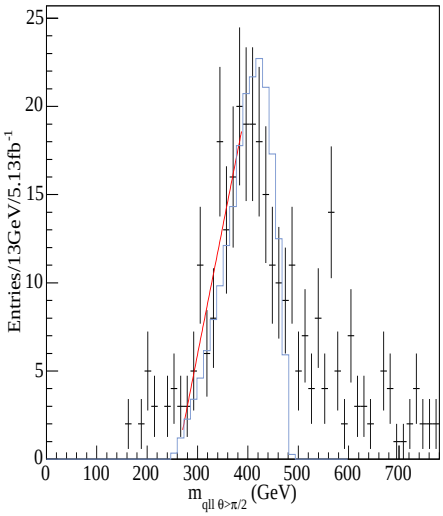

Figure 5.17: Distribution of $m^{min}_{qll(\theta>\pi/2)}$ with full simulation data (error bar curve) together with the theoretical distribution (continuous curve)

5.4.1 $m_{qll(\theta>\pi/2)}$-distribution

As an attempt to discriminate between the two solutions in table (5.4) a fifth invariant mass distribution can be made. The mass distribution $m_{qll(\theta>\pi/2)}$ is defined by requiring

$$m_{ll}^{max}/\sqrt{2} < m_{ll} < m_{ll}^{max} \tag{5.10}$$

for the ordinary m_{qll} distribution [6], and referred to as the threshold distribution. The requirement on m_{ll} is actually a requirement on the angle θ between the two final leptons in the rest frame of $\tilde{l}_R$ [6]. Constraint (5.10) on m_{ll} corresponds directly to

	Solution 1 (GeV)		Solution 2 (GeV)	
	m	σ	m	σ
Fast	218.8	4.4	259.2	12.4
Full	214.8	4.1	247.3	12.0

Table 5.6: Calculated minima of $m_{qll(\theta>\pi/2)}$ from masses obtained from fast and full simulation data.

$m^{min}_{qll(\theta>\pi/2)}$				
n	Fast(GeV)		Full (GeV)	
	Endpoint	Error	Endpoint	Error
1	272.5	8.4	227.6	12.1
2	266.8	8.0	228.4	12.7
3	257.8	8.8	246.4	12.9
4	275.9	8.5	240.0	13.2
5	282.1	8.1	249.9	12.1
6	268.5	8.3	260.7	11.1
7	284.1	8.6	259.1	12.6
Mean	272.5	8.4	244.6	12.5

Table 5.7: Results from straight line fits of threshold-curve

$\theta > \pi/2$, as equation (5.11) shows.

$$m_{ll} = m_{ll}^{max}\sqrt{(1-\cos\theta)/2} \tag{5.11}$$

According to [6] the simplicity of this constraint makes it possible to find an analytic expression for the minimum of the threshold distribution. This minimum provides one more measurement. The analytic expression of the minimum is:

$$\begin{aligned}\left(m^{\min}_{qll(\theta>\frac{\pi}{2})}\right)^2 \;=\; & \Big[\left(m^2_{\tilde{q}_L}+m^2_{\tilde{\chi}^0_2}\right)\left(m^2_{\tilde{\chi}^0_2}-m^2_{\tilde{l}_R}\right)\left(m^2_{\tilde{l}_R}-m^2_{\tilde{\chi}^0_1}\right) \\ & -\left(m^2_{\tilde{q}_L}-m^2_{\tilde{\chi}^0_2}\right)\sqrt{\left(m^2_{\tilde{\chi}^0_2}+m^2_{\tilde{l}_R}\right)^2\left(m^2_{\tilde{l}_R}+m^2_{\tilde{\chi}^0_1}\right)^2-16m^2_{\tilde{\chi}^0_2}m^4_{\tilde{l}_R}m^2_{\tilde{\chi}^0_1}} \\ & +2m^2_{\tilde{l}_R}\left(m^2_{\tilde{q}_L}-m^2_{\tilde{\chi}^0_2}\right)\left(m^2_{\tilde{\chi}^0_2}-m^2_{\tilde{\chi}^0_1}\right)\Big]/\left(4m^2_{\tilde{l}_R}m^2_{\tilde{\chi}^0_2}\right).\end{aligned} \tag{5.12}$$

Equation (5.12) depends solely on the four masses already calculated. Values of $m^{min}_{qll(\theta>\pi/2)}$ are then obtainable, by using the masses in table (5.4) as input in equation (5.12). Four values for the minimum of the threshold distribution are obtained; two from fast, and two from full simulation results, see table (5.6). Estimation of errors are done by using the method of 10 000 ATLAS experiments, as mentioned earlier.

Surprisingly the errors listed in table (5.6) are much smaller than the mass errors. This is very fortunate since larger errors would have made the two solutions compatible with each other. There was unfortunately not enough time to investigate the reason for the small errors.

The values in table (5.6) indicate where the minimum of the threshold- distribution should be in the two solutions. A measurement of the minima in both fast and full simulation distributions, figures (5.16) and (5.17) respectively, will hopefully determine which solution to choose. The minima were measured with a straight line fit and measurements chosen using criteria (5.8), the resulting values are listed in table (5.7).

The mean value of the fast simulation measurements is 272.5 ± 8.4 GeV, while the corresponding value for full simulation is 244.6 ± 12.5. The spread in the measurements is quite large, roughly 30 GeV for both simulations. The reason for this becomes apparent when figures (5.16) and (5.17) are studied. Both figures show that the minima are polluted by background, which causes variation in the values measured. Also note that the shape of the simulated distributions show a remarkable similarity to the theoretical.

	Measured (GeV)	Calculated (GeV)	
		Solution 1	Solution 2
Fast	272.5 ± 8.4	218.8 ± 4.4	259.2 ± 12.4
Full	244.6 ± 12.5	214.8 ± 4.1	247.3 ± 12.0

Table 5.8: Calculated and measured values for the minimum of the threshold curve

Table (5.8) summarizes the results of this section. Comparison between calculated and measured values favours solution 2, which actually is the nominal solution.

5.5 Conclusion

We have reached our goal and determined the masses of the sparticles in the cascade decay chain. By measuring the endpoints of four invariant mass distributions, for both fast and full simulation data, we obtained two solutions for four unknown sparticle masses. We made an additional measurement in order to discriminate between the solutions. The obtained results favoured solution 2 instead of solution 1. One solution cannot always be favoured, and must sometimes be determined by other measurements, for instance cross sections.

The above-mentioned method has its deficiencies. Among them is the fact that only one 'experiment' is performed. The mean values of the endpoints, which are used for mass calculation, do not come from several independent measurements, but from strongly correlated results. Mass values are therefore obtained from one single measurement. The method for calculating mass widths or errors, however, is regarded more realistic since their estimation required 10 000 ATLAS 'experiments'. Also the straight line fitting procedure, that do not contain any background assumptions, calls for improvement.

Also note that the proper way of extracting masses from endpoints would be to include all five invariant mass distributions from the beginning. Then the system has five equations and four unknowns, and becomes over-constrained. A more sophisticated approach is then needed to find the correct solution. One way would be to use numerical fits as described in [6].

We did also compare the results from fast and full simulation data. We observed that the data from full simulation give the best result with respect to nominal mass values, while fast simulation results give the smallest width.

Both sets of measurements have huge errors leaving the actual value of the sparticle masses uncertain. It is however important to remember that the data corresponds to only six months of running at the LHC. More statistics would improve the results and allow the study of systematic errors. By applying similar methods to other decays, further constraints on the masses could be achieved. Development of new fitting techniques and tuning of cuts to enlarge the signal to background ratio could also improve

the measurements.

The difference between fast and full simulation results are accounted for through the large errors in the measurements. Fast simulation results were systematically below nominal values, while the opposite was the case for full simulation results. The statistical material in this thesis is too small to draw any general conclusion about the observed differences in results between the two detector simulations. As long as the difference lies within statistical uncertainties it is not possible to tell whether the detector simulation has any influence on the result.

The investigations in this last chapter also showed that the sparticle masses are very sensitive to the endpoint values. The fast m_{ql}^{high}-endpoint were 2% larger than the full simulation value, causing masses obtained from the former measurements to be 29% smaller than the corresponding masses of the latter. The difference in the m_{ql}^{high}-endpoint is not the single cause of the dissimilarities in masses. If the value of the fast m_{ql}^{high}-endpoint is changed to the value of the full m_{ql}^{high}-endpoint, leaving the other endpoints unchanged, there is still an average difference of 4% between the calculated masses. This difference is then due to the very small dissimilarity between the remaining endpoints.

By measuring the difference between sparticle masses a more optimistic result was obtained. The discrepancy between nominal and measured values amounted to a few percent and the errors are small compared to direct measurements of the masses. The LHC will be more suitable for measurements of mass differences than direct mass measurements, this is also in agreement with previous studies [6]. A Linear Collider will be able to fix the mass of the LSP at nominal value. By combining this measurement with measurements of mass differences, the mass of the remaining sparticles can be determined.

Time did not allow for attempts to reduce the errors in the mass measurements, nor for a rigorous study of systematic errors. Among the details that should have been resolved are the reasons for the polluted endpoint of the m_{ql}^{high}-distribution.

Bibliography

[1] ATLAS Collaboration, ATLAS Technical Design Report, CERN (1999)

[2] Biglietti et al. Full Supersymmetry Simulation for ATLAS in DC1, ATL-PHYS-2004-011, (2004)

[3] B.R.Martin, G.Shaw, Particle Physics, John Wiley & Sons, Chichester (1997)

[4] T. Sjostrand, L. Lonneblad, S.Mrenna, P. Skands, Pythia 6.2 Physics and Manual (second edition),hep-ph/0108264, (2002)

[5] I.Hinchcliff, F.E.Paige, M.D.Shapiro, J.Soderquist, W.Yao, *Physical Review* D55 (1997) 5520 9

[6] B.K. Gjelsten, D.J. Miller, P. Osland, Measurement of SUSY Masses via Cascade Decays for SPS 1a, JHEP 0412 (2004) 003

[7] E.Lytken, Prospects for Slepton Searches with ATLAS, PhD Thesis at the Niels Bohr Institute, 2003.

[8] ATLAS Collaboration, Liquid Argon Technical Design Report, CERN (1996)

[9] S. Eidelman et al., Phys. Lett. B 592, 1 (2004)

[10] G, Azuelos et al., Jet Finder Library: version 1.0, ATLAS Internal Note ATL-SOFT-98-038

[11] R.K. Bock, A. Vasilescu, The Particle Detector BriefBook (The Internet version), http://rkb.home.cern.ch/rkb/titleD.html

[12] ATLAS Software Working Group, CBNT_Athena Ntuple variable list, (http://atlas.web.cern.ch/Atlas/GROUPS/SOFTWARE/OO/domains /Reconstruction/packages/CBNT_Athena/CBNT_variables.htm)

[13] B.C. Allanach, C.G. Lester, M.A. Parker, and B.R. Webber, Measuring sparticle masses in non-universal string inspired models at the LHC, JHEP09(2000)004.

[14] http://phyweb.lbl.gov/susy/

[15] M.Dobbs,S.Frixione, E. Laenen, K. Tollefson, Les Houches Guidebook to MOnte Carlo Generators for Hadron Collider Physics, hep-ph/0403045,2004.

[16] M. Dobbs, J.B. Hansen, The HepMC C++ Monte Carlo event record for High Energy Physics, Computer Physics Communications 134,41(2001):

[17] G. Corcella, I.G. Knowles, G. Marchesini, S. Moretti, K. Odagiri, P. Richardson, M.H. Seymour and B.R. Webber, HERWIG 6.5, JHEP 0101 (2001) 010 [hep-ph/0011363]; hep-ph/0210213.

[18] H. Baer, F.Page, S. Protopopescu, X. Tata, ISAJET.7.48 A Monte Carlo Event Generator for pp, $p\bar{p}$ and e^+e^- Reactions, hep-ph/0001086, (2000).

[19] http://www.hep.phy.cam.ac.uk/ richardn/HERWIG/ISAWIG/

[20] P. Richardson, Simulating Exotic Processes, Talk at Exotic Signal at Hadron Colliders, Durham (2003).

[21] B. Andersson, G. Gustafson, G. Ingelman and T. Sjöstrand, Parton fragmenttion and string dynamics, Physics Report 97(1983)31.

[22] M. Drees, S.P. Martin, Electroweak symmetry breaking and new physics at the TeV scale, eds. T.L. Barklow et al., p.146, hep-ph/9504324.

[23] D.M. Pierce, J.A. Bagger, K. Matchev and R. Zhang Nucl. Phys B491(1997)3

[24] A. Dell'Acqua, A hands on introduction to Geant4, Talk given at the Ann Arbor Workshop on Geant4 (2001) http://atlas.web.cern.ch/Atlas/GROUPS/SOFTWARE/OO/sit/Training/

[25] Application Software Group, GEANT-Detector Description and Simulation Tool, CERN, Geneva 1993

[26] Jakob. L. Nielsen, Using the NorduGrid Atlas rpms, Seminar at the University of Oslo, 2003.

[27] E. Richter-Was, d. Froidevaux, L. Poggioli, ATLFAST 2.0 a fast simulation package for ATLAS, ATL-PHYS-98-131.

[28] Wim T.L.P. Lavrijsen, Python for ATLAS Software, US-ATLAS Physics Analysis 2004.

[29] R. Brun et al. The ROOT project, http://root.cern.ch/

[30] CERN computer center, The PAW manual, CERN Program Library Entry Q121 (1989)

[31] http://atlas.web.cern.ch/Atlas/GROUPS/SOFTWARE/OO/architecture/

[32] http://atlantis.web.cern.ch/atlantis/

[33] K. Desch, Supersymmetry at LHC and ILC, Proceedings of the SLAC Summer Institute 2004.

[34] Super-Kamiokande Collaboration, EVIDENCE FOR AN OSCILLATORY SIGNATURE IN ATMOSPHERIC NEUTRINO OSCILLATION, Phys.Rev.Lett.93:101801,2004.

[35] J. Ellis, Supersymmetry for Alp Hikers hep-ph/0203114.

[36] S. P. Martin, A Supersymmetry Primer, hep-ph/9709356

[37] K.R.Dienes, String Theory and the Path to Unification: A Review of Recent Developments, Pyisics Report 287, 447-525 (1997) hep-th/9602045

[38] R.M. Godbole, Challenges of LHC to QCD and vice versa. Talk given in Beijing, July 6-10 (2004).

[39] G. Sguazzoni, Higgs and beyound Standard Model searches at LEP, hep-ph/0411096.

[40] A.J. Barr, Studies of supersymmetry models for the ATLAS experiment at the Large Hadron Collider, Phd. thesis University of Cambridge (2002)

[41] Wikipedia, free online encyclopedia, (http://en.wikipedia.org/wiki/Main_Page)

[42] http://ist-socrates.berkeley.edu/ noise/mssm.html

[1] N. Arkani-Hamed, S. Dimopoulos, Supersymmetric Unification without low energy Supersymmetry andsignatures for fine-tuning at the LHC. (hep-th/0405159)

[43] W.R. Leo, Techniques for Nuclear and Particle Physics Experiments 2nd edition, Springer-Verlag (1994)

[44] C. G. Lester, Model independent sparticle mass measurements at ATLAS, PhD thesis University of Cambridge 2001.

Appendix A

Obtaining the photon field

The free Lagrangian for an electron is given by

$$\mathscr{L} = i\bar{\psi}\gamma_\mu\partial^\mu\psi - m\bar{\psi}\psi \tag{A.1}$$

By inspection we find that equation A.1 remains unchanged under the following phase transformation of the field

$$\psi(x) \to e^{i\alpha}\psi(x) \tag{A.2}$$

where α is a real constant.

The family of phase transformations $U(\alpha) \equiv e^{i\alpha}$ forms a unitary Abelian[1] group called U(1).

Equation A.2 is called a global gauge transformation, and we say that the Lagrangian in A.1 is gauge invariant. The transformation is global since the parameter α stays the same throughout space.

According to Noether's theorem gauge invariance of A.1 implies the existence of a conserved current. By working out the details the current is found to be the electromagnetic charge current density. This leads again to the conservation of electric charge. Both results are obtained only because of the U(1) phase invariance of the free electron Lagrangian.

A more general invariance of A.1 would be if α could differ throughout space, that is, $\alpha = \alpha(x)$. The Lagrangian should then be invariant under transformation

$$\psi(x) \to e^{i\alpha(x)}\psi(x) \tag{A.3}$$

where $\alpha(x)$ depends on space and time. This is known as local gauge invariance. This is however not the case, the free electron Lagrangian is not invariant under the A.3.

By introducing a modified derivative local gauge invariance can be imposed on A.1. The motivation for doing this is purely mathematical aesthetics. It turns out that

$$D_\mu \equiv \partial_\mu - ieA_\mu \tag{A.4}$$

where A_μ transforms as

$$A_\mu \to A_\mu + \frac{1}{e}\partial_\mu\alpha \tag{A.5}$$

cancel the unwanted terms in A.1 when ψ undergo transformation A.3. Finally we can reformulate the Lagrangian in equation A.1 by replacing the derivative by the modified derivative in A.4, the Lagrangian becomes:

$$\mathscr{L} = \bar{\psi}(i\gamma_\mu\partial^\mu - m)\psi + e\bar{\psi}\gamma_\mu A_\mu\psi - \frac{1}{4}F_{\mu\nu}F^{\mu\nu} \tag{A.6}$$

[1] Multiplication of group members is commutative. This is not necessarily the case for groups

and is called the QED Lagrangian.

The end of the story is that if we impose local gauge invariance on a free electron Lagrangian we are forced to introduce a vector field A_μ that couples to the Dirac particle. A_μ is called the gauge field and is interpreted as the physical photon field.

Exactly the same procedure can be used on the quarks but we need to replace the U(1) gauge group by the SU(3) group of phase transformations on the quark color fields. SU(3) is a non-Abelian group which slightly complicates the deduction.

Appendix B

Mass formulae

All formulae in this appendix are obtained from [6] with permission from B.K. Gjelsten.

B.1 Endpoint formulae

Formulae connecting endpoints of invariant masses to sparticle masses. Note that only the endpoint of the invariant mass distribution of the two final leptons m_{ll} have a unique expression. The other relations depend on the mass relations and ratios, see B.3 and B.2 respectively.

$$(m_{ll}^{\max})^2 = \left(m_{\tilde{\chi}_2^0}^2 - m_{\tilde{l}_R}^2\right)\left(m_{\tilde{l}_R}^2 - m_{\tilde{\chi}_1^0}^2\right)/m_{\tilde{l}_R}^2 \tag{B.1}$$

$$\left(m_{qll}^{\max}\right)^2 = \begin{cases} \frac{\left(m_{\tilde{q}_L}^2 - m_{\tilde{\chi}_2^0}^2\right)\left(m_{\tilde{\chi}_2^0}^2 - m_{\tilde{\chi}_1^0}^2\right)}{m_{\tilde{\chi}_2^0}^2} & \text{for} \quad \frac{m_{\tilde{q}_L}}{m_{\tilde{\chi}_2^0}} > \frac{m_{\tilde{\chi}_2^0}}{m_{\tilde{l}_R}}\frac{m_{\tilde{l}_R}}{m_{\tilde{\chi}_1^0}} \quad (1) \\ \frac{\left(m_{\tilde{q}_L}^2 m_{\tilde{l}_R}^2 - m_{\tilde{\chi}_2^0}^2 m_{\tilde{\chi}_1^0}^2\right)\left(m_{\tilde{\chi}_2^0}^2 - m_{\tilde{l}_R}^2\right)}{m_{\tilde{\chi}_2^0}^2 m_{\tilde{l}_R}^2} & \text{for} \quad \frac{m_{\tilde{\chi}_2^0}}{m_{\tilde{l}_R}} > \frac{m_{\tilde{l}_R}}{m_{\tilde{\chi}_1^0}}\frac{m_{\tilde{q}_L}}{m_{\tilde{\chi}_2^0}} \quad (2) \\ \frac{\left(m_{\tilde{q}_L}^2 - m_{\tilde{l}_R}^2\right)\left(m_{\tilde{l}_R}^2 - m_{\tilde{\chi}_1^0}^2\right)}{m_{\tilde{l}_R}^2} & \text{for} \quad \frac{m_{\tilde{l}_R}}{m_{\tilde{\chi}_1^0}} > \frac{m_{\tilde{q}_L}}{m_{\tilde{\chi}_2^0}}\frac{m_{\tilde{\chi}_2^0}}{m_{\tilde{l}_R}} \quad (3) \\ \left(m_{\tilde{q}_L} - m_{\tilde{\chi}_1^0}\right)^2 & \text{otherwise} \quad (4) \end{cases} \tag{B.2}$$

$$\left(m_{ql(\text{low})}^{\max}, m_{ql(\text{high})}^{\max}\right) = \begin{cases} \left(m_{ql_{\text{n}}}^{\max}, m_{ql_{\text{f}}}^{\max}\right) & \text{for} \quad 2m_{\tilde{l}_R}^2 > m_{\tilde{\chi}_1^0}^2 + m_{\tilde{\chi}_2^0}^2 > 2m_{\tilde{\chi}_1^0}m_{\tilde{\chi}_2^0} \quad (1) \\ \left(m_{ql(\text{eq})}^{\max}, m_{ql_{\text{f}}}^{\max}\right) & \text{for} \quad m_{\tilde{\chi}_1^0}^2 + m_{\tilde{\chi}_2^0}^2 > 2m_{\tilde{l}_R}^2 > 2m_{\tilde{\chi}_1^0}m_{\tilde{\chi}_2^0} \quad (2) \\ \left(m_{ql(\text{eq})}^{\max}, m_{ql_{\text{n}}}^{\max}\right) & \text{for} \quad m_{\tilde{\chi}_1^0}^2 + m_{\tilde{\chi}_2^0}^2 > 2m_{\tilde{\chi}_1^0}m_{\tilde{\chi}_2^0} > 2m_{\tilde{l}_R}^2 \quad (3) \end{cases}$$

(B.3)

$$\left(m_{ql_{\rm n}}^{\rm max}\right)^2 = \left(m_{\tilde{q}_L}^2 - m_{\tilde{\chi}_2^0}^2\right)\left(m_{\tilde{\chi}_2^0}^2 - m_{\tilde{l}_R}^2\right)/m_{\tilde{\chi}_2^0}^2 \quad \text{(B.4)}$$

$$\left(m_{ql_{\rm f}}^{\rm max}\right)^2 = \left(m_{\tilde{q}_L}^2 - m_{\tilde{\chi}_2^0}^2\right)\left(m_{\tilde{l}_R}^2 - m_{\tilde{\chi}_1^0}^2\right)/m_{\tilde{l}_R}^2 \quad \text{(B.5)}$$

$$\left(m_{ql(\rm eq)}^{\rm max}\right)^2 = \left(m_{\tilde{q}_L}^2 - m_{\tilde{\chi}_2^0}^2\right)\left(m_{\tilde{l}_R}^2 - m_{\tilde{\chi}_1^0}^2\right)/\left(2m_{\tilde{l}_R}^2 - m_{\tilde{\chi}_1^0}^2\right) \quad \text{(B.6)}$$

$$\begin{aligned}\left(m_{qll(\theta>\frac{\pi}{2})}^{\rm min}\right)^2 = \Big[&\left(m_{\tilde{q}_L}^2 + m_{\tilde{\chi}_2^0}^2\right)\left(m_{\tilde{\chi}_2^0}^2 - m_{\tilde{l}_R}^2\right)\left(m_{\tilde{l}_R}^2 - m_{\tilde{\chi}_1^0}^2\right) \\ &-\left(m_{\tilde{q}_L}^2 - m_{\tilde{\chi}_2^0}^2\right)\sqrt{\left(m_{\tilde{\chi}_2^0}^2 + m_{\tilde{l}_R}^2\right)^2\left(m_{\tilde{l}_R}^2 + m_{\tilde{\chi}_1^0}^2\right)^2 - 16m_{\tilde{\chi}_2^0}^2 m_{\tilde{l}_R}^4 m_{\tilde{\chi}_1^0}^2} \\ &+2m_{\tilde{l}_R}^2\left(m_{\tilde{q}_L}^2 - m_{\tilde{\chi}_2^0}^2\right)\left(m_{\tilde{\chi}_2^0}^2 - m_{\tilde{\chi}_1^0}^2\right)\Big]/\left(4m_{\tilde{l}_R}^2 m_{\tilde{\chi}_2^0}^2\right) \quad \text{(B.7)}\end{aligned}$$

where 'low' and 'high' on the left-hand side in Eq. (B.3) refer to minimising and maximising with respect to the choice of lepton. Furthermore 'min' in Eq. (B.7) refers to the threshold in the subset of the m_{qll} distribution for which $\frac{m_{ll}}{\sqrt{2}} < (m_{ll})^{max} < m_{ll}$.

B.2 Inversion formulae

The formulae below are the inverted equations of section B.1. The endpoint expressions in the last section were not unique, neither are the sparticle mass expressions, which depends on the relations between the masses. The mass solutions are divided into regions called Region(a,b), where a refers to the number labeling the mass ratios in equation B.2 and b refers to the number labelling the mass relations in equation B.3. This means that the solutions in Region(1,1) satisfy the mass ratio (1) of equation B.2 and the mass relation (1) of equation B.3.

$$a = m_{ll}^{\rm max},\ b = m_{qll}^{\rm max},\ c = m_{ql(\rm low)}^{\rm max},\ d = m_{ql(\rm high)}^{\rm max}. \quad \text{(B.8)}$$

Region (1,1):

$$m_{\tilde{\chi}_1^0}^2 = \frac{(b^2-d^2)(b^2-c^2)}{(c^2+d^2-b^2)^2}a^2 \quad \text{(B.9)}$$

$$m_{\tilde{l}_R}^2 = \frac{c^2(b^2-c^2)}{(c^2+d^2-b^2)^2}a^2 \quad \text{(B.10)}$$

$$m_{\tilde{\chi}_2^0}^2 = \frac{c^2d^2}{(c^2+d^2-b^2)^2}a^2 \quad \text{(B.11)}$$

$$m_{\tilde{q}_L}^2 = \frac{c^2d^2}{(c^2+d^2-b^2)^2}(c^2+d^2-b^2+a^2) \quad \text{(B.12)}$$

Region (1,2):

$$m^2_{\tilde{\chi}^0_1} = \frac{(b^2c^2 - b^2d^2 + c^2d^2)(2c^2 - d^2)}{(d^2 - c^2)^2(b^2 - d^2)}a^2 \quad \text{(B.13)}$$

$$m^2_{\tilde{l}_R} = \frac{(b^2c^2 - b^2d^2 + c^2d^2)c^2}{(d^2 - c^2)^2(b^2 - d^2)}a^2 \quad \text{(B.14)}$$

$$m^2_{\tilde{\chi}^0_2} = \frac{(2c^2 - d^2)c^2d^2}{(d^2 - c^2)^2(b^2 - d^2)}a^2 \quad \text{(B.15)}$$

$$m^2_{\tilde{q}_L} = \frac{c^2d^2}{(d^2 - c^2)^2(b^2 - d^2)}[a^2(2c^2 - d^2) + (d^2 - c^2)(b^2 - d^2)] \quad \text{(B.16)}$$

Region (1,3):

$$m^2_{\tilde{\chi}^0_1} = \frac{(d^2 - c^2)(b^2 - d^2)(b^2 - 2c^2)}{(c^2 + d^2 - b^2)^2d^2}a^2 \quad \text{(B.17)}$$

$$m^2_{\tilde{l}_R} = \frac{(d^2 - c^2)^2(b^2 - d^2)}{(c^2 + d^2 - b^2)^2d^2}a^2 \quad \text{(B.18)}$$

$$m^2_{\tilde{\chi}^0_2} = \frac{(2d^2 - b^2)(d^2 - c^2)c^2}{(c^2 + d^2 - b^2)^2d^2}a^2 \quad \text{(B.19)}$$

$$m^2_{\tilde{q}_L} = \frac{(2d^2 - b^2)c^2}{(c^2 + d^2 - b^2)^2d^2}[a^2(d^2 - c^2) + d^2(c^2 + d^2 - b^2)] \quad \text{(B.20)}$$

Region (4,1):

$$m^2_{\tilde{\chi}^0_1} = m^2_{\tilde{\chi}^0_2} - (da/c + ac/d)m_{\tilde{\chi}^0_2} + a^2 \quad \text{(B.21)}$$

$$m^2_{\tilde{l}_R} = m^2_{\tilde{\chi}^0_2} - (ac/d)m_{\tilde{\chi}^0_2} \quad \text{(B.22)}$$

$$m_{\tilde{\chi}^0_2} = \frac{\left[(a^2 + b^2)c^2d^2 - (b^2 - a^2)a^2(c^2 + d^2) + 2abcd\sqrt{(a^2 + c^2 - b^2)(a^2 + d^2 - b^2)}\right]}{[(a^2c^2 + a^2d^2 + c^2d^2)^2 - 4a^2b^2c^2d^2]/(acd)} \quad \text{(B.23)}$$

$$m_{\tilde{q}_L} = m_{\tilde{\chi}^0_1} + b \quad \text{(B.24)}$$

Region (4,2):

$$m_{\tilde{\chi}^0_1} = \frac{2c^2 - d^2}{d^2 - c^2}\left(b - c\sqrt{\frac{b^2 - a^2 - d^2}{2c^2 - d^2}}\right) \quad \text{(B.25)}$$

$$m^2_{\tilde{l}_R} = \frac{c^2}{2c^2 - d^2}m^2_{\tilde{\chi}^0_1} \quad \text{(B.26)}$$

$$m^2_{\tilde{\chi}^0_2} = \frac{c^2}{2c^2 - d^2}m^2_{\tilde{\chi}^0_1} + \frac{a^2c^2}{d^2 - c^2} \quad \text{(B.27)}$$

$$m_{\tilde{q}_L} = m_{\tilde{\chi}^0_1} + b \quad \text{(B.28)}$$

Region (4,3):

$$m^2_{\tilde{\chi}^0_1} = m^2_{\tilde{l}_R} + a\left[a(d^2 - c^2) - \sqrt{a^2(d^2 - c^2)^2 + 4c^2d^2m^2_{\tilde{l}_R}}\right]/(2d^2) \quad \text{(B.29)}$$

$$\begin{aligned} m^2_{\tilde{l}_R} = {} & a^2\{-(d^4 - c^4)^2a^8 + (d^2 - c^2)[c^6(2d^2 - 3b^2) + 7c^4b^2d^2 + d^4(c^2(3b^2 - 2d^2) + b^2d^2)]a^6 \\ & + c^2d^2[(5c^4 - 6c^2d^2 - 3d^4)b^4 + (7c^2d^4 + 5c^6 - 5c^4d^2 + d^6)b^2 + 4d^4c^4]a^4 \\ & + d^4c^4[4d^2c^2b^2 - 10c^2b^4 + 2c^2d^4 + 2c^4d^2 + c^4b^2 + 4b^6 - 2d^2b^4 - d^4b^2]a^2 \\ & + c^6d^6(b^2 - d^2)(b^2 - c^2) \pm 2abc\sqrt{(b^2 - a^2 - d^2)(b^2d^2 - 2a^2d^2 - 2c^2d^2 + 2a^2c^2)} \\ & \times[(d^2 + c^2)(d^2 - c^2)^2a^4 + 2c^2d^2(c^2b^2 - b^2d^2 + c^4 + d^4)a^2 + c^4d^4(d^2 + c^2 - 2b^2)]\} \\ & /[a^4d^4 + (a^2 + d^2)^2c^4 + 2a^2c^2d^2(a^2 + d^2 - 2b^2)]^2 \end{aligned} \quad \text{(B.30)}$$

$$m^2_{\tilde{\chi}^0_2} = m^2_{\tilde{l}_R}(a^2 + m^2_{\tilde{l}_R} - m^2_{\tilde{\chi}^0_1})/(m^2_{\tilde{l}_R} - m^2_{\tilde{\chi}^0_1}) \quad \text{(B.31)}$$

$$m_{\tilde{q}_L} = m_{\tilde{\chi}^0_1} + b \quad \text{(B.32)}$$

Appendix C

Details of endpoint measurements

This appendix provide the full information of each endpoint measurement. Table (5.1) and table (5.2) summarize the results showed in the following section.

n	m_{ll}				
	Fit range (GeV)	Binning (GeV)	Endpoint (GeV)	Error (GeV)	$\frac{\chi^2}{NDF}$
1	95-101	0.5	101.2	0.48	1.78
2	96.5-105	0.5	100.2	0.34	2.1
3	96.9-102	1.0	102.7	0.87	0.73
4	96.1-104	1.5	103.7	0.60	0.32
5	96.1-104	2.0	103.3	0.24	0.10
6	95.0-100	2.5	102.7	0.61	0.59
7	95-103	2.5	102.8	0.92	0.17

Table C.1: Fast m_{ll} measurements

n	m_{qll}				
	Fit range (GeV)	Binning (GeV)	Endpoint (GeV)	Error (GeV)	$\frac{\chi^2}{NDF}$
1	410-505	7	498.0	4.0	1.10
2	410-505	6	503.0	6.4	1.43
3	405-502	6	502.6	6.1	1.34
4	415-502	5	500.2	6.50	0.98
5	415-502	9	498.4	5.8	1.14
6	415-502	10	501.2	4.3	0.82
7	440-500	10	500.4	4.2	0.99

Table C.2: Fast m_{qll} measurements

n	m_{ql}^{high}				
	Fit range (GeV)	Binning (GeV)	Endpoint (GeV)	Error (GeV)	$\frac{\chi^2}{NDF}$
1	260-405	7	429.1	9.2	2.1
2	226-435	9	457.6	9.6	1.6
3	260-420	10	445.7	10.0	2.0
4	236-384	12	413.9	9.60	2.5
5	300-435	13	447.2	9.2	2.1
6	280-405	7	425.9	9.2	2.2
7	245-386	6	408.5	9.0	2.4

Table C.3: Fast m_{ql}^{high} measurements

n	m_{ql}^{low}				
	Fit range (GeV)	Binning (GeV)	Endpoint (GeV)	Error (GeV)	$\frac{\chi^2}{NDF}$
1	150-350	9	316.7	5.1	2.1
2	100-350	9	317.3	4.7	1.9
3	135-350	10	321.0	4.8	1.8
4	125-350	11	322.6	5.1	2.0
5	150-350	11	330.8	4.9	1.9
6	150-350	12	325.1	4.7	2.0
7	150-350	13	325.5	4.7	2.1

Table C.4: Fast m_{ql}^{low} measurements

n	m_{ll}				
	Fit range (GeV)	Binning (GeV)	Endpoint (GeV)	Error (GeV)	$\frac{\chi^2}{NDF}$
1	91-105	1	101.8	0.58	2.3
2	91-105	4	103.9	0.74	0.2
3	90-105	3	105.1	0.78	0.1
4	94-105	2	104.0	0.71	0.8
5	90-115	1	101.9	0.58	1.7
6	93.115	2	104.3	0.78	1.3
7	93-105	1	101.7	0.52	2.5

Table C.5: Full m_{ll} measurements

n	m_{qll}				
	Fit range (GeV)	Binning (GeV)	Endpoint (GeV)	Error (GeV)	$\frac{\chi^2}{NDF}$
1	415-510	13	502.6	4.8	1.1
2	385-510	10	498.4	5.8	1.1
3	375-510	10	498.4	5.7	1.0
4	425-510	17	505.1	5.9	1.3
5	355-555	11	502.2	5.0	1.4
6	430-505	12	500.2	5.2	0.8
7	430-505	13	503.2	5.4	1.3

Table C.6: Full m_{qll} measurements

n	m_{ql}^{high}				
	Fit range (GeV)	Binning (GeV)	Endpoint (GeV)	Error (GeV)	$\frac{\chi^2}{NDF}$
1	330-450	12	422.9	5.7	1.0
2	330-450	10	421.8	5.1	1.4
3	380-430	13	418.2	6.5	0.5
4	315-430	10	421.8	4.9	1.2
5	290-415	15	423.4	6.1	1.5
6	380-425	5	413.0	4.9	1.1
7	380-435	8	425.0	5.2	0.2

Table C.7: Full m_{ql}^{high} measurements

n	m_{ql}^{low}				
	Fit range (GeV)	Binning (GeV)	Endpoint (GeV)	Error (GeV)	$\frac{\chi^2}{NDF}$
1	230-325	12	326.3	6.6	0.9
2	219-330	11	320.0	6.1	1.2
3	230-325	14	324.1	6.2	0.7
4	185-325	10	321.9	5.9	1.6
5	195-330	11	311.9	6.3	1.3
6	225-330	17	322.6	5.5	0.5
7	219-330	15	328.4	5.5	0.5

Table C.8: Full m_{ql}^{low} measurements